Tampere University

Wolfram Grötsch

IMPLEMENTING COMPARTMENTALIZED OXYGEN CONTROL TO A NEURONAL CELL CULTURE CHIP

Master of Science Thesis
Faculty of Medicine and Health Technology
Examiners: Prof. Pasi Kallio
Assoc. Prof. Veikko Sariola
September 2023

ABSTRACT

Wolfram Grötsch: Implementing compartmentalized oxygen control to a neuronal cell culture chip
Master of Science Thesis
Tampere University
Biomedical Sciences and Engineering - Biomedical Micro- and Nanodevices
September 2023

To study the effects of low oxygen concentrations (hypoxia) on epileptic cells in neuronal cell culture, an existing cell culture device with three separate cell compartments connected by microtunnels was modified to incorporate targeted oxygen control capabilities to adjust oxygen levels in a single cell compartment. Subsequent cell culture experiments, not included in this study, will determine whether these hypoxic conditions influence seizure initiation or drug response.

Several concepts were conceived and compared using a weighted evaluation. Two concepts were then simulated and a two-layered polydimethylsiloxane (PDMS)-based chip design was selected for implementation. The lower layer contained the microtunnels and the second layer, bonded on top, a scavenging channel routed around one cell compartment. Inside the cell compartment, an oxygen-blocking structure was submerged to limit the scavenging effect to the bottom. Two molds, one for each PDMS layer, were produced using SU-8 photolithography on a silicon wafer to achieve micrometer-scale structures. One of the two molds was a micro-macro mold which is a combination of SU-8 structures and 3D-printed parts to achieve micrometer and millimeter-scale features within a single mold. These parts were 3D-printed using a stereolithography (SLA) printer and bonded with a two-component epoxy adhesive to assemble the mold. The two cast PDMS layers were punched to add the inlets and outlets, cut to open the top, then aligned, and permanently bonded together using oxygen plasma. Leak tests were performed to verify the seal tightness of the scavenging channel prior to further processing. To verify the chosen concept and the numerical simulations, ratiometric two-dimensional oxygen measurements on three built chips were performed. For this purpose, the chips were permanently fixed to a ratiometric measuring plate and imaged over several hours while different known oxygen concentrations were applied as calibration points, followed by the application of pure nitrogen as an oxygen scavenger.

The numerical simulations were in agreement with the measurements, proving their use as a valuable tool for further design iterations. Oxygen control within the target cell compartment was possible with the implemented design, reaching hypoxic oxygen levels in at least one measurement. The oxygen profile along the bottom of the scavenged cell compartment agreed well with the two-dimensional simulation result with a maximum deviation of 0.4 % O_2 compared to the measurement setup it was adapted to. The time constants obtained varied considerably and no clear conclusion was drawn from the results of the three measured chips except that they were in the same range predicted by the numerical simulations. In the later cell cultures, cellular oxygen consumption and nutrient supply affect the cell responses, both of which were not considered in this work. Due to the small volume of culture media available, cells may reach hypoxic conditions significantly faster. In addition, their nutrient supply is limited, which may cause additional cellular responses or cell death in long-term experiments. However, recommendations for their consideration in future work are given in the conclusions.

Keywords: Hypoxia, oxygen control, compartmentalization, two-layered, PDMS

PREFACE

This thesis was conducted in the Micro- and Nanotechnologies research group at Tampere University from January to September 2023, and was part of a project called ASEMO in the multidisciplinary research consortium Centre of Excellence in Body-on-Chip Research (CoEBoC).

I would like to thank my supervisors, Joose Kreutzer and Hannu Välimäki, as well as my examiners, Pasi Kallio and Veikko Sariola, for their regular guidance, support, input, and feedback during the thesis process. I would also like to thank my colleagues Lassi Sukki, Kaisa Tornberg, Jari Väliaho, Timo Salpavaara, and Juha Heikkilä, who were very helpful and always shared their extensive knowledge in this field.

Another big thank you goes to my parents, whose constant support always kept my back free so that I could fully concentrate on my studies, and to my siblings Margitta and Elmar for their support. I also owe a lot of thanks to my partner Essi, who supported me throughout the whole thesis process and had to listen to my struggles every day.

This thesis was written in Overleaf using the template provided by Tampere University, which is currently maintained by Ville Koljonen.

The writing and formulation of some text passages in this thesis were improved using the AI-based writing tools DeepL Write (deepl.com/write) and/or ChatGPT version 3.5 (chat.openai.com), while Grammarly (grammarly.com) was used throughout the entire thesis.

Tampere, 22nd September 2023

Wolfram Grötsch

CONTENTS

LIST OF FIGURES

LIST OF ABBREVIATIONS AND SYMBOLS

2D	Two-dimensional
3D	Three-dimensional
AEAPS	[3-(2-Aminoethylamino)propyl]trimethoxysilane
AED	Anti epileptic drug
BOC	Body on chip
CAD	Computer-aided design
CCD	Charge-coupled device
ECM	Extracellular matrix
FEM	Finite element method
hESC	Human embryonic stem cell
hiPSC	Human induced pluripotent stem cell
hPSC	Human pluripotent stem cell
IPA	Isopropyl alcohol
IUPAC	International Union of Pure and Applied Chemistry
LBM	Lattice Boltzmann Method
MD	Molecular Dynamics
MEA	Multi-electrode array
OOC	Organ on chip
PC	Polycarbonate
PDE	Partial differential equation
PDMS	Polydimethylsiloxane
PMMA	Poly(methyl methacrylate)
PTFE	Polytetrafluoroethylene
PVP	Polyvinylpyrrolidone
ROI	Region of interest
SATP	Standard ambient temperature and pressure
SLA	Stereolithography

SPH	Smoothed Particle Hydrodynamics
TDS	Transport of Diluted Species
WHO	World Health Organization

Symbols

c	molar concentration, $[\frac{\mathrm{mol}}{\mathrm{m}^3}]$
D	diffusion coefficient, $[\frac{\mathrm{m}^2}{\mathrm{s}}]$
f_1	fraction of dye molecules of the first type, $[-]$
f_2	fraction of dye molecules of the second type, $[-]$
F_v	volume fraction, $[-]$
H	constant to convert k_h to $k_{h(T)}$, $[\mathrm{K}]$
J	diffusion flux, $[\frac{\mathrm{mol}}{\mathrm{s\,m}^2}]$
k	mass transport coefficient, $[\frac{\mathrm{m}}{\mathrm{s}}]$
k_H	Henry's constant, $[\frac{\mathrm{Pa\,m}^3}{\mathrm{mol}}]$
K_p	partition coefficient ratio, $[-]$
K_{SV}	specific quenching efficiency, $[\frac{1}{\mathrm{Pa}}]$
n	amount of substance (Equation 2.7), $[\mathrm{mol}]$
n	pressure dependence of solubility (Equation 2.14), $[\frac{1}{\mathrm{atm}}]$
p	pressure, $[\mathrm{Pa}]$
p_{O_2}	partial pressure of oxygen, $[\mathrm{Pa}]$
R	universal gas constant (Equation 2.7), $[\frac{\mathrm{J}}{\mathrm{K\,mol}}]$
R	intensity ratio of red and green channel at a specific partial pressure of oxygen (Equation 2.2), $[-]$
R_0	intensity ratio of red and green channel at zero oxygen concentration, $[-]$
S	solubility, $[\frac{\mathrm{cm}^3(\mathrm{STP})}{\mathrm{cm}^3\,\mathrm{atm}}]$
S_{inf}	infinite solubility of a gas in polymer, $[\frac{\mathrm{cm}^3(\mathrm{STP})}{\mathrm{cm}^3\,\mathrm{atm}}]$
T	temperature, $[\mathrm{K}]$
u	velocity field, $[\frac{\mathrm{m}}{\mathrm{s}}]$
V	volume, $[\mathrm{m}^3]$

Subscripts

ch	chamber (pressure)
$\_\mathrm{eq}$	equilibrated (concentration)
g	gas phase
gl	gas-liquid interface
gp	gas-PDMS interface
$H(\mathrm{SATP})$	Henry's law constant at standard ambient temperature and pressure
$H(T)$	Henry's law constant at experiment temperature T
inf	at infinity (solubility)
l	liquid phase
lg	liquid-gas interface
lp	liquid-PDMS interface
$\mathrm{O_2}$	oxygen
p	PDMS phase (solid)
pg	PDMS-gas interface
pl	PDMS-liquid interface
SATP	standard ambient temperature and pressure ($298.15\ K$ and $1\ atm$)

1. INTRODUCTION

Epilepsy is one of the most common disabling neurological disorders. It affects the lives of approximately 65 million people worldwide and is ranked by the World Health Organization as the second most serious neurological disorder. [1] Several drugs are available on the market to treat the disease but are ineffective in one-third of the patients. In the search for new effective drugs, researchers use animal models or, increasingly, organ-on-chip platforms based on human-derived cells. [2], [3] By using human-derived cells in these models, animal testing can be reduced and preliminary drug testing can provide more relevant results that are applicable to humans, as animal testing is often unable to properly model a disease and provide adequate insight into the viability of a drug [4].

Researchers at the Tampere University have developed such an organ-on-chip platform using human-derived cells to study epilepsy. In short, this platform has three fluidically separated cell compartments connected by microtunnels through which axons can grow and the cells form a network that spans all cell compartments. In Figure 1.1 the cell culture device is shown mounted onto a multi-electrode array (MEA) plate for the measurement of neuronal activity. The separate cell compartments allow localized stimulation of the cells with different drugs to induce or reduce seizure activity of the network, as demonstrated by Pelkonen et al. [5]

Hypoxia, a condition in which cellular oxygen levels are too low compared to what is re-

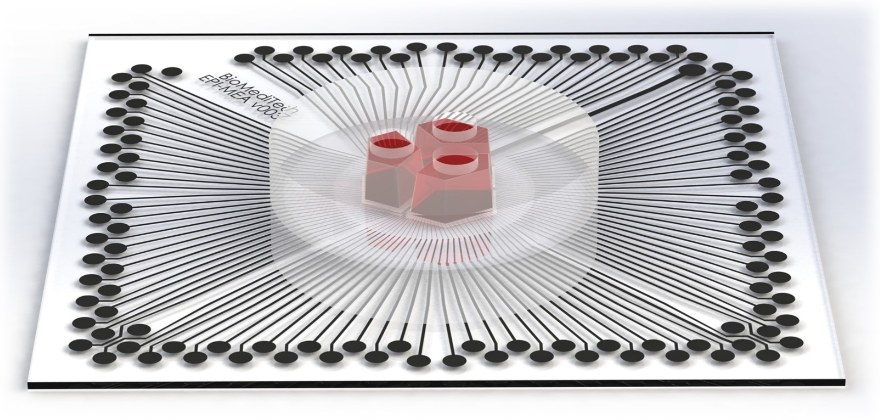

Figure 1.1. *Cell culture device with its three cell compartments shown in red mounted on a multi-electrode array plate. Image created by Lassi Sukki of Tampere University.*

quired in a physiological environment, has been shown by Xu and Fan to increase seizure susceptibility [6]. A commonly used method to control oxygen levels in cell cultures and reach hypoxic conditions is to build chips out of oxygen-permeable materials and place them in an atmosphere with the desired oxygen levels, which affects the entire chip [7]. However, to achieve localized control of oxygen levels, control channels can be used. They may be supplied with liquids or gases at a specific target level of oxygen [8], [9]. Alternatively, liquid oxygen scavengers that actively bind the oxygen by a chemical reaction are commonly utilized [10].

In order to further study the effects of hypoxia on epileptic seizures and the viability of drugs, researchers from Tampere University want to extend the cell culture platform described above with localized oxygen control capabilities to create hypoxic conditions in one cell compartment while keeping the others at higher oxygen levels. The design, implementation, and verification of such a solution is the scope and aim of this Master's thesis. The specific research questions are:

1. Can oxygen levels in the hypoxic range for neuronal cells be achieved?
2. What is the oxygen profile the cells will experience?
3. How would such a system look like and what kind of fabrication steps will be required?

Next, the thesis content is outlined. This thesis starts by introducing several theoretical concepts and state-of-the-art. First, epilepsy and hypoxia are explained, followed by the main oxygen transport mechanisms relevant to physiological and *in vitro* systems. Then, a quick introduction to *in vitro* cell cultures and available oxygen control techniques for them is given. This is followed by an overview of the use of polydimethylsiloxane (PDMS) for microfluidic devices as well as various approaches to produce layers of PDMS with through-holes. Afterward, a quick overview of available electrochemical and optical oxygen sensing procedures is given. Subsequently, the previously introduced neuronal cell culture device and research results generated with it are highlighted. The last part of this chapter examines numerical simulation methods and models for the simulation of oxygen transport and the required equations.

At the beginning of Chapter 3, the design and design selection methodology along with the boundary conditions for the designs are demonstrated. This is followed by the simulation approach which was used for the comparison and evaluation of the approaches. Then, various tested techniques for the manufacturing of PDMS membranes with openings are presented. Afterward, the mold manufacturing procedures are explained, starting from the design and fabrication of the required photolithography masks, the photolithography procedure itself, the mold characterization, and its finalization. Subsequently, the fabrication steps of the chips from fabricating the individual layers over their alignment and bonding to the finalization are given. The chapter concludes with a description of the oxygen measurements that were conducted to verify the design and simulations.

The obtained results are displayed and discussed in the fourth chapter. Initially, the conceived designs are introduced, evaluated, and compared. The comparison based on the simulation results follows and the final implemented design is described. Then, the results of the membrane manufacturing tests are presented followed by the results of the mold and chip fabrication. The chapter concludes with the oxygen control measurement results and a comparison to the results of a simulation using room temperature parameters.

A summary of the results and final conclusions, as well as considerations for future work, are the content of the fifth chapter.

2. THEORETICAL BACKGROUND

2.1 Epilepsy and hypoxia

One of the most common neurological disorders with disabling effects is epilepsy. Around 65 million individuals globally are impacted by it, and the World Health Organization (WHO) ranks it as the second worst neurologic disorder worldwide [1]. For treatment, over 20 anti-epileptic drugs (AEDs) have been approved so far, but for around one-third of the patients, they do not help control their seizures. For this group, alternative treatments are implanted neurostimulators, dietary therapies, or surgery. [2] The available surgeries have the highest success rate in treating epileptic seizures. However, they are often seen as a last resort as they pose great health risks and are very costly. Only patients with frequent and intense seizures, despite treatment with AEDs, are eligible for it. [11]

Animal models, primarily based on rodents, are commonly used for studying the pathophysiology of epilepsy and in the research of new AEDs [2]. However, newly found compounds that work in animal models do not always translate to humans and might fail during pre-clinical testing, wasting a significant amount of money and time [12]. To speed up the development of novel and efficient drugs, new methods for the study of epilepsy and the research of AEDs are developed in the form of organ-on-chip (OOC) cultures [3]. They utilize neuronal cells, which are often derived from human induced pluripotent stem cells (hiPSCs), and therefore generate more relevant results for the treatment of humans [3], [5]. In many patients, the exact cause of an epileptic seizure is not known. However, seizures can be caused by almost any injury that affects brain function. This can be due to acquired injuries such as a traumatic brain injury, stroke, genetic mutations, or autoimmune or infectious diseases [2]. Chronic hypoxia, a state of too-low oxygen levels in tissues, was found to increase the seizure risks during *in vitro* experiments [6].

Hypoxia, or low oxygen pressure, is a state in which the oxygen levels of a tissue fall below their normal (physioxic) levels. It affects several aspects of cell behavior, such as cellular metabolism, apoptosis, DNA repair, and proliferation [13]. However, hypoxia not only triggers negative responses but it was also found to aid in the proliferation of neuronal stem cells [14].

Besides hypoxia, four more terms are used to describe the oxygen contents in tissues. These are, ranging from lower to higher concentration, anoxia, hypoxia, physoxia, normoxia, and hyperoxia. An overview with general values is shown in Table 2.1.

The oxygen concentrations in various human body tissues differ significantly in the range of 0-12 %. An overview of selected tissue concentrations is shown in Table 2.2. However, the oxygen concentration is not always the same within an organ. The liver, for example, does not have only one oxygen concentration but relies on a gradient [15]. This gradient is crucial for the liver's metabolic zonation, enabling it to run metabolic pathways in parallel at maximum efficiency [16].

Table 2.1. *Glossary of terms describing the various oxygen concentrations for tissues. Adapted from ref. [17]*

Term	**Description**
Anoxia	Oxygen levels < 0.02 %, often leading to necrosis.
Hypoxia	Low oxygen levels causing adaptive responses at cell or tissue level. Occurs at 3-5 % oxygen, depending on the tissue.
Physoxia	The normal level of oxygen as found in the body. It depends on the tissue but overall between 4-12 %.
Normoxia	The oxygen level found in the atmosphere (∼21 %). It often causes hyperoxic conditions in *in vitro* cultures.
Hyperoxia	Levels of oxygen above the physioxic levels.

Table 2.2. *An overview of physioxic tissue oxygen levels in humans. [17], [18]*

Tissue	**Physioxic oxygen levels**
Tumors	0-2 %
Muscle	3.8 %
Brain	4-6 %
Liver	4-13 %
Ovaries	12 %

2.2 Oxygen transport mechanisms

In order to understand the options available to control oxygen concentrations in cell culture systems, we need to know the foundational mechanisms at play for the transport of oxygen in organisms and cell cultures. The two most important ones are convection and diffusion.

Convection is the active movement of fluid and comes in two different forms. Natural convection is generally caused by heat and causes fluids to rise due to heat-induced density changes and sink back down once it cools, causing a steady movement of the fluid and a current within that transports substances. [19] On the contrary, forced convection occurs when an external source, such as a pump, forces a fluid to move. In the case of an organism, this forced movement would be caused by the heart [20], while in cell cultures, it is often emulated using peristaltic or syringe pumps [21]. Mixed convection occurs when natural and forced convection is present in a system at the same time. [22]

The second form of oxygen transport is a passive mechanism called diffusion, which plays an important role in the transport of oxygen in organisms [20]. Fick's first law of diffusion describes that the diffusion flux always depends on a concentration gradient. A substance will always move along this gradient from a higher to a lower concentration in an attempt to reach equilibrium. This is indicated in Equation 2.1 by the minus sign in front of the diffusion coefficient D [23]. In humans, this gradient is present, for example, in the lungs' alveolus, where the aspirated air's oxygen diffuses into the oxygen-depleted blood. [24] For a one-dimensional system, Fick's first law of diffusion can be written as:

$$J = -D\frac{\partial c}{\partial x}\,, \tag{2.1}$$

where J denotes the flux or rate of diffusion of the substance, D is the diffusion coefficient, which depends on the properties of the substance and the medium through which it is diffusing, c is the concentration, and x is the considered length.

Diffusion is most efficient at short distances, as the required time increases significantly with the diffusion distance due to a lowered concentration gradient and the random movement of molecules [23], whereas forced convection is more efficient in transporting oxygen over greater distances.

Diffusion processes are significantly temperature dependent. In pure water, for example, the oxygen diffusion coefficient is $D = 2.0 \cdot 10^{-5}\mathrm{cm^2/s}$ at 21 °C and increases significantly to around $D = 2.8 \cdot 10^{-5}\mathrm{cm^2/s}$ at 37 °C, which is the temperature at which cell culture experiments are conducted [25]. The composition of the substance through which the oxygen diffuses also affects its speed. In cell culture media, for example, the added proteins negatively impact oxygen diffusion ($D = 2.69 \cdot 10^{-5}\mathrm{cm^2/s}$ at 37 °C) compared to isotonic saline ($D = 2.84 \cdot 10^{-5}\mathrm{cm^2/s}$ at 37 °C). [26] The phase through which oxygen needs to diffuse also impacts its diffusion speed. It diffuses around 10,000 times faster in the air than in water [27]. However, its diffusion speed in polydimethylsiloxane (PDMS) is roughly the same as in water with a value of ($D_{\mathrm{PDMS}} = 3.4 \cdot 10^{-5}\mathrm{cm^2/s}$ at 35 °C) [28].

Due to the limited effective diffusion distance *in vivo*, which often does not exceed 100 µm from capillaries to cells, the blood flow needs to be improved for oxygen-hungry tissues, such as muscle. Therefore, another form of active oxygen transport is utilized. A protein called myoglobin aids in the transport of oxygen. [29] However, in cell cultures, this additional mechanism is not present as the conditions for the myoglobin to function properly are not met [26].

2.3 *In vitro* cell cultures

In vitro cell cultures play a large role in today's research of diseases and the search for new medications and treatments. They offer the possibility of studying cells in a controlled environment without any systemic effects. [30] In an ethical context, their image is significantly better than animal experiments, which experience more and more disapproval in today's society and suffer from a poor translatability of results from animals to humans [31], [32]. These cultures can be established using animal [30], or human [33] derived cells. However, in many cases, the medical value of *in vitro* cell cultures utilizing human-derived cells yields more relevant results [33]. Therefore, human pluripotent stem cells (hPSCs) are used. Their pluripotency allows them to differentiate into almost every cell type found in the body. The first type, human embryonic stem cells (hESCs), are derived from human embryos and are ethically controversial. Human induced pluripotent stem cells (hiPSCs), on the other hand, are produced by reprogramming cells harvested from adults. [34] They offer the additional benefit that cells from a patient with a specific genetic disease can be harvested and used for intensive cell studies allowing the study of disease patterns and potential drug candidates [35]. The sole use of *in vitro* cell tests as a replacement for animal tests of medications is not yet officially approved by the FDA, and pharma companies trust their over the years established processes and protocols and are reluctant to make a change [36].

All *in vitro* cell cultures have in common that they require some form of control over the environment. The most important parameters are the CO_2 and O_2 levels, pH, osmolality, temperature, and enough nutrients, which are supplied through special culture media. [30] There are a variety of cell culture formats available, which can be broadly categorized into two-dimensional (2D) and three-dimensional (3D) cultures, both with their own advantages and drawbacks.

2.3.1 Two-dimensional cell cultures

Two-dimensional cell cultures are the oldest and simplest form of cell culture [37]. They are mostly monolayer cell cultures that consist of a single layer of cells on a substrate and are either grown in Petri dishes (Figure 2.1a) or for automated and large-scale experiments in well plates (Figure 2.1b), which feature an array of separated wells of equal volume.

2D cell cultures offer several advantages for laboratory experiments. They allow for finely controllable culture conditions, making them highly reproducible and well-suited for com-

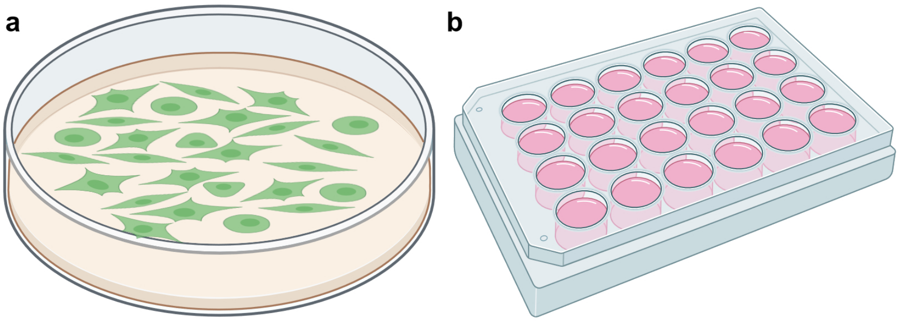

Figure 2.1. *Schematic representations of 2D cell cultures.* ***a:*** *Petri dish with cells,* ***b:*** *24-well plate filled with culture media. Created with BioRender.com*

parative experiments. Additionally, 2D cultures are economically advantageous due to their ease of use and fast setup time, saving both time and money. However, 2D cell cultures have several drawbacks. The morphology of cells cultivated in 2D cultures differs from that of cells *in vivo*, which can lead to changes in cell function, internal structures, cell signaling, and secretion. Additionally, in 2D cultures, all cells receive the same supply of substances from the culture medium, which is not reflective of the complex three-dimensional structures found *in vivo*, where cells near vessels receive more nutrients and oxygen compared to more distant cells. [37] In order to overcome these weaknesses, 3D cell cultures were developed.

2.3.2 Three-dimensional cell cultures

Three-dimensional cell cultures are more sophisticated and model important physiological processes and responses better than their 2D counterparts [37]. The idea has been around for many decades, but recent milestones in the development of cell culture substrates, culture media, and techniques have caused a surge in the use of 3D cultures [38].

One way to culture cells in a three-dimensional environment is by using hydrogels (Figure 2.2a) or scaffolds. Both offer a supportive structure that helps preserve cell morphology. Hydrogel-based 3D cultures utilize a highly water-absorbent hydrogel to mimic the extracellular matrix (ECM) to give the cells a supportive environment to grow in. The cells can be either encapsulated within the gel or seeded to its surface, where they will migrate into the structure. Scaffold cultures, on the other hand, use a solid material like ceramics or metal as support, where the cells get seeded on top and migrate into the scaffold. [39]

Spheroids (Figure 2.2b) are three-dimensional cell clusters made up of hundreds to thousands of cells. They are formed either by self-assembly or through forced clustering. They provide an environment that simulates *in vivo* conditions more closely compared to monolayer cultures by enhancing cell-to-cell and cell-to-ECM interactions which improve differentiation, drug response, and metabolism. However, with increasing size, they suffer

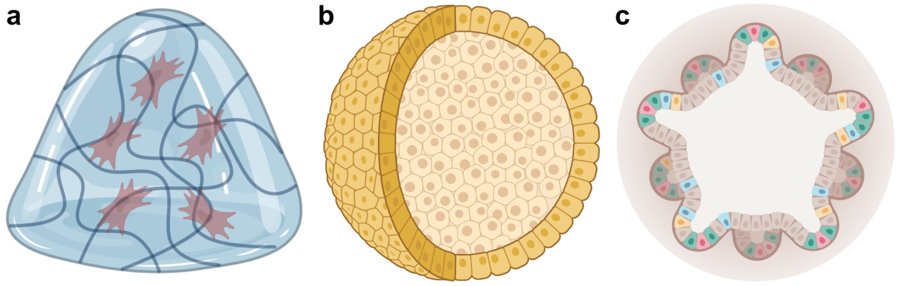

Figure 2.2. *Schematic representations of 3D cell cultures.* ***a:*** *Hydrogel,* ***b:*** *Spheroid,* ***c:*** *Organoid. Created with BioRender.com*

from hypoxia and cell necrosis at their core due to larger diffusion distances for oxygen and nutrients. [40], [41]

Organoids (Figure 2.2c) are complex 3D structures that mimic the *in vivo* architecture and function of the targeted organ and its tissue more accurately than spheroids. They are typically derived from human pluripotent stem cells and are formed via self-assembly by providing minimal differentiation information, sufficient nutrients, and time. However, like spheroids, organoids lack vascularization, which can lead to hypoxia and cell necrosis at their core. They hold great potential for biomedical research and drug development, as they can be used for personalized medicine, drug screening, and disease modeling. In the future, organoids may even enable lab-grown organ transplants, but significant improvements and further research are still needed to achieve this goal [39]. [42], [43]

In general, 3D cell cultures provide a more accurate representation of the complex *in vivo* environment. This is because the cells are able to maintain their morphology, mode of division, and phenotype. However, 3D cell cultures are significantly more complex, expensive, and time-consuming compared to 2D cell cultures. Moreover, the reproducibility of results between experiments and labs may differ, posing a challenge for researchers.

Another form of cell culture that cannot be clearly categorized into 2D or 3D cultures is the suspension cell culture. Here, the cells float freely without attachment to a substrate within the culture media in a bioreactor. To maintain equal nutrient distribution, these reactors are stirred. This form of culture is suitable for the large-scale production of vaccines or proteins. [44] However, suspension cultures are not only used for single cells but are also utilized with organoids [43] and spheroids [40] for large-scale experiments.

2.3.3 Organ on chip

Organ-on-chip (OOC) cell cultures are a type of culture that largely incorporates microfluidics technology. In an OOC system, living cells of one or more types are cultured with structural complexity and often integrate a dynamic fluid flow of culture media, allowing for the recreation of the *in vivo* microenvironment. The OOCs can be created using a variety of previously introduced 2D and 3D cell cultures, like organoids, spheroids, hydrogels, and monolayers, with over 21 different tissues and organs already modeled in this way. [33] Two different OOC platforms are shown in Figure 2.3. Mechanical stimuli can be applied to the cells in OOCs by utilizing laminar, pulsatile, or interstitial fluid flow, an increase in pressure, or stretching and straining their substrate [21].

Moreover, researchers have combined multiple OOCs to create a so-called body-on-chip (BOC) system. These are particularly useful for drug testing in complex systems, where the responses of multiple organs and tissues within the body can affect the outcome of the study. When using human-derived cells, they might one day replace animal models and play a key role in the development of personalized medicine.

Another type of culture commonly categorized as OOC is co-cultures. They are used to study cell-to-cell interactions and consist of two or more cell types within the same cell compartment or in separate cell compartments but with some form of contact between them. They are important for drug development as such a system models the complex *in vivo* environment more closely [45]. Furthermore, some cells, when cultured alone, do not behave in the same way as they do *in vivo*. However, when they are cultured with other cells in a co-culture, their behavior can resemble their *in vivo* behavior more closely. [46]

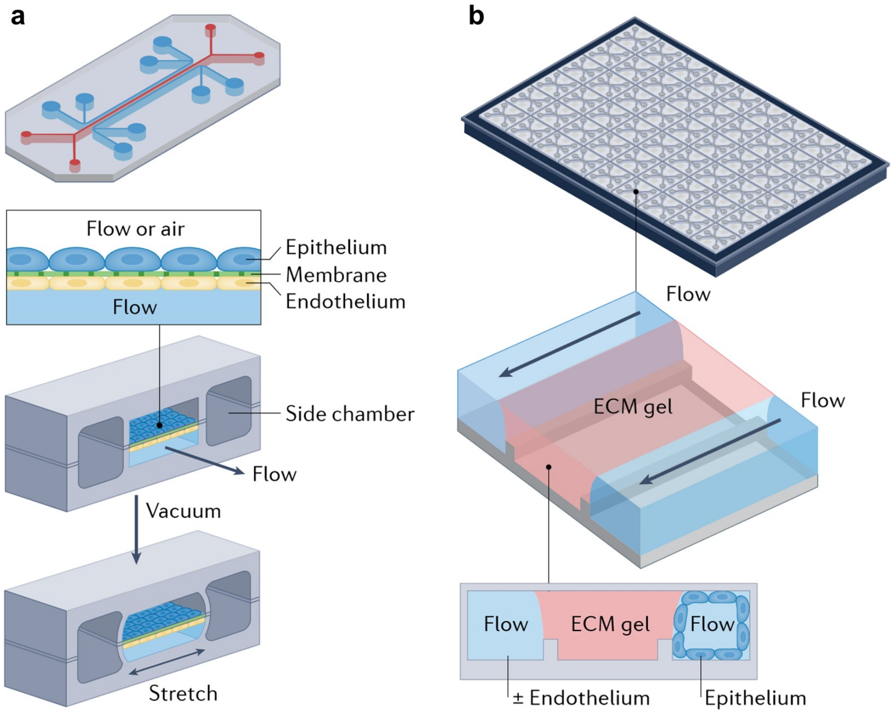

Figure 2.3. *Schematic representations of two forms of organ-on-chip systems.* ***a:*** *PDMS-based chip that allows for two-sided fluid flow and mechanical stretching (e.g., to simulate breathing) of the cells. The membrane is perforated, allowing for tissue-tissue interactions.* ***b:*** *A high throughput array of three-channel chips made from polystyrene. The cells may be cultured either in the gel or in the surrounding channels. Adapted from ref. [33].*

A co-culture involving human-derived neuronal cells and cardiomyocytes was conducted by Häkli et al. in which the cells were seeded in separate cell compartments which are connected by small microtunnels that keep the cells separated, but allow for the neurons' axons to grow through and form connections with the cardiomyocytes. The neurons were stimulated while the beating heart cells were monitored, and changes in the contraction were observed. [47]

Many of the here-introduced cell culture variations can exist in combined forms. Spheroids [41] and organoids [43], for example, can be cultured in suspension culture. While spheroids [41] and monolayers [48] can be used in co-cultures.

2.4 Oxygen control in cell cultures

Maintaining appropriate oxygen levels in cell cultures is essential for accurately modeling *in vivo* processes. The oxygen levels in tissues play a critical role in proper tissue functioning. Hypoxic conditions, or low oxygen levels, activate hypoxia-related pathways such as proliferation, migration, apoptosis, differentiation, and metabolism. Conversely, normoxic or hyperoxic conditions, or high oxygen levels, can lead to reduced plating efficiency, lower metabolic activity, and decreased proliferation [49]. However, neither deviation accurately models healthy *in vivo* conditions.[7]

Hypoxic conditions can be induced in cell cultures to model ischemia, a condition in which blood flow and oxygen supply to tissues are limited. Ischemia can occur during strokes [50] and heart attacks [51]. Therefore, controlling oxygen levels in cell cultures is crucial to simulate these conditions or to reach physiological oxygen levels. The motivation for developing oxygen control in cell cultures is to accurately model *in vivo* conditions and better understand the effects of oxygen levels on tissue functioning. [7]

2.4.1 Global oxygen control

Passive control of oxygen levels in cell cultures can be achieved by designing them with oxygen-permeable or impermeable materials. PDMS is a common choice of material for cell culture chips [33], given its inherent permeability to oxygen [52], which ensures adequate oxygen supply to cells in the device. To limit oxygen diffusion through the chip, non-permeable materials like poly(methyl methacrylate) (PMMA) or polycarbonate (PC) can be embedded into the PDMS [17]. Alternatively, the entire chip can be made from an oxygen-impermeable material such as glass [53] or polystyrene [54], [55].

The simplest form of oxygen control is to keep the cell culture in an incubator, hypoxia workstation [7], or an enclosed gas-tight chamber [5] where a specific gas composition is maintained. A hypoxic workstation is displayed in Figure 2.4.

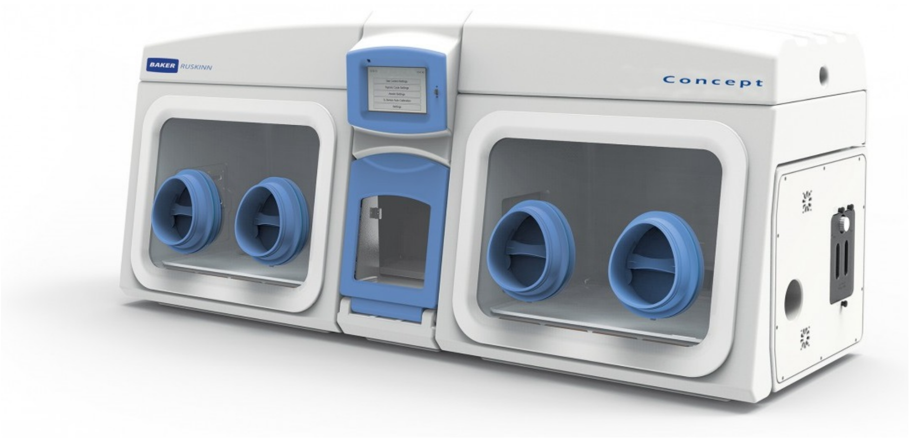

Figure 2.4. *A dual hypoxic tabletop workstation by Baker. [56]*

They work especially well with 2D cell cultures in well plates or Petri dishes. When microfluidic chips are used, the diffusive properties of the used materials are essential to get the desired oxygen flux. These systems allow for the control of the oxygen concentration at the macro scale but offer little to no control of the oxygen concentration at the micro scale at the cell level. Furthermore, it is impossible to implement controlled oxygen gradients that are required for more complex tissue models. [17]

2.4.2 Local oxygen control

To achieve more precise control over oxygen levels, researchers use an active perfusion system. This involves perfusing liquids or gases with a specific oxygen concentration or active scavenger liquids through channels in close proximity to the cell culture area. These channels can be positioned above [8], below [9], or at the side [10] of the target area, always separated by a membrane. To reduce oxygen concentration, 100 % nitrogen gas can flow through the channels, creating a gradient that causes oxygen to diffuse from the cell compartment into the channel. Liquid oxygen scavengers, such as sodium sulfite (Na_2So_3), chemically bind oxygen [10]. In both cases, a constant flow makes sure the gradient or reaction is maintained. These scavenger-based systems enable dynamic alteration of oxygen concentration during an experiment, with the possibility of rapid changes in less than a minute as demonstrated by Tornberg et al. [9]. They used a chip with three separate cell compartments, connected via microtunnels, in which they were able to set distinct oxygen concentrations via an additional structure containing the microfluidic channels shown in Figure 2.5.

An alternative method to control oxygen involves directly adjusting the oxygen levels in the medium by using an aerator to add oxygen to the culture. This method is used when the entire cell compartment is perfused with culture media [26]. In addition, the inherent oxygen-scavenging property of a material can be utilized to control oxygen levels in microchannels. Kiiski et al. [57] demonstrated this approach using off-stoichiometric thiol-

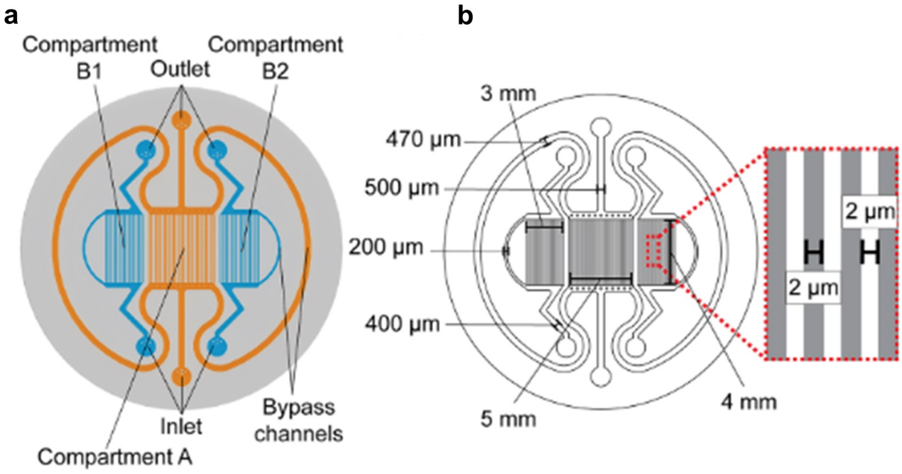

Figure 2.5. *Microfluidic channel structure for oxygen control with three cell compartments.* ***a:*** *Highlighted separate cell compartments.* ***b:*** *Channel dimensions. Modified from [9].*

enes (OSTE). They propose that oxygen scavenging occurs at the interface between the polymer and liquid, where excess thiol monomers undergo an oxidative reaction.

2.5 Microfluidic devices from PDMS

Using PDMS, more specifically Sylgard 184 from Dow Corning, in the manufacture of microfluidic systems using a rapid manufacturing procedure was first introduced by a research group led by George M. Whitesides at Harvard University in 1998. The researchers demonstrated that PDMS could be used to create microchannels and microstructures in a cost-effective and efficient manner, which allowed for the rapid manufacturing of microfluidic devices.

In their described procedure, a fluidic geometry is drawn using CAD software and transferred to a photomask, with the desired features being transparent. A negative photoresist (SU-8) is spin-coated onto a silicon wafer, and the pattern is transferred from the mask to the SU-8 using UV light. Then, the non-illuminated SU-8 is removed using a chemical developer, which results in the transparent areas as protruding features to form the positive mold. PDMS in a mixture of 10:1 is then cast to the mold and cured at 65 °C for 1 h. Subsequently, the PDMS is demolded, cleaned, and treated with oxygen plasma together with a sheet of PDMS. After the plasma treatment, both pieces were permanently bonded together by bringing them in contact. [58]

The plasma treatment that is used for permanently bonding PDMS to PDMS or glass also changes its hydrophilicity. Contact angles of water on PDMS of less than 5° can be achieved, while the contact angle of untreated PDMS is around 107° [59]. However, increased hydrophilicity due to oxygen plasma treatment lasts only for a short time, and hydrophobic recovery sets in within minutes. [60] Longer-lasting hydrophilic surface treatment is achieved by applying PVP right after oxygen plasma treatment, which results in contact angles of less than 30° for time periods of over six months [61].

The great success of PDMS as a material used in cell culture applications is attributed to some of its unique properties, such as flexibility, inertness, stability, and non-fluorescence [62]. Other beneficial properties are its optical transparency down to 280 nm [63], gas permeability [64], and biocompatibility [65]. Many of these properties have been thoroughly studied. Properties such as diffusion coefficient, solubility, and permeability for various substances at different temperatures [52], [66], as well as mechanical parameters like tensile strength and hardness for different mixing ratios [67], can be readily found in publications. Additionally, the softness and elasticity of PDMS enable it to be easily molded into complex shapes and structures that can mimic the *in vivo* microenvironment of cells [68].

However, PDMS also has some disadvantageous properties, such as the leaching of uncrosslinked oligomers, absorption of small molecules, and swelling. Absorption of small molecules is an issue for drug response studies, as it alters the concentration and affects bioavailability. In a study conducted by Meer et al., [69] the absorption was found to be variable and time-dependent. To reduce the absorption of drug molecules, they propose two lipid-based coatings. Carter et al. showed that the uncrosslinked oligomers which leach from the bulk PDMS could affect cell behavior and that longer curing times can significantly reduce the released amount [70]. PDMS is also prone to swelling when exposed to non-polar solvents such as toluene and hydrocarbons. This effect can be permanent when exposed for longer durations but can be reversed when exposing the PDMS to various solvents of decreasing solubility [71].

2.6 Techniques for the production of PDMS layers with through-holes

In order to produce multi-layered microfluidic devices from PDMS by bonding two or more layers on top of each other, the lower layers require openings for the fluidic paths. Another requirement is a smooth and even surface on both sides of the lower layers to ensure a tight bond, which is crucial to minimize the risk of leakage. There are several methods described for the manufacturing of openings in PDMS sheets. The manual manufacturing of openings using a scalpel or punches is a simple and fast procedure. However, it is not an option for microfluidic devices requiring small features because it suffers from low accuracy and repeatability.

An approach using laser ablation is described by Huft et al. [72]. It utilizes machine vision to detect molded features in PDMS chips by scanning them on an XY-translation stage. A 25 W CO_2 laser with a wavelength of 10.6 µm is used for the ablation to add features such as vias or microchannels with a positional accuracy of 20 µm. At optimal settings, the system achieved eight vias per second, largely limited by the speed of the XY-stage. [72]

Santisteban et al. [73], propose an approach that utilizes spin-coating the PDMS onto a mold. Hereby the resulting layer is aimed to be thinner than the mold features are tall, so the protruding features result in openings. They coat the entire mold surface with a 250 nm thick octafluorocyclobutane (C_4F_8) layer to achieve better layer uniformity. This modifies the surface's contact angle with water to be 125 ± 3°. The now hydrophobic surface repels the PDMS, forming a more even layer at the PDMS-Air interface next to the pillars. In order to be able to spin-coat PDMS layers with a thickness in the range of 25 to 125 µm, they utilized off-ratio mixtures of PDMS (i.e., 5:1, 20:1) or thinned the PDMS mixture using silicon oil.

Qu et al. [74] describe a process that allows for manufacturing through-holes in PDMS sheets. It uses a mold with protruding micropillars fabricated from SU-8 on a substrate. On top of the pillars, another substrate with double-sided tape is placed, with the tape facing the pillars. The stack is placed in a PDMS-filled container in a vacuum chamber. Upon applying the vacuum, the air between will escape and be replaced by the PDMS.

A similar approach described by Chiu et al. [75], uses SU-8 molds as well. However, the mold is covered with PDMS before a polytetrafluoroethylene (PTFE) sheet is applied on top of the protruding features. A pressure of up to 50 kPa was applied to the sheet during the curing to squeeze out all the PDMS between it and the SU-8 structures to ensure the vias stay open and are not closed by a thin layer of PDMS. After curing, the PTFE sheet was peeled off, and the PDMS membrane remained in the mold due to higher adhesion to the mold substrate than the PTFE sheet. With thin, flexible membranes, this simplifies handling during further processing steps. Figure 2.6 shows a schematic of this procedure applied to manufacturing a two-layered microfluidic device with fluidic connections through the openings. [75]

For Carlborg et al. [76], this did not work reliably enough as they describe problems with the residual layers blocking the holes. Their described approach is based on the spatial inhibition of the platinum catalyst in PDMS, which is responsible for the crosslinking reactions. The platinum catalyst binds to amines, which they have deposited in the form of aminoethylaminopropyltrimethoxysilane (AEAPS) on top of a glass plate. This is done by submerging them for 1 h in a solution of 2 % w/w of AEAPS in methanol. Subsequently, the glass plates are baked for 10 min at 110 ℃ so the silane links covalently to the glass plates. Similar to the method described by Chiu et al. [75], the glass plate is then clamped onto the protruding SU-8 features of a mold. The crosslinking reaction is only suppressed at the interface of coated glass plate and PDMS above the protruding structures, where the catalyst trap is close, and the diffusion distance from the bulk is large, see Figure 2.7.

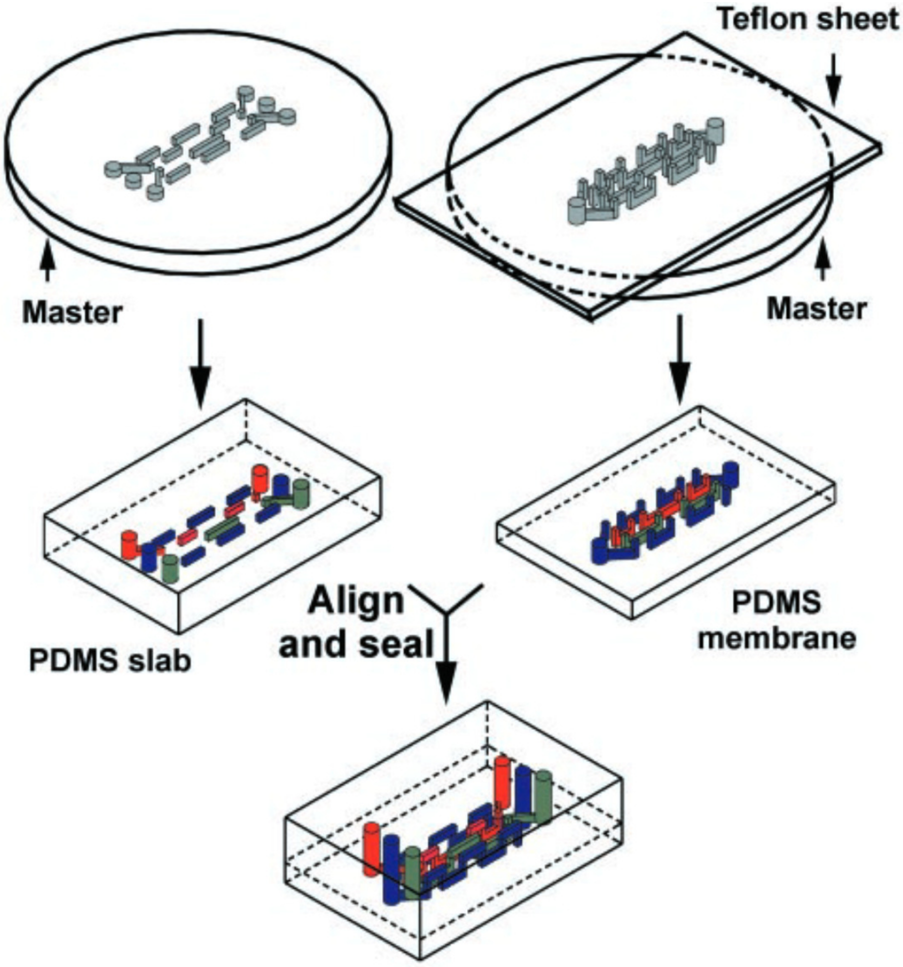

Figure 2.6. *Schematic of the fabrication process for a two-layered microfluidic device. The right side visualizes the process of producing a PDMS membrane with openings using a PTFE (Teflon) sheet. [75].*

However, next to them, the catalyst can diffuse freely from the bulk upwards and at least partially crosslink the PDMS. After removing the PDMS from the glass plate, the surface is sticky, similar to tape, which can be attributed to a lower level of cross-linking. [76]

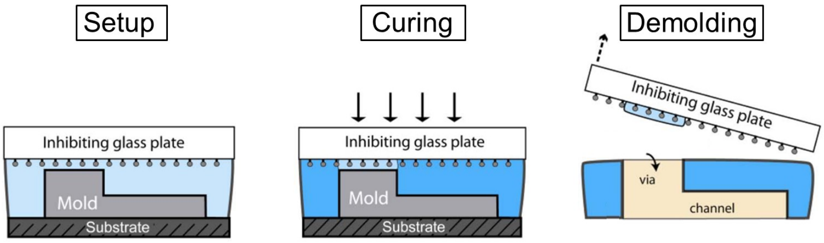

Figure 2.7. *Schematic showing the molding procedure using coated glass plates to inhibit PDMS cross-linking at the glass-PDMS interface. Adapted from ref. [76].*

2.7 Oxygen sensing techniques

The ability to accurately measure and evaluate achievable oxygen levels and gradients using a designed hypoxia system is crucial during the development and for the final validation of the system to produce reliable and repeatable conditions. According to Palacio-Castañeda et al. [17], the most commonly used measurement approaches are based on electrochemical and optical detection.

2.7.1 Electrochemical sensors

All electrochemical measurement techniques rely on the same principle. They measure a current generated by a reduction reaction which is proportional to the concentration of dissolved oxygen. These sensors are ultra-microelectrodes [77] or small-scale Clark electrodes [78], and largely appear in arrays to gather data over larger surface areas [79], [80]. These sensors are easy to miniaturize and integrate into a microfluidic device and offer high sensitivity. Using sensor arrays, gradients can be measured at different locations. However, the active consumption of oxygen is a major drawback of these electrode-based sensors. This is particularly problematic when working with small liquid volumes. Other limitations are the lack of spatial data, the degradation of the electrode due to the adsorption of proteins, and the potential for cell toxicity due to the materials used in the electrodes. For more responsive measurements, it is also beneficial if the solution is stirred or in motion to avoid local depletion of oxygen near the electrode due to the reduction reaction. [7], [17]

2.7.2 Optical sensors

Optical oxygen measurements are based on oxygen-sensitive materials' luminescence intensity and lifetime. When oxygen is present, this luminescence is quenched, which causes the measured intensity and lifetime to increase with decreasing oxygen levels [81]. These oxygen-sensitive luminescent materials can be used in the form of dyes when water-soluble [82], or embedded in beads [83], and sensor layers [84]. The latter two are preferred when toxicity is a concern.

Intensity imaging [85] is a widely used form of readout because it requires only a fluorescence microscope. However, its accuracy is limited by inhomogeneities in the light source and sensor structure. In contrast, fluorescence lifetime imaging (FLIM) provides highly accurate results. However, this method requires special equipment, which is not readily available in most research laboratories [83].

To mitigate this limitation, Ungerböck et al. have developed a two-wavelength ratiometric imaging technique [81], to achieve high-resolution imaging using inexpensive and readily available equipment. The signals are generated by two luminescent dyes that are excited by a blue light source. Platinum(II)-5,10,15,20-tetrakis-(2,3,4,5,6-pentafluorphenyl)-porphyrin (PtTFPP), which emits red light and whose emission is quenched in the presence of oxygen, and Macrolex Fluorescent Yellow (MFY) which emits the green reference light. A color camera's red and green channels were utilized to measure the intensities at the two different wavelengths. The signal of the reference dye MYF was recorded by the green channel, while the oxygen-sensitive signal of PtTFPP was recorded by the red channel.

By calculating the ratio of the two signals, the aforementioned inhomogeneities in the light source can be compensated. To calibrate the sensor, a non-linear Stern-Vollmer calibration curve is calculated using the equation:

$$\frac{R}{R_0} = \frac{f_1}{1 + K_{SV}\, p_{\mathrm{O}_2}} + f_2 \tag{2.2}$$

where R is the ratio of the red channel to the green channel at the corresponding partial pressure of oxygen p_{O_2}, while R_0 is the unquenched (deoxygenated) ratio, different fractions of dye molecules are described by f_1 and f_2, where the first describes a fraction of dyes quenched with a specific quenching efficiency K_{SV} and the latter the non-quenched fraction [81]. Such a calibration calculation is required for each individual sensor plate prior to measurement. To fabricate the sensor plates, the luminescent dyes are mixed in polystyrene, knife-coated to a glass plate, and optionally covered by a thin layer of PDMS to protect the sensing layer from scratches and delamination.

Instead of using oxygen sensing plates, optical fibers can be used. The oxygen-sensitive material will be applied to the tip on one end of the fiber, with the excitation and readout systems being located on the other end. Such a system offers great flexibility for measurements in complex environments such as the body. An *in vivo* measurement for partial oxygen pressure in the blood using optical fibers is described by Peterson and Fitzgerald [86]. An optical fiber system with 100 fibers and simultaneous read-out has been developed by Fischer et al. [87].

According to Brennan et al., optical measurements are the preferred choice for oxygen measurements in microfluidic systems. Compared to the electrochemical measurements based on Clark electrodes, the optical measurements do not suffer from fouling. Therefore, they are more suitable for long-term experiments with low or no flow and small medium volumes, as they also do not consume any oxygen. Additionally, they allow measurements over a greater area and do not require any electrical connections. [7]

2.8 Neuron cell culture device

To study neuronal networks with a focus on epilepsy, the NeuroGroup of Tampere University, together with the Micro- and Nanosystems Research Group, has developed and studied a brain-on-a-chip cell culture system called Modular Platform for Epilepsy Modeling *In Vitro* (MEMO) [5]. It consists of multiple components: a multi-electrode array (MEA), microfluidic chip, culture medium reservoir, plastic lid, PDMS gasket, and gas supply chamber, as shown in Figure 2.8.

Some of the system's highlights are that it allows the functional and structural development of human neuronal networks between the cell compartments with culturing times exceeding three months. Thanks to its gas control lid, it allows for MEA recordings with durations of several hours. Additionally, microscope monitoring of the cells and fixing and staining are possible. All these enable the controlled induction of seizure-like events to a specific network and study its effects on neighboring networks. The core piece is a microfluidic chip with three cell compartments connected by microtunnels. It is fabricated using PDMS molding. It has a height of 4 mm with a diameter of 22 mm. The three cell compartments are pentagonal in shape and connected by 50 microtunnels between each adjacent cell compartment. The microtunnels are 400 µm long, 10 µm wide, 3.5 µm high,

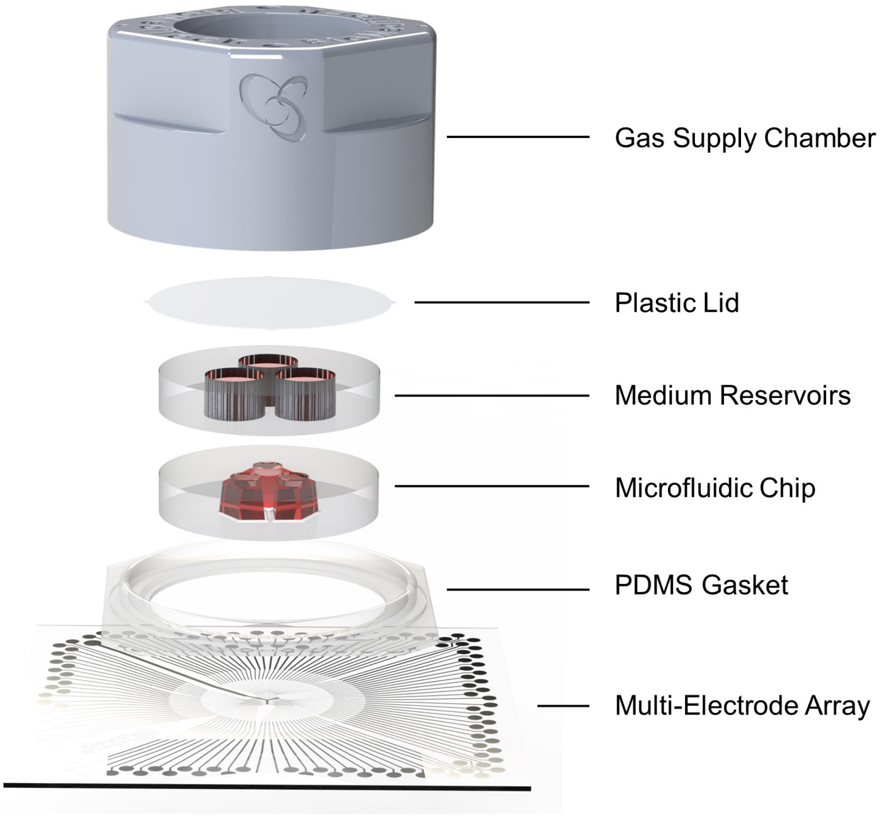

Figure 2.8. *Schematic exploded view of the MEMO cell culture system showing its components. Adapted from ref. [5].*

and have a spacing of 35 µm. These dimensions keep the neurons' somas separated between the cell compartments but allow axons to grow through and form a network. However, fluidically the cell compartments are well isolated from each other, which is critical for performing pharmacological tests targeted at cells in a single cell compartment. See Figure 2.9a for a schematic view of the microfluidic chip and its features.

An additional medium reservoir is placed on the chip to increase the amount of medium in each cell compartment and increase the time between each required medium change. It is 22 mm in diameter, 7 mm thick, contains three circular holes with a diameter of 6 mm, and is made of PDMS as well. In this configuration, each cell compartment has a medium volume of 200 µl. At the bottom of the system is a multi-electrode array on a 49 mm × 49 mm × 1 mm soda lime glass plate. The tracks and electrodes are made of 300 nm thick titanium (Ti) with an additional 300 nm thick titanium nitride (TiN) layer on top of the electrodes. As the insulation layer, a 500 nm thick silicon nitride (SiN) layer is deposited. There are 32 electrodes in each cell compartment, 8 of which are located under the microtunnels, plus an additional reference electrode. Figure 2.9b shows the locations of the electrodes. A PDMS gasket is bonded on top of the MEA plate to enable a tight seal for the gas supply lid that covers the system during measurements. The lid features gas-feeding openings through which cell culture gas (5 % CO_2, 19 % O_2, 76 % N_2) is supplied during long-duration MEA measurements to maintain appropriate pH and osmolality. Additionally, to prevent culture medium evaporation and contamination, the medium reservoirs are covered by a sterile transparent plastic lid.

The cell experiments utilize human pluripotent stem cells hPSCs. Before being plated on the MEMO chip, the cells undergo a pre-differentiation process of 32 days *in vitro*. It can take many weeks for the hPSC-derived neuronal cultures on the MEAs to reach functional

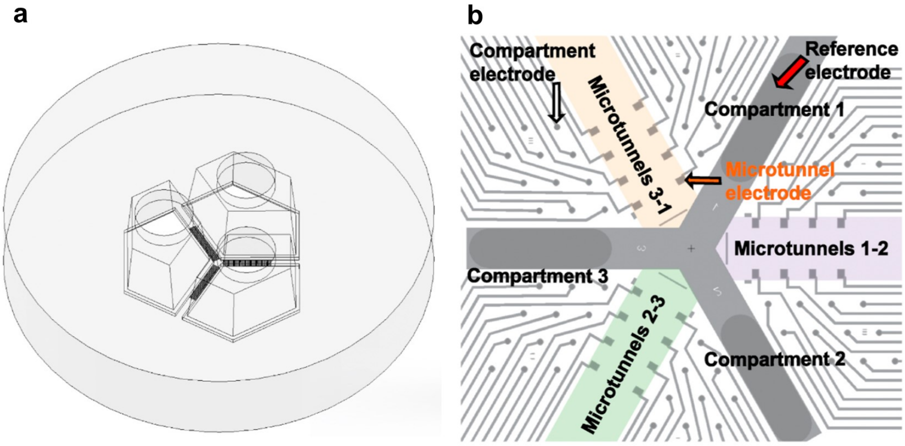

Figure 2.9. ***a:*** *Simplified view of the microfluidic chip displaying the three cell compartments and the microtunnels connecting them.* ***b:*** *MEA plate showing the locations of the 32 electrodes of each cell compartment. Eight of them are located toward the neighboring cell compartment under the microtunnels. Adapted from ref. [5].*

maturation. After approximately 55 days on MEMO, synchronous bursts appear that span all three cell compartments. These are seen as an indication of the functional maturity of the network [88]. From this day onwards until day 62, pharmacological experiments are conducted.

Seizure-like events are induced by administering a convulsant to Cell Compartment 1. Compared to the baseline, the number of bursts increased by as much as 214 %. Some minor burst count changes were observed in the neighboring cell compartments, but generally, it can be said that the effect of the drug did not spread to the neighboring cell compartments. Following up, an anticonvulsant was added to Cell Compartment 2. This drug did not decrease the burst rate per minute, but it reduced the overall level of electrical activity. This was seen as an indication that the connections to the neighboring cell compartments maintained the burst activity of cells in Cell Compartment 2. The network activity on the MEMO chip was maintained for at least 98 days. [5]

2.9 Numerical simulations

2.9.1 Simulation methods and models

The use of numerical simulations is growing in the development of microfluidic devices and in many other research fields. This is due to the many benefits that come from applying them. It can significantly improve the speed at which new approaches are developed and tested and reduces the need to build and characterize a prototype, which can yield substantial savings in costs. Furthermore, if set up correctly, numerical models can give considerable insight into a concept's functionality and characteristics, which can aid in developing novel designs. However, in the field of microfluidics, the number of publications that are dedicated to modeling is limited. [89]

There are a variety of numerical simulation tools used in microfluidics. The Lattice Boltzmann Method (LBM), for example, breaks down a fluid into a lattice of fluid density values which are used to simulate fluid flow. It is especially strong in modeling fluid flow, where the dynamics at the interface are important. [90] In the meshless Smoothed Particle Hydrodynamics (SPH) method, a fluid is represented as a collection of particles and is used in elastic and multiphase flow simulations. [91] A similar but more fine-grained approach is the Molecular Dynamics (MD) method. Here the single molecules and their interactions are modeled. It can be applied to simulate systems with liquids, gases, and solids, but it excels in biological applications to model processes such as protein folding [92]. [93] In the Finite Element Method (FEM), which is used in this work, a problem is simplified by breaking it down into smaller, easier-to-solve elements, which are triangles for two-dimensional and tetrahedrons for three-dimensional studies. The number of these elements is finite to enable computers to solve them. Therefore, the solution is always an approximation. To obtain the solution for the entire domain, the partial differential equations (PDEs) are solved by using a mesh to split the domain into a finite number of elements, with continuity enforced at the boundaries between neighboring elements. [94]

The accuracy of the approximation depends on many factors—the mesh density, for example. The finer the mesh that is used for the calculations, the more accurate the simulation will be. However, this comes at the cost of computing resources, which results in longer computing times or the requirement of a more powerful machine. In time-dependent simulations, a smaller time step is preferred to more accurately capture the changes that occur over time, although this comes again at the expense of increased computing resources [95], [96]. When pre-calculated or measured values are used to define, for example, material properties or other parameters used in the model, the accuracy at which they are obtained ultimately affects the results. The same applies to any assumptions or simplifications that are made when building the model. As mentioned earlier, greater accuracy often comes at the expense of computational power. However, there are some techniques that can be used to reduce the computational load while keeping the models accurate. One such feature is the usage of symmetry. When applicable to a model, only half or a quarter of the geometry is simulated. [97] Another way to reduce computational requirements is the usage of adaptive meshing. Here, a mesh is refined and designed more accurately and tighter in areas of specific interest or with smaller feature sizes while kept more coarse in less important areas. [98] If possible, the abstraction or simplification of a three-dimensional problem into a two-dimensional one can also significantly reduce the computational requirements, as it contains fewer nodes and requires fewer equations to be solved.

Buchwald [99], modeled the oxygen consumption of pancreatic islets to investigate the cell viability in standard culture conditions. He employed 2D and 3D models, which were solved as time-dependent problems until a steady state was reached. The oxygen concentration in the surrounding medium, as well as the flow velocities, were simulated, and different culture conditions were investigated. Lee et al. [100], employed FEM to model the oxygen scavenging capabilities of a newly designed microfluidic chip used for hypoxia experiments. A sodium sulfite scavenger was used, and the boundaries of the scavenger channel were considered as 0 % O_2 due to its rapid scavenging properties and the large enough flow rate. Medium oxygen concentration and the velocity profile were obtained as a result, and the oxygen concentration was verified using a ratiometric oxygen measurement. An extensive study investigating the oxygen transport in microfluidic cell culture devices using FEM was conducted by Zahorodny-Burke et al. [101]. They utilized a two-dimensional representation of their microfluidic chip, which features a channel on a glass substrate with an oxygen-permeable membrane on top and a thin layer of cells at the bottom of the channel. The channel is constantly perfused by cell culture media, and the cell's oxygen consumption is represented as an outward flux of oxygen out of the channel. The aim of the study was to find ideal material properties, flow rates, and chip geometries, such as the thickness of the oxygen-permeable membrane, to optimize the chip and guarantee sufficient oxygen supply to the cells.

2.9.2 Calculation of initial conditions

In PDMS-based cell culture devices, oxygen can be present in the solid, liquid, and gas phases, where solid refers to the PDMS, liquid to the cell culture medium, and gas to the air surrounding the culture chip. To model the oxygen transport between these phases, we need equations to describe it. The calculations used to model gas transport in a microfluidic system were initially proposed by Mäki et al. [102] for CO_2. In this work, they are adapted and modified to be used for O_2.

In the solid phase, diffusion is the only form of transport, while in the liquid and gas phases, transport will occur by convection and diffusion. Assuming that the oxygen concentration does not change over time, the mass balance in the system between its three domains is described by these four equations:

$$\begin{aligned} \frac{\partial c_{\mathrm{p}}}{\partial t} + \nabla \cdot J_{\mathrm{p}} = 0\,, \\ \frac{\partial c_{\mathrm{l}}}{\partial t} + \nabla \cdot J_{\mathrm{l}} + u_{\mathrm{l}} \cdot \nabla c_{\mathrm{l}} = 0\,, \\ \frac{\partial c_{\mathrm{g}}}{\partial t} + \nabla \cdot J_{\mathrm{g}} + u_{\mathrm{g}} \cdot \nabla c_{\mathrm{g}} = 0\,, \\ J_i = (-D_i \nabla c_i)\,, \end{aligned} \tag{2.3}$$

where u is the velocity field and the subscripts p, l, and g, denote the PDMS, liquid, and gas phases, respectively. Notice that the right side of the left-hand term that describes the transport due to convection is missing in the first equation, as diffusion is the only form of transport in PDMS. The equilibrium of O_2 concentration between two phases is described by the Equilibrium Expression 2.4 [103]:

$$c_{\mathrm{p}} \underset{k_{\mathrm{lp}}}{\overset{k_{\mathrm{pl}}}{\rightleftharpoons}} c_{\mathrm{l}}\,,\; c_{\mathrm{l}} \underset{k_{\mathrm{gl}}}{\overset{k_{\mathrm{lg}}}{\rightleftharpoons}} c_{\mathrm{g}}\,,\; c_{\mathrm{g}} \underset{k_{\mathrm{pg}}}{\overset{k_{\mathrm{gp}}}{\rightleftharpoons}} c_{\mathrm{p}}\,, \tag{2.4}$$

where c is the concentration in each phase, and k is the mass transport coefficient at the specific interface, with the subscripts indicating the direction. So k_{pl} denotes the mass transport at the interface from the PDMS phase to the liquid phase.

Under steady-state conditions, the dimensionless partition coefficients K_p can be obtained by the ratio of the previously introduced rate constants or the ratio of oxygen concentrations in each phase and can be expressed as [103]:

$$Kp_{\mathrm{lp}} = \frac{k_{\mathrm{lp}}}{k_{\mathrm{pl}}} = \frac{c_{\mathrm{p\_eq}}}{c_{\mathrm{l\_eq}}}, Kp_{\mathrm{lg}} = \frac{k_{\mathrm{lg}}}{k_{\mathrm{gl}}} = \frac{c_{\mathrm{g\_eq}}}{c_{\mathrm{l\_eq}}}, Kp_{\mathrm{pg}} = \frac{k_{\mathrm{pg}}}{k_{\mathrm{gp}}} = \frac{c_{\mathrm{g\_eq}}}{c_{\mathrm{p\_eq}}}, \tag{2.5}$$

with $c_{\mathrm{p\_eq}}$, $c_{\mathrm{l\_eq}}$, and $c_{\mathrm{g\_eq}}$ expressing the O_2 concentrations at equilibrium in the PDMS, liquid, and gas phases, respectively. The mass transport between the two domains can be modeled using the O_2 concentrations at both sides of the interface and their mass transport coefficients. The flux is described by the equations below, with a separate equation per interface: liquid-PDMS, liquid-gas, and PDMS-gas [103]:

$$\begin{aligned} J_{\mathrm{lp}} &= k_{\mathrm{lp}} c_{\mathrm{l}} - k_{\mathrm{pl}} c_{\mathrm{p}} = k_{\mathrm{pl}} (Kp_{\mathrm{lp}} c_{\mathrm{l}} - c_{\mathrm{p}})\,, \\ J_{\mathrm{lg}} &= k_{\mathrm{lg}} c_{\mathrm{l}} - k_{\mathrm{gl}} c_{\mathrm{g}} = k_{\mathrm{gl}} (Kp_{\mathrm{lg}} c_{\mathrm{l}} - c_{\mathrm{g}})\,, \\ J_{\mathrm{pg}} &= k_{\mathrm{pg}} c_{\mathrm{p}} - k_{\mathrm{gp}} c_{\mathrm{g}} = k_{\mathrm{gp}} (Kp_{\mathrm{pg}} c_{\mathrm{p}} - c_{\mathrm{g}})\,, \end{aligned} \tag{2.6}$$

where J is the flux with the superscripts lp, lg, and pg denoting the O_2 flux towards the interface of the second subscript at the interface of the first and second subscript; e.g., lp is the flux towards the PDMS phase at the liquid-PDMS interface. To describe the flux in the opposite direction, a minus sign is used. Next, the equilibrium concentrations in each phase must be found as they are used to find the partition coefficients K_{p}. Assuming O_2 is an ideal gas; we can describe it by the ideal gas equation:

$$p_{\mathrm{O_2}} V = nRT\,, \tag{2.7}$$

where $p_{\mathrm{O_2}}$, V, n, R, and T are partial pressure of O_2, volume, amount of substance, ideal gas constant, and temperature, respectively. The equation

$$c_{\mathrm{g\_eq}} = \frac{n}{V} \tag{2.8}$$

expresses the equilibrium concentration in the gas phase, where $c_{\mathrm{g\_eq}}$ is the equilibrated O_2 concentration. By rearranging Equation 2.7 for volume and substituting it into Equation 2.8, we obtain:

$$c_{\mathrm{g\_eq}} = \frac{p_{\mathrm{O_2}}}{RT} = \frac{Fv_{\mathrm{O_2}} p_{\mathrm{ch}}}{RT}\,, \tag{2.9}$$

where $Fv_{\mathrm{O_2}}$ is the volume fraction of O_2, and p_{ch} is the total chamber pressure used to describe the equilibrated O_2 concentration in the gaseous domain.

Henry's law, which states that the amount of dissolved gas is directly proportional to the partial pressure above the liquid, is used to obtain the equilibrated concentration of dissolved O_2 in a liquid and is written as:

$$c = kp\,, \tag{2.10}$$

where c is the dissolved gas concentration, k is the specific Henry's constant, and p is the partial pressure of the gas. However, the solubility is temperature-dependent. Therefore, we need to consider Henry's law as a function of temperature, as described by Sander [104] using Van't Hoff's equation:

$$k_{H(T)} = k_{H(\mathrm{SATP})} \exp\left[-H\left(\frac{1}{T} - \frac{1}{T_{\mathrm{SATP}}}\right)\right] , \tag{2.11}$$

where $k_{H(T)}$ is Henry's constant at experiment temperature T and $k_{H(\mathrm{SATP})}$ is Henry's constant at standard ambient temperature and pressure (SATP) T_{SATP}, which is defined by the International Union of Pure and Applied Chemistry (IUPAC) as 298.15 K, and H is a constant (in K) used for temperature-dependence. By calculating the reciprocal temperature-dependent Henry's constant [104] for O_2, which describes the volatility instead of the solubility, using Equation 2.11, we can rewrite Equation 2.10 into

$$c_{\mathrm{l\_eq}(T)} = \frac{p_{\mathrm{O_2}}}{k_{H(T)}} , \tag{2.12}$$

to solve for the O_2 concentration at equilibrium in the liquid. Here, $c_{\mathrm{l\_eq}(T)}$ describes the equilibrated O_2 concentration in liquid at the experiment temperature T. Lastly, we need to find the equilibrated concentration of O_2 in PDMS, which is dependent on the O_2 concentration of the gas above and the solubility of O_2 in PDMS and is expressed as

$$c_{\mathrm{p\_eq}} = S\, c_{\mathrm{g\_eq}} , \tag{2.13}$$

where $c_{\mathrm{p\_eq}}$ is the concentration of O_2 in PDMS at equilibrium and S is the solubility of O_2 in PDMS, calculated using the semi-empirical equation [66]:

$$S = S_{\mathrm{inf}}(1 + p_{\mathrm{ch}}\, n) , \tag{2.14}$$

where S_{inf} is the infinite solubility of the gas in the polymer, n is the pressure dependence of the solubility, and p is the pressure.

3. MATERIALS AND METHODS

This chapter covers the methodology that was used to select the designs and introduces the simulation approach that was used to evaluate them. Three different approaches for the manufacture of PDMS membranes with openings are presented. The entire manufacturing procedure for SU-8-based molds is introduced, followed by the assembly procedure of the chips and the oxygen measurements.

3.1 Design and design selection methodology

The current state-of-the-art cell culture chip introduced in Section 2.8 was used as a starting point for the hypoxia designs. Ideally, the resulting approach to lower the oxygen content in the cell culture area would have minimal impact on the currently established system, avoiding larger changes to already proven protocols and facilitating correlation with previously published work using the same cell culture chip.

Due to this, there were a few constraints applied to the possible designs. The biggest of them was the impossibility of adding any hypoxia structures below the cell culture area due to the MEA plate, which was used for electrical activity measurements during cell experiments. Furthermore, there were microtunnels connecting the cell compartments, which could not be modified, as well as the gas supply cover, which was required to maintain steady incubator-like conditions to keep the pH levels stable. However, the dimensions of the cover and chip were flexible and could have been increased if required. Other less stringent limitations were the size and shape of the cell compartment and the presence of the medium reservoirs.

The conceived designs were compared with each other using a weighted evaluation. The approaches were evaluated on the basis of fabrication complexity and potential success rate, the gradient of O_2, the speed of O_2 change, and potential acceptability by end-users on a 1-5 point scale, where higher scores indicate better performance. Fabrication took into account all necessary and expected fabrication steps, their difficulty, and their estimated success rate. A lower difficulty was rated with a higher number of points. The gradient point tried to estimate the size of the gradient due to the system, where a smaller, less steep gradient received a higher number of points. The speed of O_2 change considered the rate at which hypoxia can be achieved, with a faster system receiving more points. Possible acceptance by the end-users was a more objective factor that attempted to estimate how well the cell researchers would accept the solution. If a system required fewer changes to the researcher's current workflow and protocols, it received more points. Based on this evaluation, the two most promising designs were chosen for further investigation and comparison, which was done using FEM simulations.

The selected design, whose fabrication steps are described in the following sections, is briefly explained. However, for a detailed explanation of the design, the reader is referred to Section 4.1.

The design consisted of two layers of PDMS. The first layer was 200 µm thick and contained the microtunnels connecting the cell compartments as well as the openings for the cell compartment itself. This layer will be referred to as the microtunnel layer. Permanently bonded to the microtunnel layer was the second layer, which was approximately 3 mm thick. This layer contained a scavenging channel routed around a single cell compartment as well as the large section of the cell compartment and will be referred to as the scavenging channel layer. Within the cell compartment, a passive submerged oxygen-blocking structure is placed. This limits the oxygen scavenging effect to below the structure.

3.2 Simulation

All simulations were implemented using the commercially available software *COMSOL Multiphysics 6.1* (COMSOL AB, Stockholm, Sweden). Two models were built and simulated in 2D as a worst-case representation where the width of the cell compartment was set to the broadest section where the gradient would be the largest.

To simplify the model, several assumptions were made:

- Pressure and temperature are constant
- Henry's law and ideal gas law are valid
- No evaporation of culture media
- Only the transport of oxygen is considered
- The MEA plate below acts as a diffusion barrier (no flux)
- The flow of the scavenger is significantly greater than the oxygen diffusion speed. Therefore, no flow simulation was needed, and the oxygen concentration at the boundary of the scavenging channel was considered to be constant.

COMSOLs' inbuilt materials, Air, PDMS, and Water, were used to describe the material properties of the three domains. Air was used for the surrounding room air and the scavenging channel. PDMS was assigned for all solid structures produced by molding, and water was assigned for the culture medium within the cell compartments. The diffusion coefficients of oxygen close to 37 °C for all three phases were taken from the literature and can be found in Table 3.1. The diffusion coefficient of oxygen in culture media takes into account the salinity and protein content which slows down oxygen diffusion [26].

Using the mass transfer equations of the *Transport of Diluted Species* (TDS) module, the concentration change of dissolved oxygen by diffusion in the system was modeled. Therefore, a TDS physics module was added for each domain. The flux of oxygen between two adjacent domains was defined by adding *Flux Nodes* to each of the TDS modules, described by Equation 2.6. The concentrations there referred to the concentrations of the respective domains defined in the TDS module. The direction of the flux was represented by the sign, where one domain had a positive and the other a negative sign.

The starting conditions represented the chip sitting in an incubator at equilibrium at 37 °C with an oxygen concentration of 19 %. The oxygen concentration in an incubator was lower than the room air oxygen concentration (21 %) due to the additional partial pressure of water vapor and CO_2 [26]. The saturated oxygen concentrations in PDMS, air, and liquid were calculated using the Equations 2.7 - 2.14. Using the saturated concentrations and Equation 2.5, the partition coefficients Kp_{lp}, Kp_{lg}, and Kp_{pg} were calculated. The values for the mass transport coefficients k could not be found in the literature as these differ from system to system and would need to be measured. Here, however, estimated values based on previous simulations executed by Antti Mäki were used for k_{gp}, k_{gl}, and k_{pl}. As an oxygen scavenger, 100 % Nitrogen was used to create a gradient as steep as possible. The scavenger was present during the entire simulation and was modeled by a *Flux Node* at the scavenging channel boundaries, with the concentration in the scavenging channel being 0 %. An overview of the used simulation parameters is presented in Table 3.1. The mesh was set up using custom settings with a maximum and minimum element size of 50 µm and 0.05 µm, respectively. The maximum element growth rate was set to 1.05, the curvature factor to 0.2, and the resolution of narrow regions to 1.

Parametric sweeps were used to experiment with the oxygen concentrations that were applied to the scavenging channels as well as the size, position, and distance of the scavenging channels to the cells. The simulations were run as time-dependent to obtain the system's time constants, as well as static simulations to get steady-state gradients and oxygen concentrations. As a result of the models, a gradient image of the oxygen concentration within the medium in the range of 0 % to 19 %, as well as a plot of the concentration along the bottom boundary where the cells are located, was generated. The time constant was calculated based on the oxygen concentration change on a predefined point at the bottom of the cell compartment, 1.3 mm from the center wall separating the cell compartments. Therefore, a table of oxygen values with time points was exported to a MATLAB script, where a curve fit was applied. The time constant was obtained by scanning for the time point where the oxygen concentration dropped below 37 % of its starting value. The used script can be found in Appendix C.

The oxygen concentration in the culture media was converted from its molar concentration to the equivalent of the oxygen percentage in the air above for easier comparison. This was done using Henry's law (Equation 2.10) to obtain the partial pressure of oxygen, which was converted to a percentage using the ambient pressure.

Table 3.1. *Overview of the simulation parameters utilized in the study*

Parameter	Definition	Value	Source
$c_{\mathrm{g\_eq}}$	Saturated oxygen concentration in gas	$7.47\ [\frac{\mathrm{mol}}{\mathrm{m}^3}]$	calculated
$c_{\mathrm{l\_eq}}$	Saturated oxygen concentration in cell culture media	$0.20\ [\frac{\mathrm{mol}}{\mathrm{m}^3}]$	calculated
$c_{\mathrm{p\_eq}}$	Saturated oxygen concentration in PDMS	$1.35\ [\frac{\mathrm{mol}}{\mathrm{m}^3}]$	calculated
D_{air}	Diffusion coefficient of O_2 in air	$2.1 \cdot 10^{-5}\ [\frac{\mathrm{m}^2}{\mathrm{s}}]$	[27]
D_{medium}	Diffusion coefficient of O_2 in culture medium at 37 ℃	$2.69 \cdot 10^{-9}\ [\frac{\mathrm{m}^2}{\mathrm{s}}]$	[26]
D_{PDMS}	Diffusion coefficient of O_2 in PDMS at 35 ℃	$3.4 \cdot 10^{-9}\ [\frac{\mathrm{m}^2}{\mathrm{s}}]$	[28]
H	Constant to convert $k_{H(\mathrm{SATP})}$ to $k_{H(T)}$	$1700\ [\mathrm{K}]$	[104]
$k_{H(\mathrm{SATP})}$	Henry's constant at SATP	$77942\ [\frac{\mathrm{Pa}\cdot\mathrm{m}^3}{\mathrm{mol}}]$	[104]
$k_{H(T)}$	Henry's constant at experiment temperature	$97181\ [\frac{\mathrm{Pa}\cdot\mathrm{m}^3}{\mathrm{mol}}]$	calculated
k_{gl}	mass transport coefficient Gas-Liquid	$2 \cdot 10^{-5}\ [\frac{\mathrm{m}}{\mathrm{s}}]$	estimated
k_{gp}	mass transport coefficient Gas-PDMS	$2 \cdot 10^{-5}\ [\frac{\mathrm{m}}{\mathrm{s}}]$	estimated
k_{pl}	mass transport coefficient PDMS-Liquid	$2 \cdot 10^{-3}\ [\frac{\mathrm{m}}{\mathrm{s}}]$	estimated
Kp_{lg}	Partition coefficient Liquid-Gas	$37.69\ [-]$	calculated
Kp_{lp}	Partition coefficient Liquid-PDMS	$7.75\ [-]$	calculated
Kp_{pg}	Partition coefficient PDMS-Gas	$4.86\ [-]$	calculated
n	Pressure dependence of solubility	$4.9e-3\ [\frac{1}{\mathrm{atm}}]$	[66]
p_{ch}	Chamber pressure	$1\ [\mathrm{atm}]$	defined
R	Universal gas constant	$8.3145\ [\frac{\mathrm{J}}{\mathrm{mol}\cdot\mathrm{K}}]$	constant
S_{inf}	Solubility of O_2 in PDMS at 35 ℃	$0.18\ [\frac{\mathrm{cm}^3(\mathrm{STP})}{\mathrm{cm}^3\cdot\mathrm{atm}}]$	[66]
T	Experiment temperature	37 ℃	defined
T_{SATP}	Temperature as defined by SATP	25 ℃	constant

3.3 Open membrane manufacturing tests

Three methods to produce thin PDMS membranes with openings using plates were tested in this work. The first one used a 3D-printed plate produced in a stereolithography (SLA) printer using a resin that was found to inhibit PDMS crosslinking. The second used an untreated polycarbonate plate, while the last utilized a special coating of [3-(2-Aminoethylamino)propyl]trimethoxysilane (AEAPS, Sigma Aldrich, USA) on glass plates that prevents PDMS from cross-linking. In all three methods, which are also described in Section 2.6, the plate was pressed onto the mold structures to create an even top layer and, if successful, the openings.

For the first approach, three plates with thicknesses 3 mm, 4 mm, and 5 mm and size 72 mm × 72 mm were 3D-printed in a vertical orientation to reduce warping using an SLA 3D-printer (Form 3, Formlabs, USA). A clear resin (clear V4, Formlabs, USA) was used for printing as it prevented PDMS crosslinking. After printing, they were washed in a specialized washing machine (Form Wash, Formlabs, USA) and partially cured in a UV oven (Form cure, Formlabs, USA) at 60 ℃ for 15 min. A full cure was not desired as there should be enough of the crosslink inhibiting substance freely available. To enhance the surface quality of the plates, they were wet-sanded using sandpaper with increasing grain sizes of 400, 1,200, 2,000, and 3,000.

For the test using the polycarbonate plate, a rectangular plate of 75 mm × 75 mm with a thickness of 3 mm was sawn out from a larger plate using a bandsaw. Care was taken not to scratch the surface of the plate that will be applied to the PDMS, as these will transfer to the PDMS layer, complicating further processing, specifically bonding and sealing properties.

To treat the glass plates with AEAPS, the following procedure was used. Ten microscope slides with size 75 mm × 38 mm (2947-75X38, Corning, USA) were placed in a special piece of glassware to hold them upright. Images and a more detailed description of the glassware can be found in Appendix A. A glass container was filled with methanol, and 2 % w/w of AEAPS was added using a pipet. The mixture was thoroughly stirred using a glass stick. Then, the glass plates within the holder were submerged in the methanol-AEAPS mixture for 1 h. Subsequently, the plates were removed and placed within the holder in a preheated oven (UN55, Memmert, Germany) for 30 min at 110 ℃ to covalently link the AEAPS molecules to the glass plates. All the work was done in a fume hood wearing methanol-resistant butyl gloves to reduce the risk of accidents. See Figure 3.1 for a depiction of the working environment. Once the plates were placed in the oven, the lab was emptied and closed for 30 min to allow the methanol vapors to escape by the room ventilation.

The molding tests were done using an old decommissioned mold which had a height

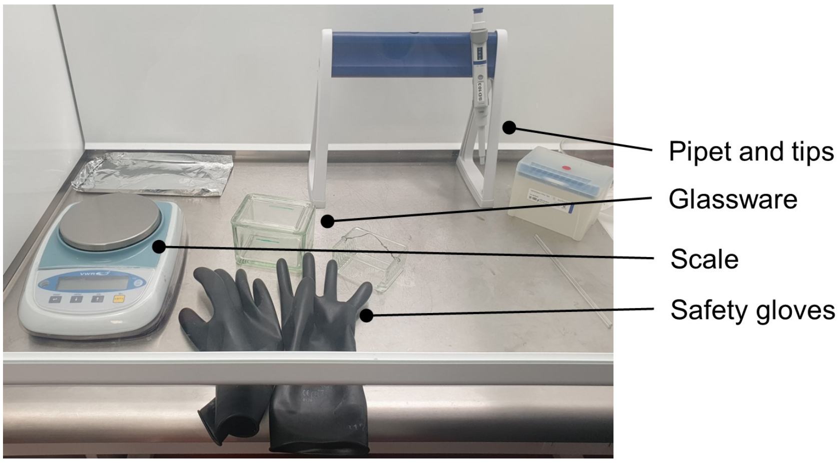

Figure 3.1. *Required equipment used to coat glass plates with AEAPS in a fume hood.*

of 200 µm and featured similar geometries as were planned to be manufactured later on. PDMS (Sylgard 184, Dow, USA) was mixed in a ratio of 10:1 w/w of the base to crosslinker. The mixture was thoroughly stirred and degassed. After pouring it into the mold, another degassing cycle followed to remove bubbles that remained in the PDMS as well as those that occurred during the pour. Then the plates were first applied to one edge of the mold and then carefully lowered onto the PDMS so that the meniscus of the PDMS was in contact with the mold and the plate and moved steadily forward (see Figure 3.2) to prevent air pockets from getting trapped under the plate, as they were nearly impossible to remove once the plate was fully applied.

A weight was applied to the plates to squeeze out as much PDMS as possible between the SU-8 structures of the mold and the plates. The PDMS was cured in an oven (UF75M, Memmert, Germany) for 10 h at 60 ℃. With the inhibiting glass plates, an alternate curing procedure at room temperature for three days was tried as well in an attempt to reduce the adhesion strength of PDMS to the glass plates.

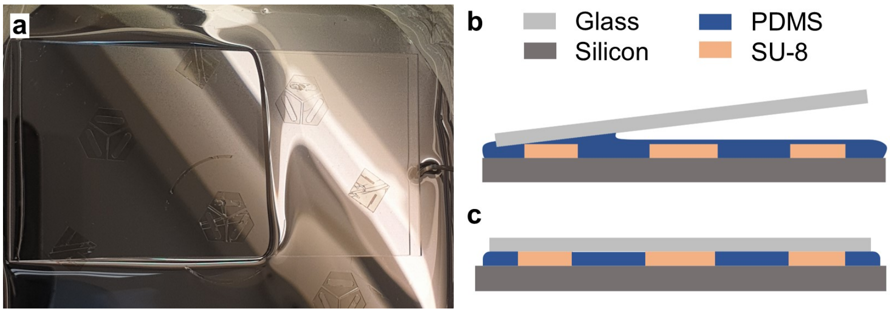

Figure 3.2. *Application of plates.* ***a:*** *Image of a glass plate getting applied onto the mold. The meniscus of the PDMS between the mold and glass plate wandering from left to right is visible.* ***b:*** *Schematic of the plate on the mold with the meniscus between PDMS and plate.* ***c:*** *Schematic of the fully applied plate. Note that the possible residual PDMS layer between SU-8 structures and the plate is not shown here.*

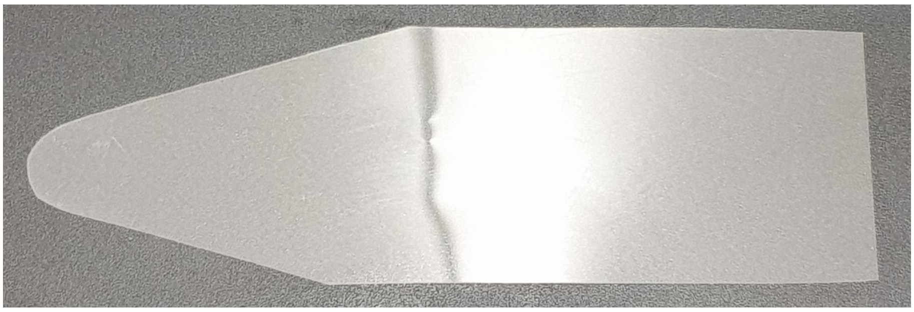

Figure 3.3. *The custom wedge tool that was cut out from a PET film. The rounded edge on the left side is wedged between the PDMS and the glass plate. The right rectangular side forms the handle.*

After the PDMS cure, the plates were removed, and the resulting membranes were investigated for their surface quality and the quality of the opened cavities. On the treated glass plates, the PDMS adhered so strongly that it was demolded upon the liftoff of the glass plate. Therefore, different methods to remove the thin PDMS membrane from the inhibiting glass plates needed to be tested. A peel-off at different angles relative to the glass plate was tried, as well as swelling the PDMS in the solvents acetone and isopropyl alcohol (IPA). Another tested lift-off approach was wedging a 1 mm thick polyethylene terephthalate (PET) film between the PDMS and the glass plate. Therefore, a custom tool was crafted by cutting out a long piece with a wide rounded tip out of the PET film, as shown in Figure 3.3. The rounded edge should be easier on the PDMS, reducing the risk of ripping. To give the tool more stability and prevent it from buckling while wedging it in between, the rectangular handle side was bent into a slight U-shape.

3.4 Mold fabrication

The molds were fabricated using photolithographic processes to achieve small feature sizes at good quality. This manufacturing procedure consisted of several steps, which are explained in detail below, but a short summary is given here. First, the chip geometries were drawn as 2D sketches using CAD software. These were then turned into a photomask that was used to transfer the patterns employing UV light into a layer of SU-8 which was spun onto a silicon wafer. The unexposed SU-8 was removed, with the exposed areas forming the protruding features onto which the PDMS was molded. Two molds were fabricated. The mold for the microtunnel layer, hereafter referred to as Mold 1, contained two layers of SU-8, defined as Layer 1 and Layer 2, in the order in which they were applied. The mold for the scavenging channel layer is referred to as Mold 2 and consists of a single layer of SU-8 defined as Layer 1. Mold 2 is a micro-macro mold, which used a combination of SU-8 and 3D-printed structures to achieve larger heights than are possible with sole SU-8 molds, and therefore required additional fabrication steps.

3.4.1 Mask design and fabrication

Based on the final design for the scavenging channels and cell compartments, the masks were created. These were built on the template created by Jari Väliaho from the Micro- and Nanosystems research group at Tampere University. These templates include all the necessary tolerances as well as the alignment marks for creating multi-layered structures. The masks were drawn using AutoCAD (Autodesk, USA) based on three-dimensional designs, which were exported as 2D sketches from the modeling software (SolidWorks, Dassault Systemes, France). Five chips were arranged on one wafer, so with one molding step, five chips could be fabricated. Care was taken for the multi-layered mold masks so that the chip structures were perfectly aligned between them. See the first three images in Appendix B for schematics of the masks. In the final step, the chip geometries were scaled up by 1 % to account for the shrinkage of PDMS. For the initial three masks, the mask files were then sent to a service contractor (Micro Lithography Services, UK) for manufacturing. As a mask type, a chromium mask on soda-lime glass was selected, where the chrome areas are opaque and block the UV light.

Later, an updated mask for the scavenging channel layer featuring ten chips of five different sizes, with two of each size, was fabricated in the cleanroom. The layout of this mask is shown in the fourth picture of Appendix B. A specially prepared mask blank with a chrome layer and a pre-spinned positive photoresist layer was used (CBL5009Du-AZ1500, Clean Surface Technology, Japan). The mask was placed in a mask writer (µPG501, Heidelberg Instruments, Germany). First, the mask writer converted the mask file into a set of instructions which it then executed to expose the photoresist. The exposed resist was then removed using a developer (AZ726 MIF, MicroChemicals, Germany) by submerging it for 1 min. Subsequently, the mask was submerged for 1 min into an etchant (Chrome Etch 18, micro resist technology, Germany) to remove the exposed chrome layer. The mask was then thoroughly rinsed with DI water and dried using pressurized nitrogen. To remove the remaining photoresist, the mask was placed for 1 min in a prewarmed UV-oven (UV-F 400, Panacol-Elosol, Germany) to expose the entire photoresist layer, followed by another development of 1 min in AZ726 MIF. Before their use, all the masks were checked for their quality, imaged, and measured using a microscope (BX53M, Olympus, Japan).

3.4.2 Photolithography

Two different photolithography resists were used during the following described processes. These were SU-8 5 (Kayaku Advanced Materials, USA) and SU-8 3050 (Kayaku Advanced Materials, USA). The first was a very thin resist with a viscosity similar to water, suitable for thin layers, while the latter was thick like honey and used for thick layers. Both were negative photoresists, where the areas exposed to UV light get insoluble to the developer, remaining as solid structures. Two molds were produced, with Mold 1 featuring a 3.5 µm thick layer for the microtunnels (Layer 1) and a 200 µm layer on top to form the start of the cell compartment (Layer 2). Mold 1 contained only a 200 µm thick layer as the base of the cell compartment (Layer 1) to which the 3D-printed inserts were glued in a later step.

Immediately before the lithography, the silicon wafers were cleaned using oxygen plasma (Pico, Diener Electronic, Germany). This was done to improve the adhesion of the SU-8 photoresists on the silicon by dehydrating the surface and removing organic contaminants on the surface. No time could be wasted before the next step, as this treatment was only temporary. The silicon wafer was then placed in a spin-coater (WS-650HZB-23NPPB, Laurell Technologies, USA) on a chuck of appropriate size, and a vacuum was applied to secure the wafer in place. Then, the resist was poured onto the wafer as centered as possible. This needed to be done carefully to try not to let the stream of SU-8 rip off, which might have introduced bubbles. The SU-8 was then spun to the desired film thickness using an automated spinning program, which has been set with resist-specific parameters, as shown in Table 3.2. In Figure 3.4 the applied photoresist is shown before the spin process (a) and after the spin process (b).

After spinning the photoresist, the vacuum was turned off, and the wafer was carefully removed. Therefore, the photoresist was wiped off at one narrow edge using an acetone-

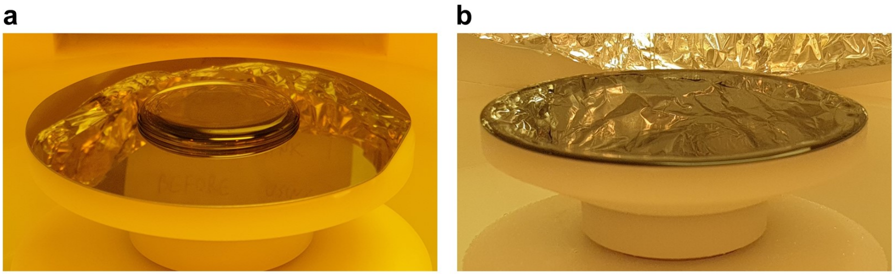

Figure 3.4. *SU-8 3050 on a wafer before (a) and after (b), spinning it to a thickness of 200 µm.*

Table 3.2. *Spin parameters for 3.5 µm and 200 µm thick SU-8 layers.*

Resist	Thickness	Step	Time	RPM	Acceleration
SU-8 5	3.5 µm	1	15 s	500	100
		2	40 s	4175	250
		3	10 s	100	500
SU-8 3050	200 µm	1	15 s	500	83
		2	40 s	700	249
		3	15 s	100	498

soaked cloth. It was important to exercise caution when applying the acetone to the cloth and when wiping not to spread any acetone onto the SU-8 layer as acetone breaks down uncured SU-8 which might have destroyed the layer. The wafer was then grabbed using special wafer tweezers and lifted out from the spinner. Caution was necessary when lifting out the wafer because excess photoresist, which was slung to the sides, could have dripped from the lid and ruined the smooth layer of SU-8. Furthermore, it was important not to tilt the wafer during this step as this can lead to an uneven photoresist film. Using an acetone-soaked cloth again, the bottom edge of the wafer was cleaned to remove any photoresist that might have flowed there. Failing to do so could have caused the wafer to stick to the copper plate in the next step.

The wafer was then placed on a copper plate with a handle for easier use and placed onto a hotplate (HS60, Torrey Pines, USA) set to 65 ℃. This was the first pre-bake step which lasted 1 min or 5 min, depending on the layer thickness, and used photoresist. Time measurement was started once the temperature measurement using a Type-K thermometer (72-7715, TENMA, Japan) showed 60 ℃. See Figure 3.5 for a representation of this setup. Subsequently, the wafer was placed on another hotplate (HS61, Torrey Pines, USA) set to 95 ℃. Here, time measurement was started at 90 ℃ and lasted for 3 min or 120 min, again depending on the layer thickness, and used photoresist. An overview of the pre-bake times can be found in Table 3.3 Once the pre-exposure bake was finished, the wafer was placed on an even surface to let it cool below 40 ℃. Placing it on a thermally well-conducting surface, such as metal, aids in cooling.

Then the wafer was placed into the mask aligner (J500, Optical Associates Inc., USA) on a vacuum chuck, and a vacuum was applied to fixate it. See Figure 3.6 for an overview of the device. At this step, it was good to make sure that the adjustment screws for the wafer alignment were in their middle positions so the maximum degree of freedom for the following alignment was available. The mask was placed over the wafer on a special

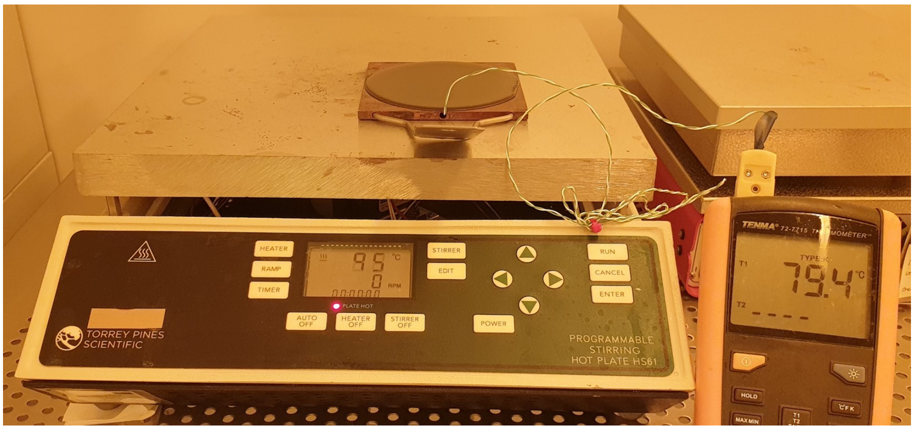

Figure 3.5. *The wafer on a copper plate on a hotplate set to 95 ℃ during the pre-exposure bake with ongoing temperature measurement.*

mask holder and fixated with a vacuum as well. A vertical adjustment screw was used to bring the wafer closer to the mask and into the focus plane of the microscope. An initial coarse alignment along the wafer edges was done with bare eyes using the alignment screws. Then the tower of the mask aligner was turned so the microscope was above the mask. Using it, the wafer flat was aligned with the mask, and the other edges were placed as centered as possible. When aligning the mask for Layer 2 of SU-8, this was done relative to the alignment marks, which were contained within the mask for Layer 1 and were now contained within Layer 1 of SU-8. Before the exposure, the wafer was brought into contact with the mask using the vertical adjustment screw. It was essential to press the "tilt"-button, which allowed the wafer chuck to compensate for any inclination between the mask and the wafer.

The tower was turned again, this time to bring the UV lamp above the mask. Exposure started automatically once this position was reached, and the tower swung back to its initial position once the exposure was finished. The exact exposure times for the respective photoresists and layer thicknesses are shown in Table 3.3.

After the exposure, the wafer was removed and placed again on the copper plate to go through the post-exposure bake steps. The temperatures and protocol were the same as before but with different timings, as listed in Table 3.3. The wafer was then again left to cool below 40 ℃ before the development was started.

The development of the resist was done via immersion in a ⌀115 mm borosilicate glass beaker filled with 1 cm of developer (mr-Dev 600, Microresist Technology, Germany). The beaker was placed on a vortex mixer (MS 3 basic, IKA, Germany) at low speed to facilitate the development through the movement of the developer to prevent local saturation. The wafer was kept for a minimum time in the developer, which is indicated in Table 3.3.

After development, the wafer was removed using wafer tweezers and immediately rinsed

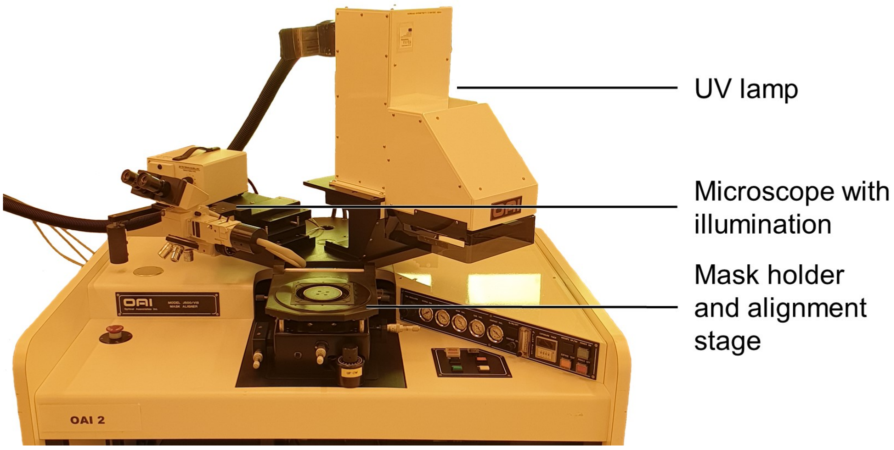

Figure 3.6. *Mask aligner with tower featuring microscope and UV lamp. In the center is the alignment stage with the wafer and mask holder.*

Table 3.3. *Pre-exposure bake, UV exposure, post-exposure bake, and development parameters (from left to right) for 3.5 µm (SU-8 5) and 200 µm (SU-8 3050) thick SU-8 layers.*

Thickness	65 °C	95 °C	Exposure	65 °C	95 °C	Development
3.5 µm	1 min	3 min	24 s	1 min	2 min	1 min
200 µm	5 min	120 min	54 s	5 min	10 min	15 min

with IPA to remove any remaining developer and resist. The wafer was dried by blowing off the IPA using pure pressurized nitrogen gas. An inspection under a microscope followed to consider if the development time was sufficient or if further development was necessary. If some remains of photoresist existed, the wafer was developed again in an iterative process for shorter durations with inspections in between until all unexposed resist was removed.

For the fabrication of Layer 2 of Mold 1, all previously described fabrication steps were repeated, starting from the oxygen plasma treatment. After all the layers were completely fabricated, the wafer was hard-baked in an oven (UF75M, Memmert, Germany) for 15 min at 150 °C to relieve internal tension and reduce cracks that emerged during processing. A fan speed of 30 % and a flap position of 0 % were used. It was essential to place the wafer in the cold oven before heating it and letting it cool down slowly to prevent temperature shocks. Besides relieving tension and cracks, this heat treatment fully polymerized the SU-8, increased its strength, and made it resistant to acetone.

Following the hardbake, the wafers were glued onto a ⌀105 mm and 2 mm thick glass plate using a double-sided adhesive sheet. The glass plate, in turn, was glued using the same tape into a ⌀120 mm Petri dish to facilitate the PDMS molding. This was done to give the wafer more rigidity and compensate for any curvature of the Petri dish.

3.4.3 Mold characterization

The molds were examined and measured during and after the manufacturing steps to assess layer quality before further processing. A microscope (BX53M, Olympus, Japan) was used to image at least partially each of the five chips on every SU-8 layer. For one of the structures defining the size of the cell compartment on each layer, optical-based measurements were done to assess the planar dimensions. Therefore, one inner edge of the pentagon that faces the scavenging channel was measured. For measurements of the layer height, a contact profilometer (DektakXT, Bruker, USA) was used. Each of the five chip geometries of each layer was measured to get insight into layer height and uniformity. Data analysis was done using the profilometer software. Therefore, the profile was leveled along two points so that the silicon substrate formed a horizontal line. The height measurement was done by placing one reference point on the silicon and the other

Table 3.4. *Measurement settings for DektakXT contact profilometer.*

Parameter	**Mold 1 Layer 1**	**Mold 1 Layer 2**	**Mold 2 Layer 1**
Range	6.5 µm	524 µm	524 µm
Length	300 µm	1000 µm	500 µm
Duration	30 s	100 s	50 s

on top of the SU-8 structures, with the software calculating the height difference between both.

All measurements were done as a standard scan and used a stylus with a tip radius of 2 µm and a contact load of 3 mg. Measurements were always started from the silicon, so the profile was selected as "Hills." Only the range, length, and duration were varied, whereby the duration was adjusted to the length to keep a constant measurement speed of 10 µm/s. All the varying parameters are listed in Table 3.4.

3.4.4 Fabricating and gluing of inserts

The inserts for Mold 2 are shown as a 3D model in Figure 3.7. These were 3D-printed using an SLA printer (Form 3, Formlabs, USA). A black resist (black V4, Formlabs, USA) was used for the prints because it did not inhibit the crosslinking of PDMS, unlike the clear resin. The prints were fabricated with a layer thickness of 25 µm to make the surface as smooth as possible. Once the prints were finished, the base plate with the parts was placed in a dedicated washing machine (Form Wash, Formlabs, USA) filled with IPA and washed for 10 min. Following the washing, the parts were manually rinsed with IPA, then deionized water (DI water), followed by another rinse with IPA, and then quickly dried using pressurized air. The parts with their support structures were removed from the base plate using a sharp blade and placed onto the supports in a Petri dish in which they were placed in a curing oven (Form cure, Formlabs, USA). The curing was done at 60 °C and under UV light for 30 min. Subsequently, the supports were snapped off. If needed, the remaining support structure was cut away using a scalpel. The inserts were again placed into the petri dish, this time facing the other way round, and cured for another 30 min as previously.

To glue the inserts to Mold 2, a two-component epoxy-based adhesive (Power Epoxy Universal, Loctite, USA) was used. Several mixtures were necessary due to the fast curing time. After a few minutes, the glue started to get thick and pull threads which complicated the gluing procedure as these threads can easily ruin the mold. Due to the pentagonal shape, the taper of the inserts, and the 120 degrees circular arrangement, two types of tweezers were used (see Figure 3.8). Narrow, slightly curved ones with flat heads, which held the insert nicely in place, were used to place the first two of three

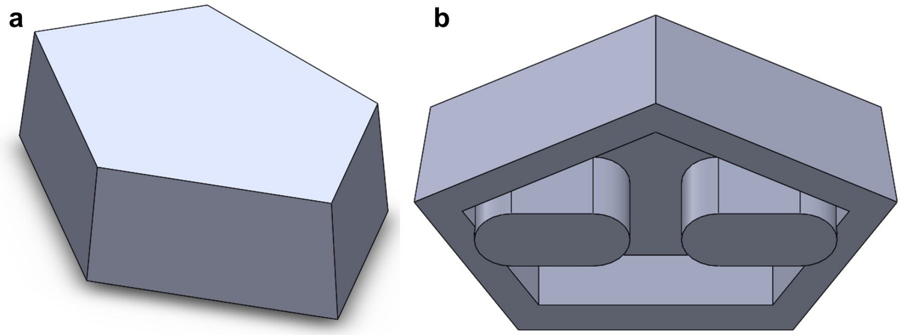

Figure 3.7. *3D model of the 3D-printed inserts used for Mold 2.* ***a:*** *Representation showing the pentagonal shape and taper of the insert.* ***b:*** *Bottom view of the insert with the two pins used for alignment with the SU-8 layer while gluing.*

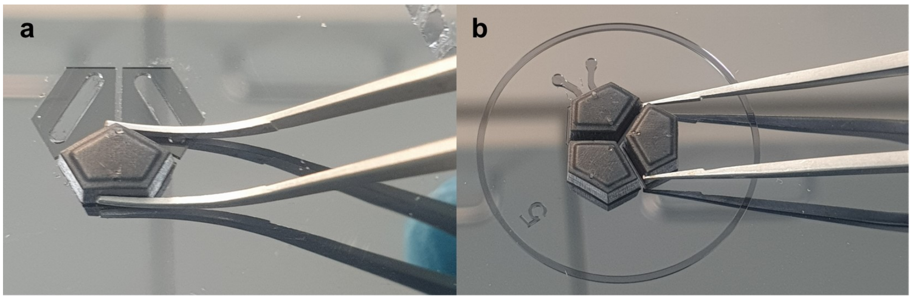

Figure 3.8. *Display of used tweezer types.* ***a:*** *Curved flat tweezers used for the first two inserts shown placing an insert on an old test mold.* ***b:*** *Narrow tweezers with small teeth to firmly grip the third insert from the sides.*

inserts per chip. However, for the third insert, the two already glued ones were in the way, so another type of tweezer was used, which had small teeth to grip the insert securely. These were used at the edges where none of the other inserts was in the way.

The glue was applied between the two pins using a piece of wire with approximately 1 mm diameter. The insert was carefully placed onto the SU-8 layer with the pins going into the slot. A dental excavator was used to press the insert down while the tweezers were removed to avoid accidental shifting. The cell compartments featuring the microtunnels were glued first as they are the ones where damage due to glue threads or misplacement is worst. The glue was left to cure for at least one day to achieve the best possible adhesion before further processing.

3.4.5 Silane coating

To facilitate the demolding properties of PDMS from Mold 2, it was coated with trichloro-(1H,1H,2H,2H-perfluorooctyl)silane which essentially acted as a non-stick layer. Therefore, the wafer was placed in a desiccator. A vacuum was applied on one side using a venturi valve. On the other end was a small container holding the liquid silane, which was evaporated due to the low pressure and pulled over the wafer. The venturi valve was used with water to create the vacuum because the water neutralized the corrosive chlorine gas created during evaporation. This treatment was done by Lassi Sukki and Juha Heikkilä from the Micro and Nanosystems research group at Tampere University.

3.5 Chip fabrication

Chip fabrication covers all required steps, from molding and demolding over the inlet punching, cleaning, and alignment to permanent bonding using oxygen plasma. For all PDMS molding procedures, the PDMS (Sylgard 184, Dow, USA) was mixed in a ratio of 10:1. The PDMS was thoroughly degassed within the mixing cup until there were almost no bubbles, then the PDMS was left to rest at ambient pressure, where small persistent bubbles popped, and then degassed one more time. The PDMS was never poured directly onto the SU-8 structures but always around. If done otherwise, bubbles can form. This was especially important for the mold containing the 3D-printed structures since it could not be degassed using a vacuum. The curing of the PDMS was done in a 60 ℃ hot oven for 10 h.

3.5.1 Fabricating the microtunnel layer with through-holes

Approximately 5 g of PDMS was poured into Mold 1 next to and around the SU-8 structures. The PDMS was given time to flow evenly over the structures and was aided if needed by tilting the mold. The mold was then placed in a vacuum chamber and evacuated to remove any bubbles that emerged during the pour.

A previously prepared round polycarbonate plate with (⌀90 mm) and thickness of 2 mm was applied onto the PDMS. Therefore, the plate was grabbed using tweezers, carefully aligned on one edge, and brought into contact. It was then gradually lowered onto the PDMS at an angle to allow air to flow away in front of the meniscus and not get locked in, as described in Section 3.3. A weight of 7 kg was placed onto the polycarbonate plate to squeeze out any excess PDMS between the plate and SU-8 structures. In between, a slab of PDMS with approximately 3 mm thickness was placed to aid in distributing the pressure more evenly and compensate for any height deviations (see Figure 3.9). To reduce the amount of PDMS between the SU-8 structures and the polycarbonate plate, the weight and the plate were turned so that the shear forces would remove as much PDMS as possible.

After the cure, the polycarbonate plate was carefully lifted off, and the PDMS remained within the mold for further processing. This way of processing simplified the alignment and bonding steps as it made sure the thin microtunnel layer stayed in its shape and did not deform.

Before molding new microtunnel layers in Mold 1, it was first cleaned using pressurized

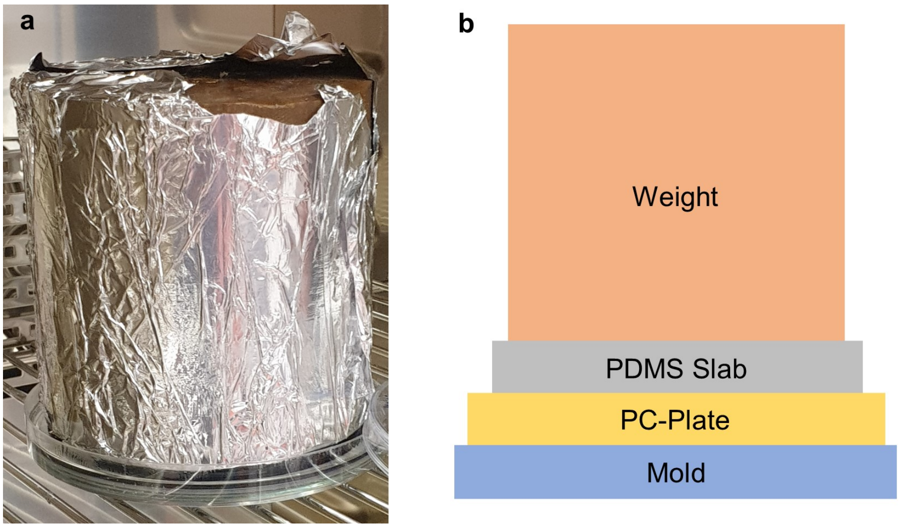

Figure 3.9. a: *Mold with an applied polycarbonate plate and PDMS slab for even pressure distribution and weight in the oven.* ***b:*** *Schematic depiction of the stack of layers.*

air, which was followed by a wipe using an acetone-soaked cloth (TX2069, Texwipe, USA). Then the mold was held vertically and rinsed with IPA, followed by DI-water, and subsequently dried using pressurized air. If needed, this procedure was repeated several times until the desired cleanliness was achieved.

3.5.2 Fabricating the scavenging channel layer

In the first molding procedure for the scavenging channel layer using Mold 2, 35 g of PDMS was poured into the mold. In all follow-up moldings, only 25 g of PDMS were used. This difference was due to the edges of the mold filling with PDMS, which was not cut out when demolding the chips. The molds were always filled first with only 15 g of PDMS, which was allowed to flow between the inserts. Once an even layer was formed, the remaining 10 g was poured into the mold, and the mold was carefully tilted to make sure the PDMS covered the inserts evenly. Vacuuming the PDMS within Mold 2 was not possible due to the glued 3D-printed inserts with their cavity surrounding the pins, which would have caused the PDMS to flow under them, causing larger flaps and, in the worst case, detach the insert when demolding.

To demold the chips, the PDMS was cut into smaller fractions around the chips using a scalpel. The chips were then carefully lifted off using tweezers, a dental excavator, and by hand. The lifting was approached from various sites, carefully pulling upwards and monitoring the PDMS to make sure it did not rip. Special care was necessary around the cell compartment with the microtunnels as the PDMS was relatively thin here and could have ripped easily.

The inner sidelength of one edge of the pentagonal cell compartment on the demolded chips was measured with a microscope (BX53M, Olympus, Japan). The same microscope was utilized for measuring the masks and molds. The shrinkage of PDMS was calculated using this equation:

$$Shrinkage = \frac{Original\,size - Measured\,size}{Original\,size} \times 100\,, \tag{3.1}$$

where $Shrinkage$ was the shrinkage in percent, $Original\,size$ the theoretically expected size or in this case, the size of the mold, and $Measured\,size$ was the real measured side length of the edge in the chip.

Once demolded, the inlets and outlets for the scavenger as well as the outer diameter of the chip, were punched. The former were punched with a self-made punch made from a size 18G syringe needle, and the latter were punched with a 22 mm punch using a press to ensure straight edges. The top of the chip above the inserts was cut open using a scalpel. Therefore, the chip was placed with the top side onto a glass plate and pressed onto it to make sure it adhered well there to prevent the PDMS from moving during the cutting. Then the PDMS was cut out as close as possible along all five cell compartment walls to create an opening of the same pentagonal shape. Using tweezers, the PDMS was carefully pushed out.

Before the next scavenging channel layers were manufactured in this mold, it was cleaned using pressurized air. Care was necessary not to use too much air pressure, which could have detached the glued inserts.

3.5.3 Alignment and bonding of microtunnel and scavenging channel layers

The microtunnel layer remaining in Mold 1 was only cleaned by carefully blowing it off using pressurized air. The scavenging channel layer was cleaned by wiping it in circular motions on an acetone-soaked cloth (TX2069, Texwipe, USA). This was followed by a rinse with IPA, then DI-water, and dried using pressurized air. The cleaned chips were placed in a new and clean Petri dish and inspected for their cleanliness using a microscope (090-131.002, Leica Mikroskope & Systeme, Germany). If needed, another cleaning cycle was done.

Before the parts were placed in the plasma machine (Pico, Diener Electronic, Germany), a pipe purge program was run to make sure the pipes were purged of all other gases and filled with 100 % oxygen to ensure the ignition of the plasma. Both layers were placed within a Petri dish in the metal tray (see Figure 3.10) of the plasma machine with the surfaces that were bonded facing upwards so that they were exposed to the plasma. A program optimized for bonding PDMS to PDMS was run with the parameters listed in Table 3.5.

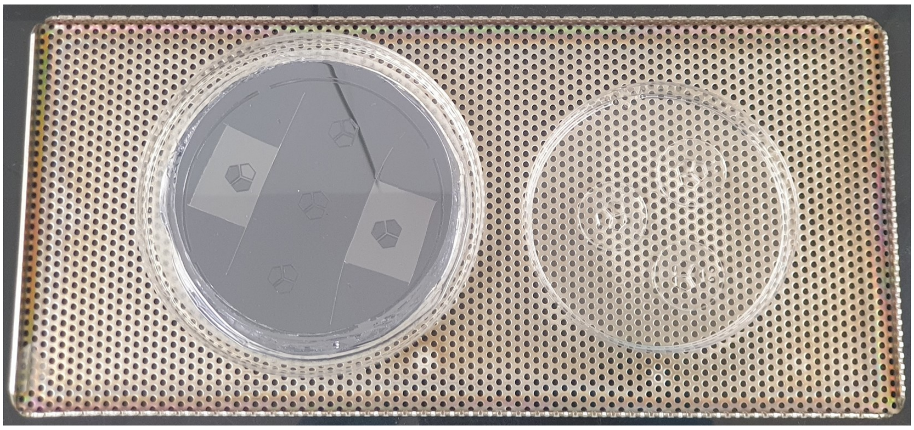

Figure 3.10. *Chip layers arranged in the metal tray of the plasma machine with the surfaces that are going to be bonded to each other facing upwards.*

Table 3.5. *Plasma treatment parameters for bonding PDMS to PDMS and hydrophilization of the assembled chips.*

Parameter	PDMS-PDMS bonding	Hydrophilization
Pumpdown pressure	0.25 mBar	0.25 mBar
Gas supply pressure	0.30 mBar	0.30 mBar
Plasma duration	20 s	5 min
Power	30 %	30 %
C1	18	18
C2	61	61

Immediately after the plasma treatment, the layers were transferred to a clean working environment where the alignment machine (FINEPLACER, Finetech, Germany) was located (see Figure 3.11). The scavenging channel layers were placed on small 22 mm × 22 mm microscope slides (631-0125, VWR, USA) with the cell compartment containing the scavenging channels centered on the plate. This enabled the scavenging channel layer to be fixated on the vacuum holder and allowed for rotational adjustment of it if needed. Additionally, these small glass slides were advantageous as the space in the alignment machine was very limited when lowering the scavenging channel layer (see Figure 3.12b) and also prevented a collision with already bonded chips or the wall of the mold.

The microtunnel layer was placed below on a platform and was aligned using a camera system that overlays the image of both layers on a computer monitor (see Figure 3.12a). Initial alignment was done in XY-position coarsely by hand, with the rotation aligned as accurately as possible. The precise XY adjustment was made using fine adjustment screws. Once both layers were aligned, the lever was actuated to bring them into contact and permanently bond them together.

Figure 3.11. *The alignment machine which was used to align and bond both layers accurately.*

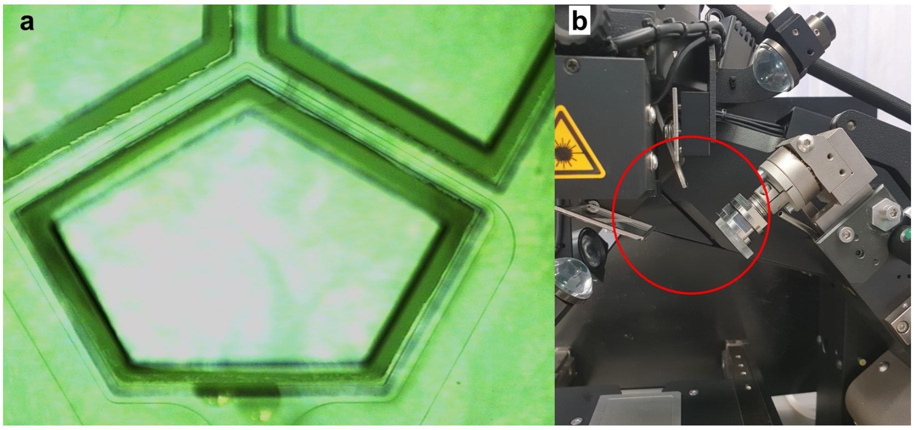

Figure 3.12. ***a:*** *Screenshot of the two aligned layers as seen on the monitor of the alignment machine.* ***b:*** *Depiction of the tight space for the scavenging channel layer when the lever is actuated, highlighted by the red circle.*

After all plasma-treated chips were bonded, a weight of 530 g was applied to them for at least 10 min to facilitate an even bonding. Subsequently, the microtunnel layer was cut around the scavenging channel layer using a scalpel and the stacked chip was carefully demolded.

3.5.4 Finalizing chips

After the assembly of the chips, they were sorted by quality. The evaluation was done based on the size of the flaps present in each layer and the alignment quality. The best chips underwent a leakage test for the scavenging channel. Therefore, the chip was temporarily bonded to a glass plate using PDMS inherent adhesion, and the cell compartments were filled with DI water. Inlets and outlets were connected, and a constant air pressure of 100 mBar was applied to one side of the scavenging channel, regulated by a pressure controller (OB1 MK4, Elveflow, France). The DI water-filled cell compartments were observed for any buildup of air bubbles.

A final thorough cleaning was conducted in the same way the scavenging channel layers were cleaned before bonding. Therefore, the chips were cleaned by wiping them in circular motions on an acetone-soaked cloth (TX2069, Texwipe, USA), followed by a rinse with IPA, then DI-water, and dried using pressurized air. An optical cleanliness assessment was done under a microscope (090-131.002, Leica Mikroskope & Systeme, Germany).

3.6 Oxygen measurements

The used ratiometric oxygen measurement plates were fabricated by Hannu Välimäki from the Tampere University Micro- and Nanosystems research group. They consisted of a 49 mm × 49 mm glass plate which was knife-coated with a 10-20 µm thick layer of polystyrene containing 0.5 % m/m of the oxygen-sensitive dye PtTFPP and 1 % m/m of the reference dye MFY. To prepare these plates for the measurement, they were coated with a 10 µm thick layer of PDMS using a spin-coater (WS-650MZ-23NPPB, Laurell Technologies, USA). The specific spin parameters are shown in Table 3.6. The chip was placed on the uncured PDMS layer on the measurement plate and cured for 10 hours in the oven. This way, the PDMS layer acted as an adhesive fixating the chip and protected the polystyrene sensor layer from scratches and delamination.

To fixate the sensor plate and chip mechanically to prevent movement during the measurement from disturbing the data, a custom mount was designed and 3D-printed. It featured a slot where the measurement plate with the chip was placed, as well as two down-holder clamps to fixate a cover. The structure was designed to fit the microscope slide holder. The cover was designed to be flexibly placed on the plate above the chip. It featured an inlet and outlet to supply gas for a controlled atmosphere surrounding the chip, as well as two holes through which the chip's scavenging channels were connected. The cover was held down by two clamps of the mount. A small glass plate with a diameter of 15 mm was glued to a small window at the top of the cover. A CAD model of the mount and cover is provided in Figure 3.13.

To supply the gases for the calibration and measurement, a manual valve system featuring six 3-way valves in series was connected to the inlet of the chip, while the other ends

Table 3.6. *Spin parameters for a 10 µm thick PDMS layer.*

Step	Time	RPM	Acceleration
1	15 s	500	100
2	60 s	4000	500
3	10 s	100	500

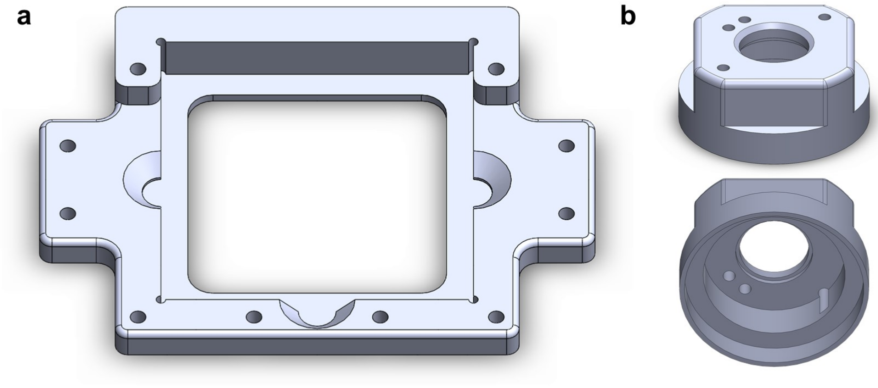

Figure 3.13. *CAD model of the 3D-printed measurement setup.* ***a:*** *The mount with a squared recess to fit the 49 mm × 49 mm oxygen measurement plates. It features three pockets for simplified removal of the plates, additional holes for fixation, and two holes on the slightly elevated backside for fixation of the down-holder clamps.* ***b:*** *The cover has four inlets and outlets. The two close to each other in one corner are used to connect the scavenging channel from the chip itself while the other two at opposing sides are used to flow gas through the cover.*

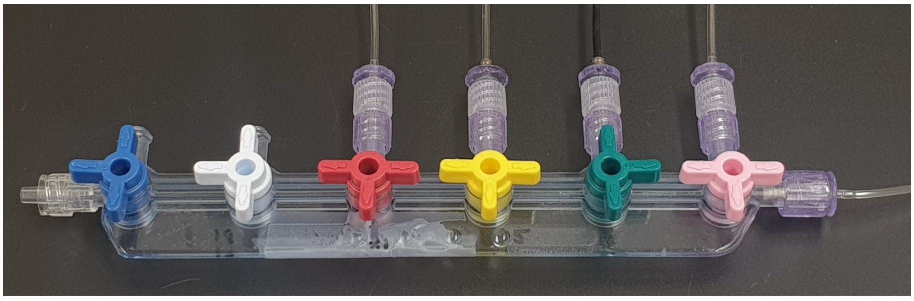

Figure 3.14. *The valve system that was used for the application of the scavenger gases. It features six 3-way valves connected in series. The right outlet was connected to the chip, while the first four valves from the right were connected to four bottles of known oxygen concentrations. In this specific configuration shown in the picture, the gas of the bottle connected to the second (green) valve was routed to the chip.*

were connected to bottles with various known oxygen concentrations. This valve system is depicted in Figure 3.14 and allowed for gas changes without touching the chip.

Additionally, an automated valve system shown in Figure 3.15 was used to apply the calibration gases overnight for the second and third measured chips. This system was built and programmed by Joose Kreutzer from Tampere University Micro- and Nanosystems research group. It featured four valves powered by a solenoid valve driver and controlled by an Arduino Uno. This setup allowed for the connection and timed control of gases of four different oxygen concentrations.

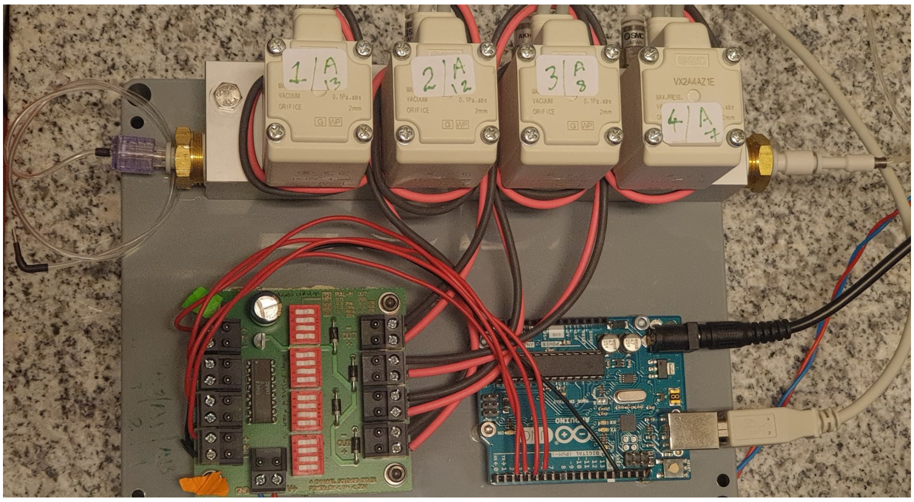

Figure 3.15. *Automatic valve system for the timed application of oxygen calibration gases overnight.*

3.6.1 Measurement execution

To configure the microscope (Axio ObserverZ1, Carl Zeiss, Germany) for oxygen measurements, the fluorescent lamp was replaced by a blue LED lamp which was used for the excitation of the luminescent dyes within the sensor layer. Due to a small medium volume of 60 µl in each cell compartment and a long experiment time of several hours, no heatplate was used. Instead, the experiments were conducted at room temperature compared to the 37 ℃ that was used in the initial simulations. To obtain a more reliable result, three chips were measured.

They were set up by filling each of the cell compartments with 60 µl of DI water. Then a submerged oxygen-blocking structure was applied to the scavenged cell compartment to limit oxygen diffusion and the other two cell compartments were covered with a piece of PET film to reduce evaporation. For an in-depth explanation of the submerged oxygen-blocking structure, the reader is referred to Section 4.1.6. Following this, the cover was applied and the chip's scavenging channel was connected through the cover using two steel tubes. The whole setup was placed in the slide holder of the microscope and the tubings were connected to it. The tubings were fixated using tape to prevent accidental movement and a matte black metal cover was placed over the chip to reduce reflections and other light disturbances. During the experiments, the light was off and the doors closed. The general sequence of the experiment started with the calibration where different gas mixtures with specific known oxygen contents were applied. Following this, the measurement was conducted. The calibration gases were only applied to the scavenging channel. An overview of the calibration gases and their compositions is given in Table 3.7. During the measurement, 19 % oxygen gas was applied to the cover while 99.999 % pure nitrogen was supplied to the scavenging channel. The duration for the application of the calibration gases was 75 min for the first chip.

Table 3.7. *Overview of the calibration gas compositions.*

Gas	Oxygen	Carbon dioxide	Nitrogen
Scavenger	0 %	0 %	99.999 %
1 % O_2 Gas	1 %	5 %	94 %
5 % O_2 Gas	5 %	5 %	90 %
10 % O_2 Gas	10 %	5 %	85 %
19 % O_2 Gas	19 %	5 %	76 %

However, when the experiments were run, adaptions to the procedure were made along the way. The specific changes are summarized in Table 3.8. For the experiments with Chip 2 and Chip 3 the chip as well as the submerged structure were hydrophilized prior to the application of DI water using oxygen plasma according to the parameters listed in Table 3.5. Additionally, the applied DI water was prewarmed in an incubator at 37 ℃ to avoid outgassing during the measurement. These measures were done to reduce the formation of bubbles. For both chips, the order of the experiment was changed as well, with the measurement being conducted before the calibration in order to prevent the chip from running dry due to the long calibration times. Other changes were the application of calibration gases to the chip and cover for significantly longer periods of time overnight and for the third chip the replacement of 19 % oxygen gas with 1 % oxygen gas.

Additionally for Chip 3, a measurement using sodium sulfite as a liquid oxygen scavenger to reach true zero oxygen concentrations was conducted. Therefore, a solution of sodium sulfite (Na_2SO_3) in DI water was prepared in the ratio 1:10 w/w. After the normal measurement, the chip was disassembled and the scavenger solution was applied, reassembled, and measured for 1 h.

Table 3.8. *Overview of the parameters used for the three measured chips.*

Parameter	Chip 1	Chip 2	Chip 3
Hydrophilization	No	Yes	Yes
Water prewarmed	No	Yes	Yes
Gas application during calibration	Chip only	Chip & cover	Chip & cover
Calibration duration per gas	75 min	5 h	3 h
Measurement point	after calibration	before calibration	before calibration
Applied calibration Gases [%]	0, 5, 10, 19	0, 5, 10, 19	0, 1, 5, 10
Gases used in analysis [%]	0, 5, 10	0, 5, 10	0, 1, 5, 10

3.6.2 Data analysis and comparison to simulation data

The data was analyzed using custom software programmed in MATLAB by Silmu Valaskivi and Hannu Välimäki. With it, the captured calibration images were loaded for analysis, and a rectangular region of interest (ROI) was defined in the area of the scavenging channel. This specific region was chosen because the change in intensity occurred rapidly and was largely unaffected by other influences. In this ROI, the ratio of the measured light intensities at steady-state time points (referenced via the image index) was associated with the applied oxygen concentrations. Therefore, the software calculated a Stern-Vollmer calibration curve by fitting the ratios to the defined oxygen concentrations. Then the measurement data was analyzed. An ROI covering the entire chip was defined and split into a grid with a cell size of 50 $\times$ 50 pixels. For each cell, the average oxygen value was calculated using the previously obtained calibration curve. Two sets of data for comparison with the simulations were extracted from each measured chip. One was the oxygen concentration profile along a line in the middle of the cell compartment at the final time point of the measurement. The other was the oxygen concentration at a defined point 1.3 mm from the center of the chip along this line over the entire measurement duration to obtain the time constant. The location of both of them is shown overlayed in a brightfield image of the third chip in Figure 3.16. Additionally, colored oxygen maps for four time points of the measurement were generated.

Due to the temperature change between the initial simulations run at 37 °C and the mea-

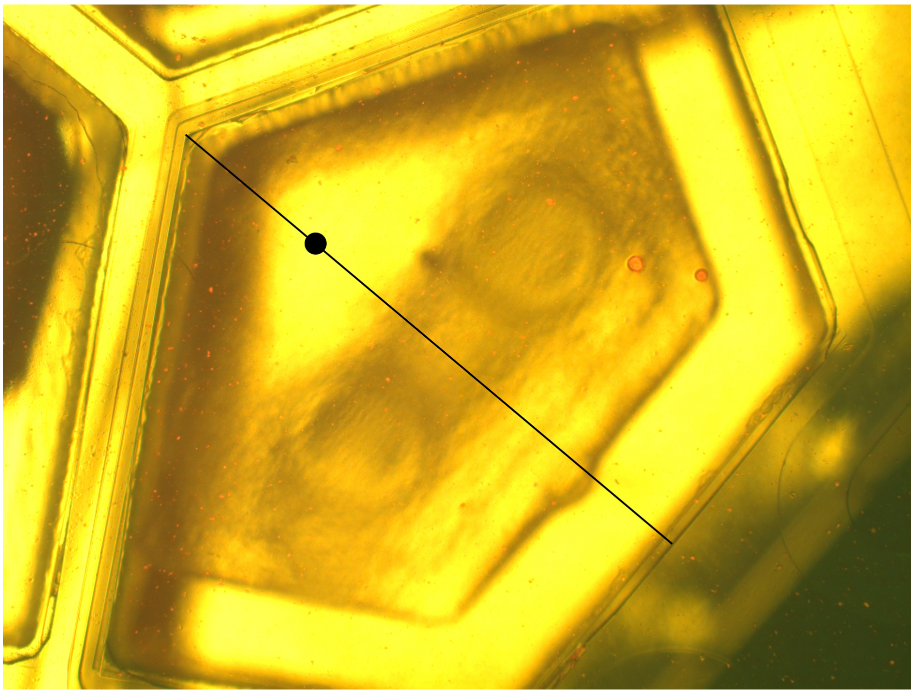

Figure 3.16. *The overlayed line for the oxygen profile at the end of the measurement along the cell compartment and the point where oxygen data is extracted over time to find the system's time constant.*

surements run at 21 ℃, the simulations were rerun with adjusted parameters. The decrease in temperature causes the oxygen concentrations in the three domains air, liquid, and PDMS to increase at equilibrium. On the contrary, the diffusion coefficients decrease. No reliable value for the diffusion coefficient in PDMS at room temperature was found in the literature, so it was kept at the previously used value for a temperature of 35 ℃. An overview of the parameters is given in Table 3.9.

The position and size of the submerged structure were also adjusted in the rerun simulations. These were measured from Chip 3 and set to a distance of 640 µm from the bottom of the cell compartment, 300 µm away from the center, and with a width of 3700 µm.

Table 3.9. *Comparison of simulation parameters used at 37 ℃ and 21 ℃. Sources are given for the values at 21 ℃.*

Parameter	**37 ℃**	**21 ℃**	**Source**
$c_{\mathrm{g\_eq}}$	$7.47\ [\frac{\mathrm{mol}}{\mathrm{m}^3}]$	$7.87\ [\frac{\mathrm{mol}}{\mathrm{m}^3}]$	calculated
$c_{\mathrm{l\_eq}}$	$0.20\ [\frac{\mathrm{mol}}{\mathrm{m}^3}]$	$0.27\ [\frac{\mathrm{mol}}{\mathrm{m}^3}]$	calculated
$c_{\mathrm{p\_eq}}$	$1.35\ [\frac{\mathrm{mol}}{\mathrm{m}^3}]$	$1.42\ [\frac{\mathrm{mol}}{\mathrm{m}^3}]$	calculated
D_{Air}	$2.1 \cdot 10^{-5}\ [\frac{\mathrm{m}^2}{\mathrm{s}}]$	$2.0 \cdot 10^{-5}\ [\frac{\mathrm{m}^2}{\mathrm{s}}]$	[105]
D_{Liquid}	$2.69 \cdot 10^{-9}\ [\frac{\mathrm{m}^2}{\mathrm{s}}]$	$2.0 \cdot 10^{-9}\ [\frac{\mathrm{m}^2}{\mathrm{s}}]$	calculated using ref. [106]
D_{PDMS}	$3.4 \cdot 10^{-9}\ [\frac{\mathrm{m}^2}{\mathrm{s}}]$	$3.4 \cdot 10^{-9}\ [\frac{\mathrm{m}^2}{\mathrm{s}}]$	[28]

4. RESULTS AND DISCUSSION

In this chapter, the conceived designs are introduced and evaluated using a weighted evaluation, with the best two being compared with each other using simulations. Then the chosen concept is presented with its own simulation results. This is followed by the results of the manufacturability tests for membranes with through-holes. Subsequently, the results of mold production are introduced, ranging from mask production over the SU-8 procedures to 3D-printed parts and mold assembly. Then the production, alignment, and bonding of chips, their leakage test, and oxygen measurements close out this chapter.

4.1 Design selection and simulation results

Based on the current state-of-the-art neuronal cell culture chip introduced in Section 2.8 and its associated limitations and requirements highlighted in Section 3.1, three potential designs were conceptualized.

4.1.1 Concept 1: Partitioner with scavenging channels

The first concept featured a divider structure made of a material that was not permeable to oxygen. The shape of the structure featured three arms at a distance of 120° from each other, separating the three cell compartments (see Figure 4.1b). The structure would have been placed into the mold, where PDMS gets cast around it so it would have been fully embedded within the chip. To maximize the oxygen scavenging area, scavenging channels were incorporated into the walls of the structure, spanning its entire height. These scavenging channels needed to be covered by a thin sheet of PDMS, which would have been bonded to the structure, to keep the scavenging channels open during the PDMS casting (see Figure 4.1a). Schematics of this concept are shown in Figure 4.1.

Benefits: The most significant benefit was the proper compartmentalization that would have been achievable with this embedded non-oxygen permeable structure. Additionally, the large surface area that could be used for scavenging channels could have helped improve the speed of the system.

Drawbacks: However, the drawbacks outweighed the benefits, as there were many of

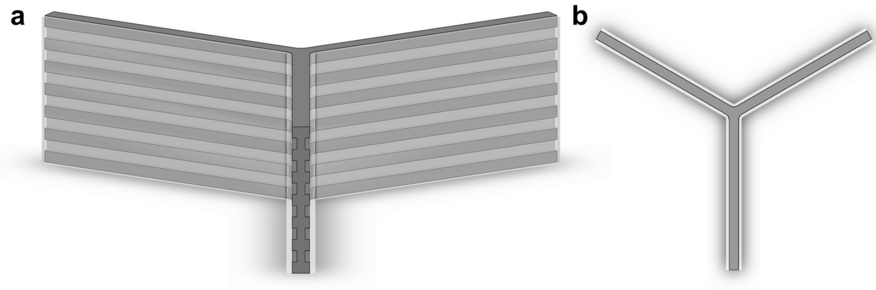

Figure 4.1. *The embedded partitioner structure.* ***a:*** *Angled view of the structure, showing the side profile of a wall with embedded scavenging channels and PDMS film on both sides.* ***b:*** *Top view of the structure highlighting the 120° degree arrangement of the structure. The three cell compartments are located between each set of arms.*

them. First, the embedded structure was rigid within the flexible PDMS, causing difficulties during demolding. Additionally, the structure needed to be thinner than 400 µm while being several millimeters tall. A structure of this aspect ratio would have been very prone to breaking. The scavenging channels within the system needed to be covered with a thin sheet of PDMS to prevent them from getting filled while casting. However, this was difficult to achieve in a reliable manner due to the 120° arrangement of the walls, causing a kink in the sidewall. Another difficulty was the connection of tubings to the scavenging channels. Furthermore, oxygen scavenging would have only occurred at the center wall, so there would be a large gradient along the entire cell compartment, with oxygen levels rising with increased distance.

4.1.2 Concept 2: Scavenging channels around the cell compartment

The second concept featured a scavenging channel that was routed around the cell compartment above the microtunnels that connect them. This was achieved by a two-layered chip design. To bring the scavenging channels closer to the cell compartment, the compartment size in the first layer was reduced to the area where the microtunnels and MEA electrodes were located. This reduced the distance of the center of the cell area in every direction to the scavenging channels, which aimed to reduce the formed oxygen gradient. To achieve this, the scavenging channels needed to be routed through both layers (see Figure 4.2). The first layer (Figure 4.2a) contained the microtunnels, the reduced cell compartment with the openings, and the scavenging channels surrounding it on three sides (in blue) with their vias to connect them to the scavenging channels of the second layer. Contained in the second layer (Figure 4.2b) were the scavenging channels routed above the microtunnels (in orange) and the large cell compartment as well as the medium chamber formed by a 3D-printed insert (not shown here). The scavenging channel routing is shown in its entirety in a bottom view in Figure 4.2c. Both of these layers had to be carefully aligned and bonded to ensure the scavenging channels were sealed and

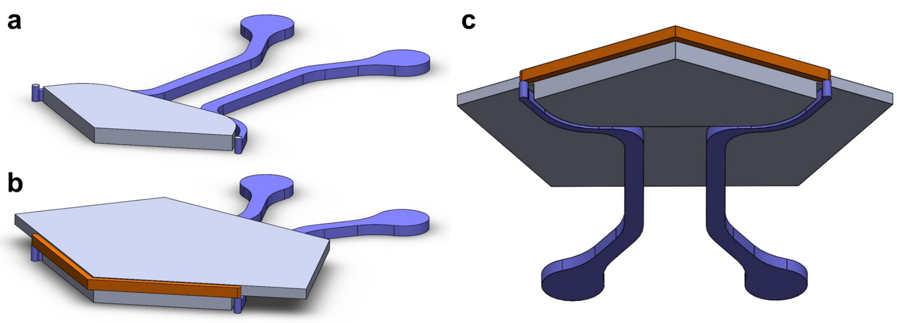

Figure 4.2. *The two-layered design features scavenging channels that are routed around the cell compartment. Here shown in a single cell compartment.* ***a:*** *First layer containing the cell area on the MEA plate, the microtunnels, and the scavenging channel (blue) on three sides.* ***b:*** *Lower part of the second layer stacked on the first layer, featuring the scavenging channels routed above the microtunnels (orange). The large cell compartment is not shown.* ***c:*** *Bottom view of the two-layered scavenging channels.*

connected.

Benefits: The benefits of this design were that the cell area was reduced at the bottom towards the MEA plate and microtunnels, allowing them to be fully utilized by the cells where they could generate relevant data. At the same time, the size of the cell compartment was not significantly changed, allowing for enough cell culture medium to be contained. Furthermore, the design did not contain any moving parts inside the cell compartment or other obstructions that might have affected the cells or the imaging capabilities.

Drawbacks: Manufacturing this design was the biggest issue. For the first layer of PDMS alone, three photolithography masks were required, which were needed to make a mold containing three layers of SU-8. Additionally, the first layer, when molded, needed to have openings for the cell compartment and the scavenging channels of the second layer to be connected to. Lastly, the accurate alignment and bonding of both layers added complexity to the manufacturing procedure of each chip, with a risk of leaking scavenging channels upon misalignment.

4.1.3 Concept 3: Immersed hypoxia structure

In this concept, a thin two-layered structure would be submerged into the cell culture medium and brought into close proximity to the cells. The upper layer would be made from a stiff and oxygen-non-permeable material such as glass so the structure kept its shape. Bonded to that would have been a thin layer of PDMS containing scavenging channels for the scavenger to flow through (see Figure 4.3b). The scavenging channels were connected by two rigid tubings for inlets and outlets, which served at the same time as the structure used to hold it in place and control the distance to the cells (see Figure 4.3a).

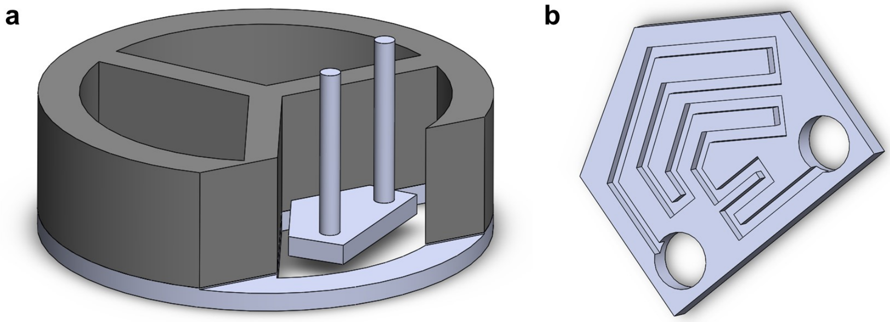

Figure 4.3. *Immersed hypoxia structure.* ***a:*** *Simplified cell compartments with the submerged structure in place.* ***b:*** *Bottom of the submerged structure featuring the scavenging channels, here engraved into the glass, which gets covered by a thin sheet of PDMS.*

Benefits: The oxygen gradient in this design was expected to be very small, especially under the structure, and, depending on the distance to the cells, likely even non-existent. However, next to the structure, a gradient would have formed as oxygen can readily diffuse there. As no oxygen could diffuse from the top due to the glass plate and the large surface area of the scavenging channels paired with the thin PDMS membrane and the low distance to the cells, the system was expected to be very fast. Additionally, due to the directed scavenging, the effect on neighboring cell compartments was considered minimal.

Drawbacks: The most significant expected drawback was that the large structure would hinder the diffusion of nutrients to the cells. Depending on the nutritional needs of the cells, long-duration experiments would not be possible. Additionally, the application and removal of the structure displaced a lot of medium due to its size, which might have caused shear stresses that were a risk to the cells and caused their detachment. Moreover, the cells would usually be imaged from below the MEA plate. However, the illumination came from the top, so the structure was in the light path, casting shadows and reflections that compromised imaging quality. Lastly, the repeatable and reliable positioning of the structure may have posed a problem as well, but at this point, it was unclear to what extent these deviations would have affected the system.

4.1.4 Weighted evaluation of concepts

The three concepts were evaluated against the following four criteria: fabrication complexity, gradient of O_2, speed of O_2 change, and potential acceptability by the end-users. The evaluation and estimates for each of the criteria for the three designs are shown in Table 4.1. As these values were primarily assumptions based on experience and planned-ahead protocols, these evaluations might deviate from the truth once the approaches were actively pursued.

Concept 1 achieved only a low amount of points as it was considered hard to manufacture,

Table 4.1. *The result table for the weighted evaluation.*

	Concept 1	**Concept 2**	**Concept 3**
Fabrication	1	4	3
Gradient	2	4	5
Speed	4	3	5
Possible Acceptance	3	5	1
Total	**10**	**16**	**14**

contained many difficulties, and featured a steep gradient as oxygen can only be scavenged from the center. The speed was evaluated higher due to the large available surface area where oxygen scavenging can occur, and the possible acceptance was evaluated in the middle range as the design did not affect the cell area, but the partitioner obstructed the lightpath to the microtunnels.

Concept 2 scored the highest points in total. Its fabrication was rated as high, even though difficulties in the production of the mold were present. However, once the mold was done, many layers could be replicated, so this problem was not seen as too crucial in the rating. In terms of gradient, high points were achieved as well due to the scavenging channels being moved closer to the cell area, reducing the distance. Due to the limited scavenging channel size and area for oxygen scavenging, the speed of this approach was rated as the lowest. However, the possible acceptance by the cell researchers was seen as best, as the changes to the cell area were minimal. The reduced cell area might have even been beneficial, as the cells were confined to the area of interest.

Concept 3 scored the second-highest points. The fabrication of the immersed structure was seen as difficult due to the very limited available space, the fragility of the thin glass sheet, and the reliable positioning. However, in terms of gradient and speed, this approach scored the maximum points, as the scavenging area was large and distributed parallel to the cell area. Nonetheless, the structure was evaluated with the lowest points in the possible acceptance as the researchers needed to submerge the structure and bring it close to the cells, which posed a risk to the culture and caused distortions in the lightpath.

Based on these results, the two most promising Concepts, 2 and 3, were chosen to be simulated.

4.1.5 Simulation results

In all models, the outermost domains represented the ambient air, where the boundaries towards the liquid and PDMS contained flux nodes, while the outer boundaries were kept constant at ambient air concentrations. The areas shown with the colored oxygen gradient were the domains filled with culture medium, while the surrounding areas that were not ambient air represented PDMS. Some models featured scavenging channels embedded in the PDMS, which were represented by an air domain as well. The numerical results were prone to errors due to several unknown factors or some known with only limited accuracy. However, for the purpose of comparing the values between the simulation models, they were reported with higher accuracy since they were all built using the same parameters.

The time constant for Concept 2 was found to be 574 s. The steady state was estimated to be reached after five times the time constant, so after 2870 s. At this time point, the plots for comparison shown in Figure 4.4 were generated. The scavenging channel surrounding the left cell compartment was fed with 9.5 % oxygen to avoid too large an effect on the scavenged cell compartment while keeping the oxygen levels reasonably high.

For Concept 3, the time constant was determined as 24 s, with the steady state being

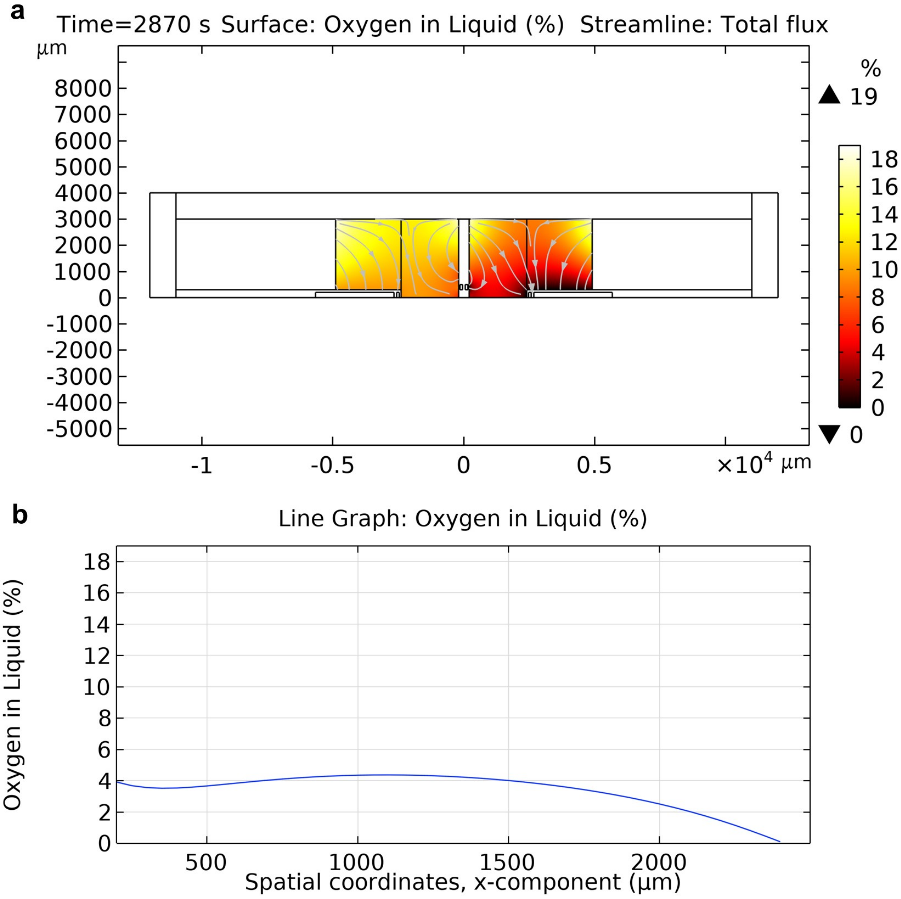

Figure 4.4. *Simulation results of Concept 2 featuring scavenging channels routed around the cell compartment.* ***a:*** *Gradient image of the oxygen concentration in cell culture medium. The arrows indicate the oxygen flux.* ***b:*** *1D-plot of the oxygen concentration at the bottom of the scavenged cell compartment from the center wall to the right wall.*

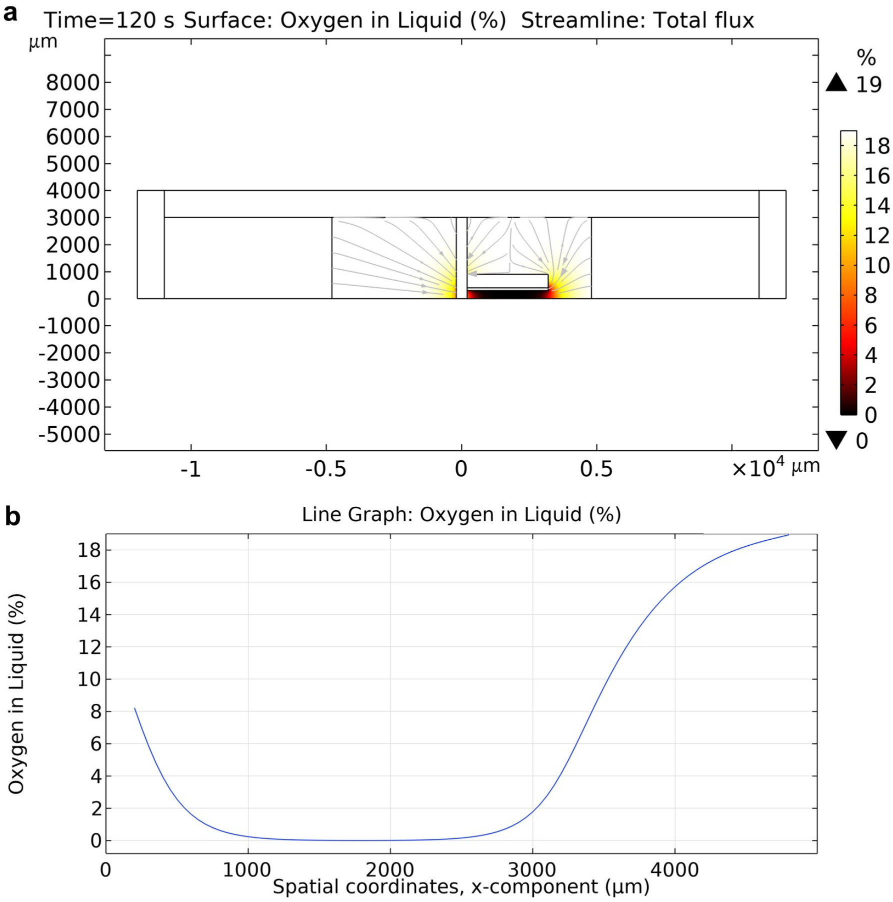

Figure 4.5. *Simulation results of immersed hypoxia structure Concept 3.* ***a:*** *Gradient image of the oxygen concentration in cell culture medium. The arrows indicate the oxygen flux.* ***b:*** *1D-plot of the oxygen concentration at the bottom of the scavenged cell compartment from the center wall to the right wall.*

reached after 120 s. This time point was used to plot the graphs in Figure 4.5. Due to the fast scavenging speed towards the bottom of the cell compartment, the rest of the cell compartment as well as the neighboring one, are still at a higher oxygen concentration. This indicated that the scavenging occurred here in a much more directed fashion. When the scavenging was applied for longer durations of time, the oxygen concentration in other areas of the cell compartment reduced as well—however, not as much as in Concept 2.

These simulation results might deviate from the truth due to the estimated values that were used when building the models. However, since the models in the comparison were all based on the same assumptions and parameters, the models were considered comparable with each other.

4.1.6 Chosen concept

Based on the simulations and simulation experiments with varying conditions, a simplified and modified version of Concept 2 was chosen. Several simplifications and changes were made to this design to test the idea in general as well as the newly required manufacturing steps. This platform can be seen as a pathfinder to evaluate the design, new ideas, and simulations, learn from the mistakes, and build a more dedicated version in a later design iteration. First, a general design explanation with a highlight of the alterations of Concept 2, including their reasoning, is given, followed by a more in-depth description containing dimensions. Then, the simulation results for this design and the expected difficulties and downsides will be presented.

Most notably, the scavenging channel was now routed only through a single layer of PDMS, compared to both layers. This removed the need for the vias connecting the scavenging channels between both layers. The design, however, was still using two layers that required to be aligned and bonded. The lower layer containing the microtunnels is referred to as the microtunnel layer. It was manufactured using the most suitable manufacturing technique to produce PDMS layers with openings found through the experiments in Section 4.2. The second layer containing the scavenging channel is referred to as the scavenging channel layer and made use of a micro-macro mold. It featured 3D-printed parts aligned and glued onto the SU-8 layer, also described as an “insert.” With this technique, it was possible to build molds that contain features of larger sizes than were possible with SU-8 and with finer features than could be produced by 3D printing alone. The SU-8 structure was used to form the scavenging channel, while the insert formed the cell compartment above. Due to the scavenging channel routing in a single layer, the cell compartment had to be set back to its original size, which caused the scavenging channels to be farther away from the cell compartment, resulting in a steeper oxygen gradient throughout the cell compartment. This was counteracted by an additional passive submerged oxygen-blocking structure into the medium above the cell compartment, very much like the one described in Concept 3, but without any scavenging channels. This prevented direct diffusion of oxygen from above and limited the vertical effect of the scavenger, focusing it below the structure. Additionally, there was only one scavenging channel routed around a single cell compartment instead of a separate scavenging channel per cell compartment. This scavenging channel was moved more towards the center of the wall separating the cell compartments, allowing for a thicker scavenging channel wall to improve the conditions for the scavenging channels to be properly sealed during the bonding procedure.

The microtunnel layer featured the openings for the cell compartment as well as the microtunnels connecting them. In Figure 4.6, this can be seen as the gray structure up until the orange scavenging channel. The layer was designed to be 200 µm thick. The scavenging channel layer contained the scavenging channel as well as the insert to form the larger cell compartment. The scavenging channel was 500 µm wide, ranging from the inlet and outlet towards the narrow center part above the microtunnels. Along this range, the wall between the scavenging channel and the cell compartment was 250 µm

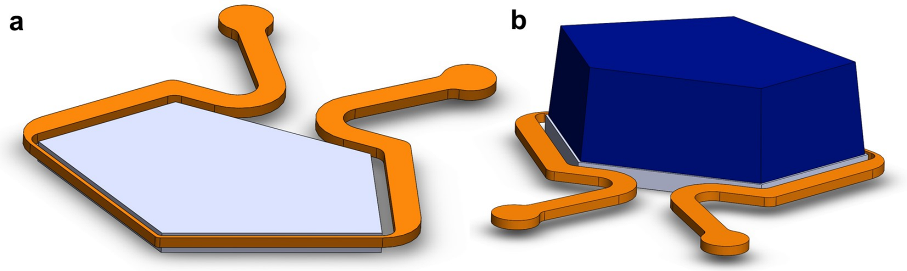

__Figure 4.6.__ Schematic of the simplified approach containing a scavenging channel (orange) routed around the cell compartment (grey) in a single layer. The microtunnels connecting the cell compartments are located under the scavenging channel where it is the narrowest. __a:__ Angled view of the cell compartment and the scavenging channel. The 200 µm gap towards the bottom is visible here. The 3D-printed insert is not shown here. __b:__ Angled view showing the structure from the inlet and outlet side and the 3D-printed insert applied (blue).

wide. Keeping the scavenging channels wide for as long as possible reduces the pressure drop. Above the microtunnels, the scavenging channel had a width of 80 µm, a wall thickness of 100 µm towards the scavenged cell compartment, and 220 µm towards the other two cell compartments. The scavenging channel was located 200 µm above the bottom of the chip because the microtunnel layer was designed with a thickness of 200 µm.

The submerged oxygen-blocking structures were 3D-printed from a transparent resin using an SLA printer. The used material was not 100 % oxygen impermeable, but it significantly impeded oxygen diffusion, which was considered a good tradeoff for the significantly faster testing iterations of various distances, shapes, and sizes of the submerged oxygen-blocking structure compared to manufacturing, for example, glass structures. The

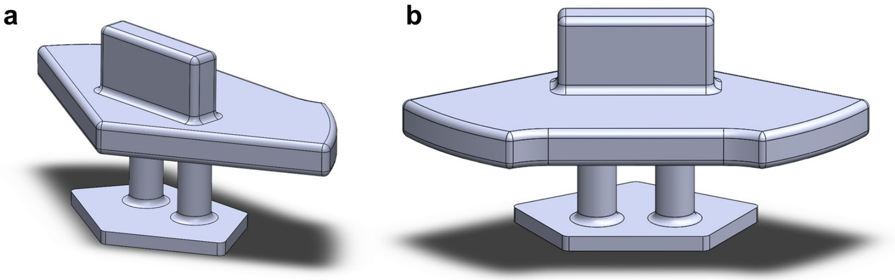

__Figure 4.7.__ 3D-printed submerged oxygen-blocking structure. The pentagonal-shaped plate at the bottom, supported by two vertical pillars, will be submerged into the cell compartment, blocking oxygen diffusion from above at close proximity to the cells. The larger upper structure closes the top of the cell compartment to prevent inward diffusion of ambient oxygen and medium evaporation. The protruding rectangular shape on top serves as a handle to grab and apply the structure using tweezers. __a:__ Angled side-view showing the edge facing inwards when applied on the chip. The inner edge angle is 120°, so three structures could be placed next to each other. __b:__ Side-view showing the outwards-facing side which features a notch to give additional space for the fluidic connectors.

submerged oxygen-blocking structure (shown in Figure 4.7) had a plate-like structure that was submerged with the same pentagonal shape as the inserts, attempting to make it as large as possible for maximum effect. The plate-like structure was supported by two vertical pillars, which connected to another larger plate-like structure that rested on top of the chip and covered the cell compartment from ambient oxygen and evaporation of the medium. The length of the vertical pillars determined the distance of the structure from the bottom of the cell compartment, together with the total chip height. Several prototypes of this structure with varying pillar lengths and sizes of the submerged pentagonal plate-like structure were fabricated for tests.

The time constant of this concept was determined as 891 s with a time to reach the steady state of 4,455 s. In Figure 4.8a it can be seen that in the right cell compartment, the scavenging occurs largely below the passive oxygen-blocking structure with some minor effect on the left cell compartment. The graph for the oxygen concentration at the bottom of the cell compartment in Figure 4.8b showed that this concept featured the most even oxygen concentration with an average value of 1 %, compared to the simulation

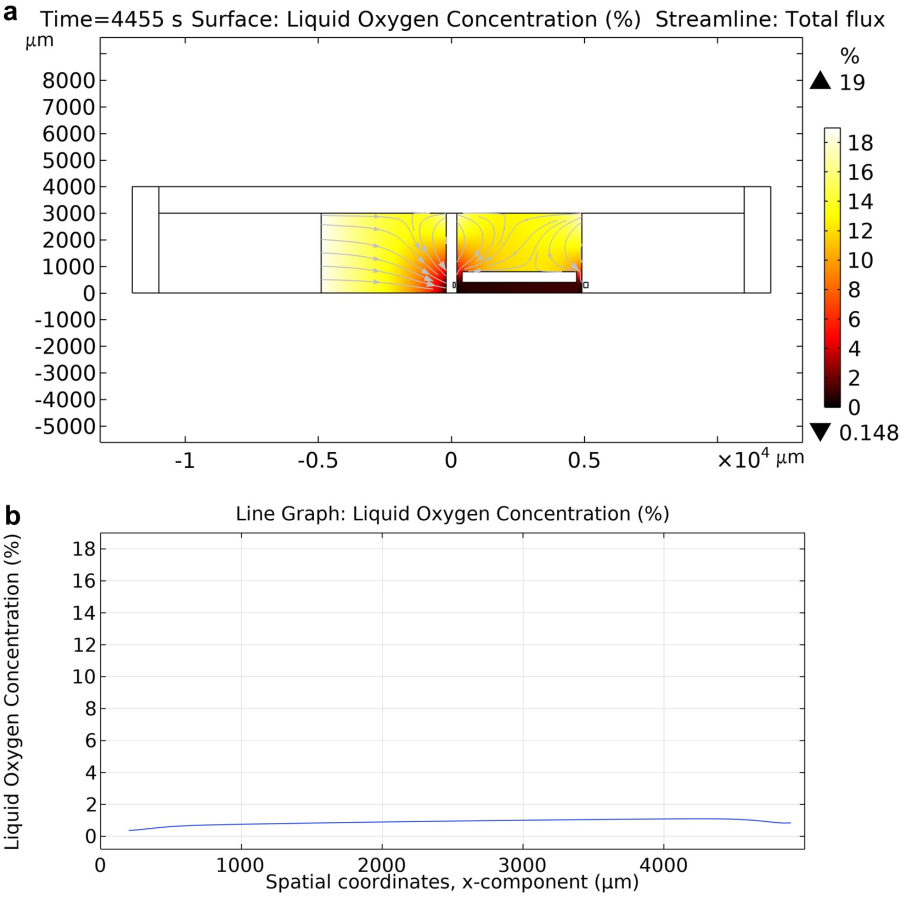

Figure 4.8. *Simulation results of the refined passive oxygen block structure concept.* ***a:*** *Gradient image of the oxygen concentration in cell culture medium. The arrows indicate the oxygen flux.* ***b:*** *1D-plot of the oxygen concentration at the bottom of the scavenged cell compartment from the center wall to the right wall.*

results of Concepts 2 and 3.

A few difficulties remained in manufacturing this chip design. The production of the 200 µm thin microtunnel layer with openings, especially ones that have clean edges and do not contain any thin flaps was difficult. These flaps could potentially fold upwards and prevent the scavenging channels contained in the scavenging channel layer from adequately sealing, causing a leaking scavenging channel which would introduce bubbles to the cell culture medium. When molding the scavenging channel layer, the PDMS was poured until above the inserts. To allow the submerged oxygen-blocking structure to pass through, this part needed to be cut away in the pentagonal shape of the insert to open it with the maximum size by hand using a scalpel. There was a risk that during this step, the chip would get damaged. Furthermore, this process was very laborious and did not scale well. Another fabrication step that posed the risk of failure was the alignment and bonding of both layers. A translational and/or rotational misalignment of the scavenging channel layer relative to the microtunnel layer could cause the scavenging channels not to be sealed properly, rendering the chip useless.

4.2 Open membrane manufacturing results

Three different techniques for fabricating PDMS membranes with openings were tested. The first used 3D-printed plates made of a material known to inhibit PDMS cross-linking. The second used glass plates coated with a crosslinking inhibitor, and the third used plain polycarbonate plates applied with pressure.

4.2.1 3D-printed inhibitor plates

The experiment using 3D-printed plates from clear resin did not work as intended. The inhibiting substance from the plates was able to prohibit the PDMS crosslinking. However, this inhibition was not limited to the interface of contact but occurred throughout the whole bulk PDMS, suggesting that the inhibiting substance was not bound to the interface but diffused readily into the PDMS. The result was a sticky, gooey PDMS mixture that was very hard to clean. No further experiments using this technique have been done.

4.2.2 Inhibitor-coated glass plates

The glass plates were successfully coated with the silane. However, there were excessive amounts of silanes in the form of horizontal lines present (see Figure 4.9a). This was thought to be caused by the rapid evaporation of the methanol from the surface of the glass plates, which flowed down after they were removed from the solution. The quality of the manufactured membranes was deemed acceptable, even though there was still a significant amount of flaps remaining as shown in Figure 4.9b. These membranes could have been used to build the chips. However, a significant issue arose with their strong adhesion to the glass plates, which resulted in detachment from the mold, further complicating processing procedures as the thin membranes needed to be handled, cleaned, and placed on a carrier without any deformations prior to bonding.

Removing the membrane from the inhibitor plates by carefully pulling them off at different angles was unsuccessful. The membranes ripped easily, and the ripping always started from the areas where the excessive silane was deposited, and the PDMS adhered even stronger. Swelling the PDMS on the plates in IPA for 5 min before attempting the peel-off noticeably simplified the process. However, they still ripped easily in the areas of excess silane. Using a PET film tool to wedge off the membrane after IPA swelling proved to be the most reliable technique. Using the wedge, the PDMS was pushed and peeled up in close proximity to where it adheres rather than being pulled and stretched from distant points. After this technique was practiced, a nearly 100 % demold success rate was achieved. Swelling the PDMS in IPA and wetting all surfaces with it was beneficial because it prevented the PDMS from sticking to itself, the tool, and the glass plate. This was also useful as thin sheets of PDMS that stuck together were hard to separate without damaging them.

The PDMS, which was cured at room temperature, showed a lower adhesion to the glass plates and was somewhat easier to remove from the inhibitor plates. However, the adhesion was still so strong that the PDMS came out with the plate, and that submersion in IPA, together with the PET wedging tool, was the preferred way to remove it.

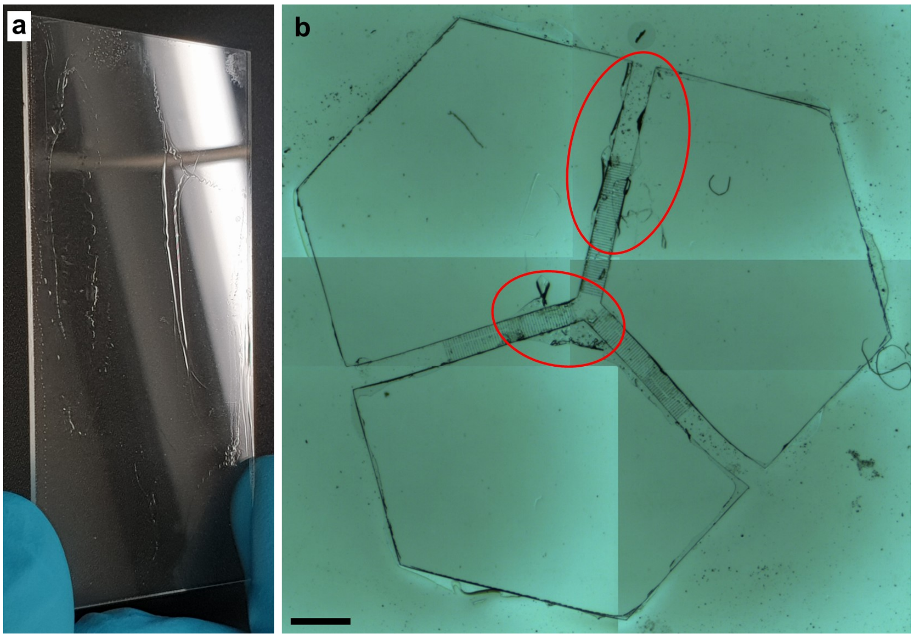

Figure 4.9. ***a:*** *Silane-coated glass plate with excessive silane residues.* ***b:*** *A closeup stitched together from multiple images showing the opening quality. Thin flaps are visible in the inner parts. Scalebar of 1,000 µm.*

4.2.3 Polycarbonate plate

The polycarbonate plates produced layers of good quality where the areas to be opened were mostly free of PDMS. A thin layer of PDMS remained on top of the SU-8 structures. When the layer was demolded, this thin layer ripped anywhere between the two edges of the mold's rim. Depending on the position this rip occurred, there were none, very minimal or larger flaps on the demolded membrane. The outcome was observed to be random, with no correlation between a position in the mold and a better or worse result. Instead, it was assumed that the way the plate was applied and the excessive PDMS squeezed out between it and the SU-8 structure affected the quality to a greater extent. Moreover, the differences between the chips in a single molding procedure might have arisen from height deviations and variations in the flatness of the mold, despite the application of a heavy weight and a flexible PDMS layer for pressure distribution. A result of the membrane molding using the polycarbonate plate is shown in Section 4.4 in Figure 4.16, where Figure 4.16a shows the remaining PDMS film on top of the SU-8 structure. Here the PDMS membrane was already removed from the mold, and only the unwanted structures remained in the mold. Figure 4.16b shows the demolded membrane with small flaps of PDMS attached that come from the thin layer that remained on the SU-8 and stayed attached. Flaps of this size were considered acceptable, but avoiding them entirely would be preferred.

However, the greatest benefit of using polycarbonate plates was the PDMS remaining within the first layer mold. This greatly simplified further processing procedures as it eliminated the need to handle and clean the first layer and reduced the need for a technique to apply it onto a carrier plate with minimal deformations for the follow-up bonding — a complicated procedure with such a thin membrane.

An additional silane treatment for the inhibition of PDMS crosslinking might have improved the quality of the openings further but is not possible on polycarbonate plates using the same procedure that was used for glass plates. Alternative procedures to permanently deposit the silane AEAPS onto these plates have not been investigated.

4.3 Mold fabrication results

The final mask design geometries for a single chip are shown in Figure 4.10. Figure 4.10a and Figure 4.10b show the geometries for the microtunnels and the cell compartment of Mold 1, respectively. Figure 4.10c shows the structure of Mold 2 containing the scavenging channel, the cell compartment structure, and the slots for aligning the 3D-printed inserts. This geometry was updated during this work, and Figure 4.10d shows the latest version. Illustrations of the four complete mask designs containing all features are shown in Appendix B.

The three ordered and the one self-fabricated mask were imaged and optically reviewed. The mask features were well reproduced with precise corners and a high resolution. In Figure 4.11, detailed shots of selected mask features are shown. The lighter areas are chrome, while the darker areas are the features that are opened and formed solid SU-8 structures during the photolithography process.

During the development of the SU-8 layers, the inspections of the development quality showed some undeveloped areas in Layer 1 of Mold 1, as shown in Figure 4.12a. Additional development cycles reduced these residues, as shown in Figure 4.12b. A similar problem was observed during the development of the 200 µm thick SU-8 layer of Mold 2. The narrow gap between the base for the 3D-printed insert and the scavenging channel was hard for the developer to get to, even though the developer was agitated using the vortex mixer. Several redevelopment steps of 3 min as well as a final development step in fresh developer, were required to achieve a clean result.

The results of the final SU-8 layers as utilized in the molding of the chips are shown in Figure 4.13. Figure 4.13a shows the entire microtunnel structure, while Figure 4.13b shows the microtunnels with the second SU-8 layer applied to form the lower part of the cell compartment. Figure 4.13c shows a closeup of the second layer structure with scavenging

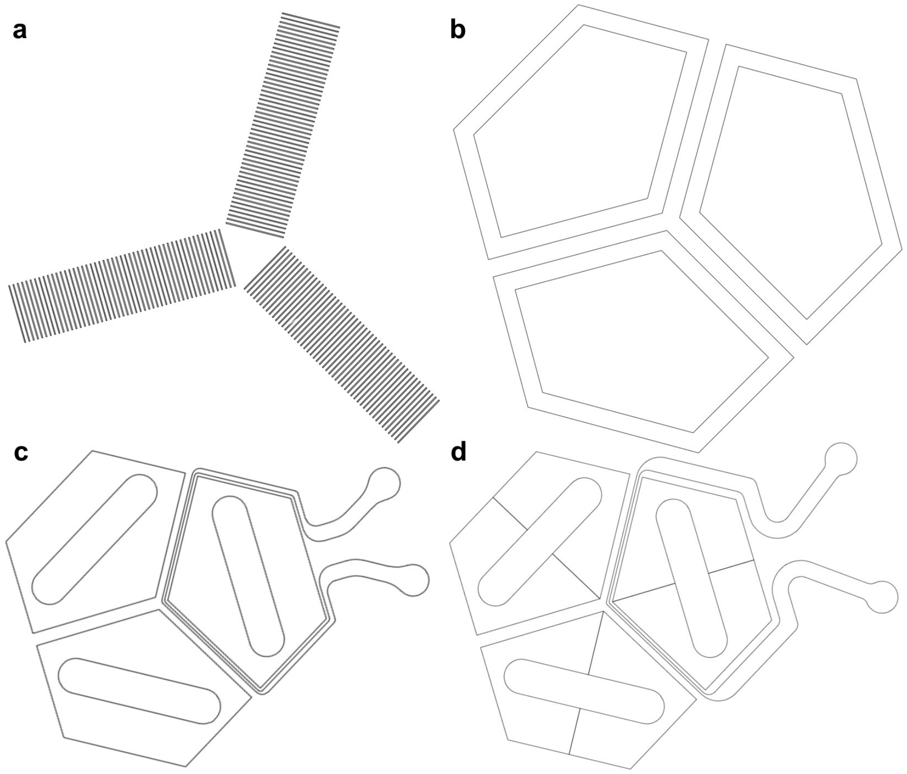

Figure 4.10. *Closeups of the chip geometries on each mask (not to scale).* ***a:*** *Microtunnel geometry for Layer 1 of Mold 1.* ***b:*** *Geometry to form the open culture area in Layer 2 SU-8 layer of Mold 1.* ***c:*** *Geometry for Mold 2 containing the scavenging channel and base with alignment slots for the 3D-printed insert.* ***d:*** *Updated version of (c).*

channels and Figure 4.13d is the updated version of it. Optically these structures looked very good. However, the measurements deviated on average by 0.35 % compared to the expected dimensions.

When comparing the measurements of the SU-8 structures and the masks, it was observed that they both deviated by 0.35 % on average compared to the expected results. This result suggested that the SU-8 structures were well reproduced from the mask, and there were no problems during UV exposure. Additionally, the error itself was very small due to the measured length of over 4000 µm and the minimal changes in the range of a few tenths of micrometers. These deviations were expected to arise either from an optical effect of the microscope's lenses or due to the calibration of the pixel size in the software. Furthermore, minimal changes in the manually aligned measurement tool between pixels resulted quickly in changes of 1 µm to 2 µm. Assuming that the overall error stemmed

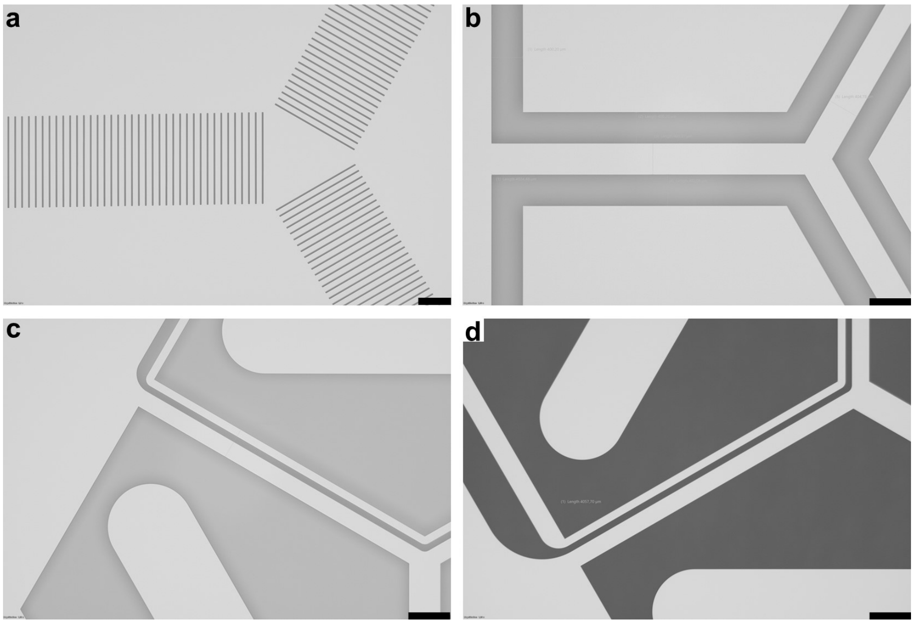

Figure 4.11. *Images of chip features on the masks. Scalebar of 200 µm for (a) and 500 µm for (b), (c), and (d).* ***a:*** *Section of microtunnels.* ***b:*** *Section of cell culture area.* ***c:*** *Section of the scavenging channel.* ***d:*** *Updated version of (c).*

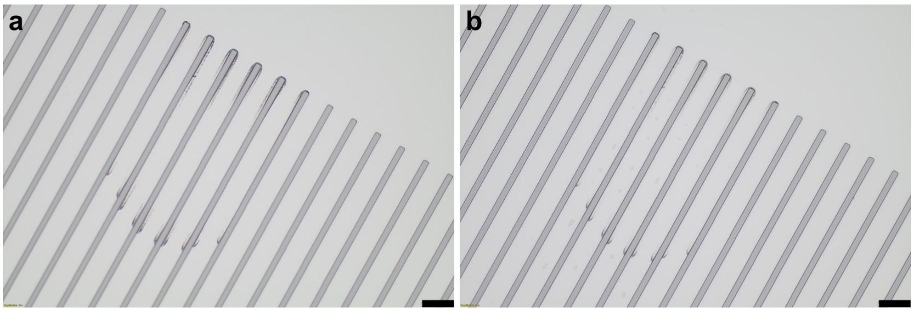

Figure 4.12. *3.5 µm SU-8 layer of the microtunnels during development. Scalebar of 50 µm.* ***a:*** *After 1 min of development, a large amount of residue was still visible.* ***b:*** *After an additional 15 s of development, the amount of residue was reduced.*

from a small inaccuracy within the pixel size calibration, it was assumed that all the measurements contained the same error. So as long as the measurements were all obtained with the same error, they were seen as comparable.

The measurement paths for the contact profilometer for height measurements of the layers are shown in Figure 4.14.

The profilometer height measurements of each chip can be found in Table 4.2 for the initial molds and in Table 4.3 for the second version of Mold 2. Layer 1 was, on average, 3.3 µm thick and very even, with minimal height deviation between the chips. However, the Layer 2 of Mold 1 was 214.6 µm on average, with deviations of up to 81 µm between the highest and lowest measurements. These deviations, however, were acceptable as there were at least three chips within the same range, so no new mold needed to be manufactured. Layer 1 of Mold 2 had an average thickness of 178.7 µm, with a maximum deviation of 25.2 µm.

An updated version of Mold 2 was fabricated using the same procedures but with a new and updated mask. It featured a total of ten chips with five different dimensions. Its geometry is shown in Figure 4.10d. Its average height was 208.2 µm with a maximum deviation of 92 µm from lowest to highest measurement. These structures were measured in the same way as described in Figure 4.14d. However, the numbering scheme of this mold was slightly different and is displayed in Appendix B in an overview of the entire

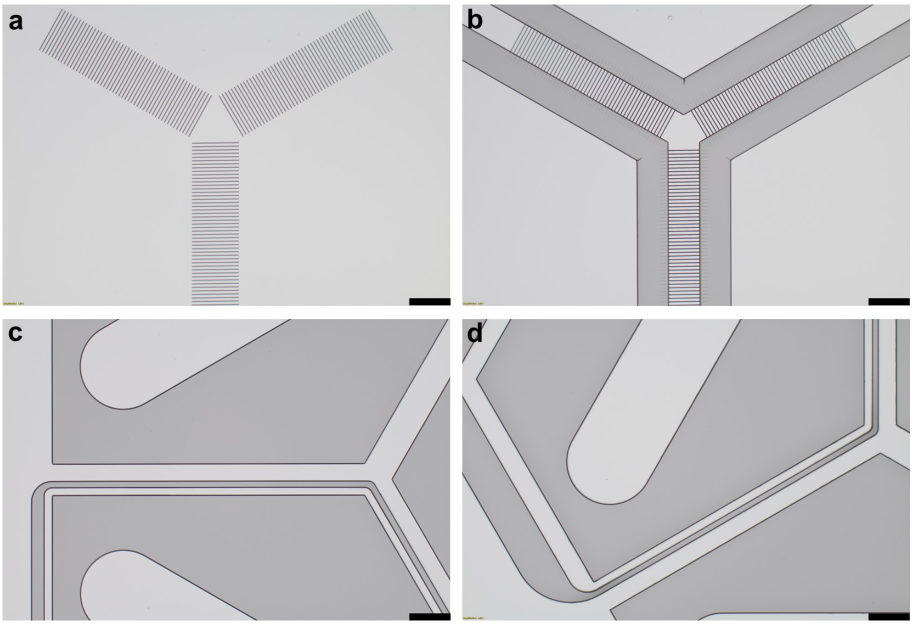

Figure 4.13. *Microscope images of SU-8 layers. Scalebar of 500 µm.* ***a:*** *Microtunnels in 3.5 µm thick Layer 1 of Mold 1.* ***b:*** *Border for cell area in the 200 µm thick SU-8 Layer 2 of Mold 1.* ***c:*** *200 µm SU-8 layer with the scavenging channels and the base for inserts in Mold 2.* ***d:*** *Updated version of Mold 2 geometry with wider scavenging channel and increased wall thickness at the sides.*

mask geometry. The height measurement results are listed in Table 4.3.

The height deviations of the 200 µm thick layers were attributed to the photoresist SU-8 3050, which was used for these layers. According to the manufacturer, it was only designed for film thicknesses up to 100 µm [107]. To achieve a more uniform film of photoresist, the SU-8 2000 series with a thickness range of 0.5 µm to 200 µm would have been better suited [108]. However, the layer variance of SU-8 3050 was accepted, as it was said to have better adhesion to silicon, leading to a longer lifetime of the molds.

The finalized molds with glued inserts and applied silane coating are depicted in Figure

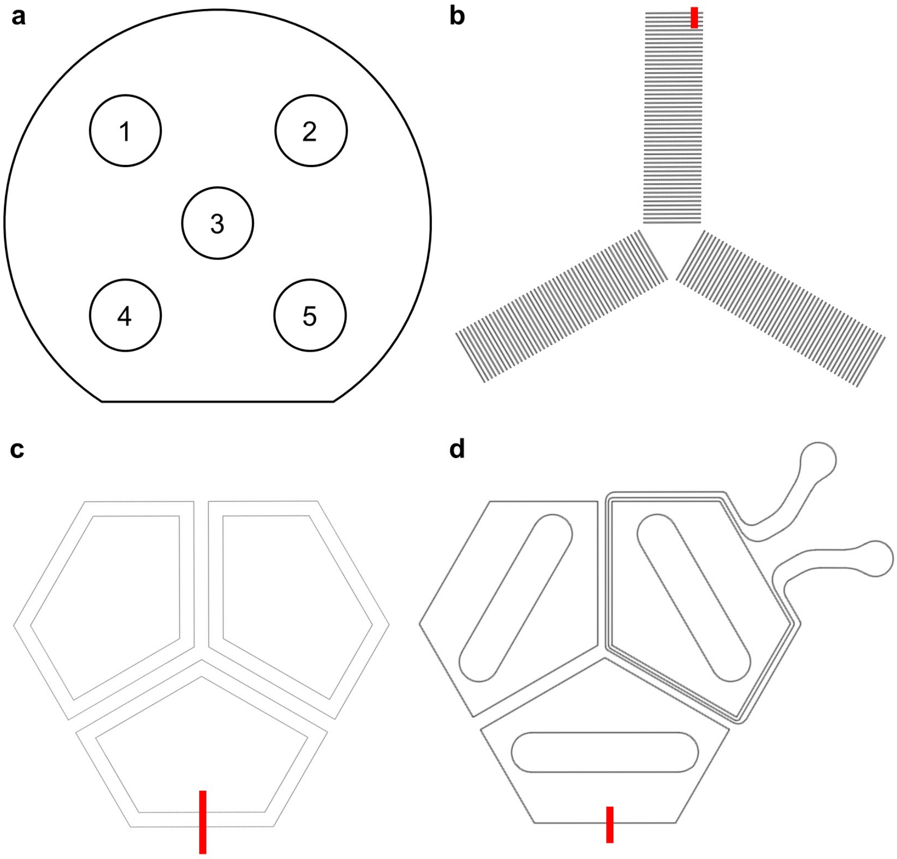

Figure 4.14. *Depiction of the chip numbering scheme and the used contact profilometer paths marked in red (not to scale).* ***a:*** *Numbering scheme of the chips on the mold with the wafer flat at the bottom.* ***b:*** *Layer 1 of Mold 1,* ***c:*** *Layer 2 of Mold 1,* ***d:*** *Mold 2*

Table 4.2. *Profilometer measurement results of the three SU-8 layers.*

Position	Mold 1 Layer 1	Mold 1 Layer 2	Mold 2 Layer 1
1	3.32 µm	189.6 µm	170.5 µm
2	3.30 µm	188.2 µm	173.0 µm
3	3.31 µm	189.5 µm	167.7 µm
4	3.30 µm	269.1 µm	189.3 µm
5	3.32 µm	236.7 µm	193.2 µm

4.15. At the time of taking the photograph, one molding cycle was done already, and the adhesion of the inserts was considered good.

Table 4.3. *Profilometer measurement results of the SU-8 height of the updated Mold 2 containing ten chips. See Appendix B for the wafer layout.*

Position	**Mold 2 Layer 1 - V2**
1	268.9 µm
2	201.0 µm
3	226.0 µm
4	245.4 µm
5	181.9 µm
6	178.8 µm
7	210.7 µm
8	191.1 µm
9	177.1 µm
10	201.0 µm

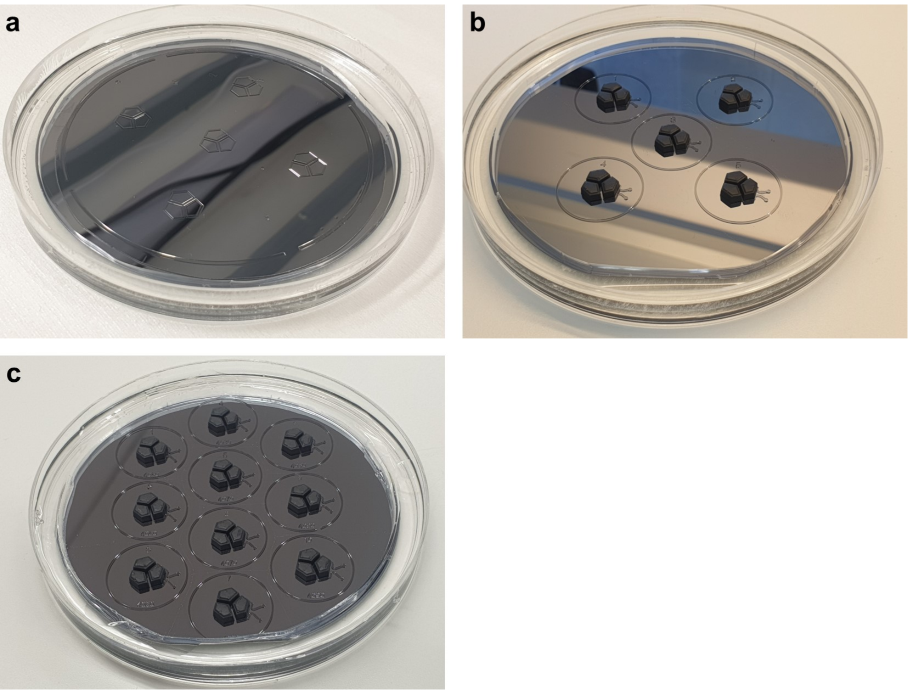

Figure 4.15. *The three finalized molds after at least one molding.* ***a:*** *Microtunnel layer mold (Mold 1) with PDMS layer still inside.* ***b:*** *Scavenging channel layer mold (Mold 2) containing five chips of the first version.* ***c:*** *Scavenging channel layer mold (Mold 2) containing ten chips of the second version with five different sizes.*

4.4 Chip fabrication results

4.4.1 Microtunnel layer

A close-up of a separately demolded microtunnel layer with minimal flaps next to the mold containing residual PDMS is shown in Figure 4.16. The upper face of the layer had an excellent surface quality from the polycarbonate plate. Careful production and handling of the plate were crucial to avoid any scratches that would transfer into the PDMS layer.

Difficulties arose due to the static charge of the PC plate, which caused many air pockets to be locked in when the plate was carefully applied. This was due to the static charge attracting the PDMS and pulling it upwards in an irregular pattern, forming air pockets that were impossible to remove. This was remedied by grounding the PC plate simply by holding it with one hand while touching the ground contact of a wall socket with the other. By following this procedure before each molding, the problem could be avoided.

Other difficulties with manufacturing the microtunnel layer were an unreliable rate of open cell compartments as well as an unpredictable amount and size of thin flaps caused by PDMS remains between the SU-8 and polycarbonate plate. If a cell compartment was not fully opened, the PDMS could always be removed by pulling it off using tweezers. However, the ripping of the PDMS was uncontrollable so larger flaps could be the result.

The best way found to demold the layer was to leave it untouched until after bonding the scavenging channel layer onto it, which was already the preferred method as it eliminated several assembly steps. The entire stack was then demolded, leaving the excess PDMS in the mold most of the time. Qualitatively, this procedure was found to produce better quality openings, as the excess PDMS seemed to tear in a more favorable manner, resulting in more minor flaps. For the best result, the chip was continuously lifted from all sides step by step.

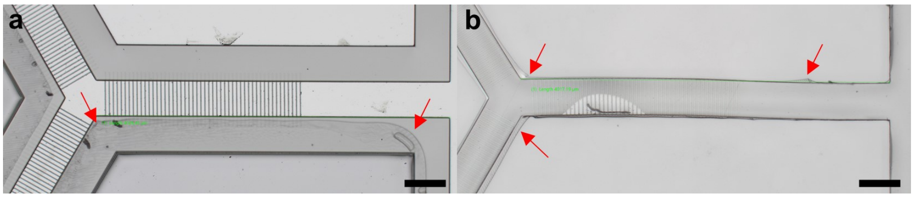

Figure 4.16. ***a:*** *Mold 1 where the layer is demolded. Only the excess PDMS remains. The thin film of PDMS on top of the SU-8 structure is clearly visible and highlighted by red arrows.* ***b:*** *Demolded first layer where minor flaps are visible and highlighted with red arrows. Scalebar of 500 µm.*

4.4.2 Scavenging channel layer - Version 1

For the scavenging channel layer, two different molds were used. For both, there were many bubbles within the center of the chip between the cell compartments, even though the PDMS was thoroughly degassed before demolding. To avoid these, several different ways of pouring the PDMS in an attempt to reduce the air pockets were tested, but none seemed to change the outcome significantly. However, some chips low in bubbles were obtained by several moldings and sorting out the best ones.

The chips demolded from the first version mold showed a significant amount of flaps, originating from PDMS that flowed into gaps between the insert and the SU-8 base substrate. An extreme example is shown in Figure 4.17a, where the darker areas are very large flaps. These flaps complicated the demolding process and caused a risk of detaching the glued insert which would result in the loss of one chip per molding. Additionally, they could have hindered the medium from freely flowing to the bottom of the cell compartment which was especially a problem for chips that were not treated to be hydrophilic. Here the flaps could have caused air pockets to build up which would be very hard to remove. Furthermore, the flaps might have hindered the submerged oxygen-blocking structure from properly being in place.

During the alignment and bonding phase using chips from this first version, it was noticed that they did not properly match together. The problem, therefore, was found to be the shrinkage of the scavenging channel layer. For the molds of both layers, a theoretical shrinkage of 1 % was added to their mask to counter the shrinkage. However, at this point, it was not considered that the PDMS of the microtunnel layer remains within the mold where it stays in a stretched state keeping the original mold size, while the scavenging channel layer was demolded and therefore allowed to shrink by the theoretical 1 %. In Figure 4.17a the real misalignment due to the shrinkage is visible along the lower edge near the scavenging channel, while Figure 4.17b shows a theoretical misalignment due

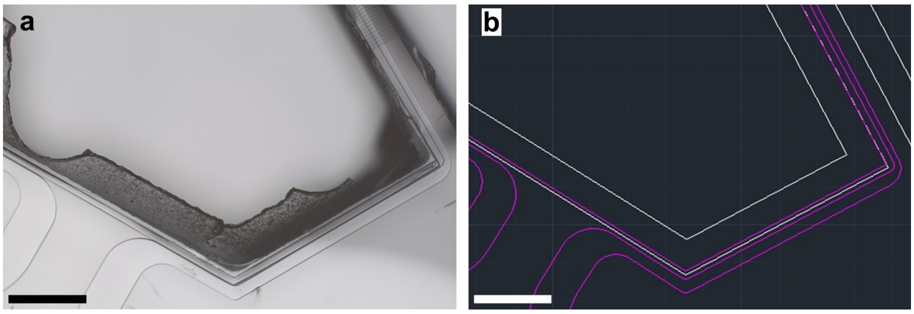

Figure 4.17. ***a:*** *Aligned and bonded chip. Large flaps of PDMS can be seen in dark gray. The misalignment of the PDMS layers due to unequal shrinkage can be seen in the bottom half along the scavenging channel.* ***b:*** *Theoretical shrinkage of the scavenging channel layer in pink compared to the unshrinking microtunnel layer in white based on a theoretical shrinkage of 1 %. Scalebar of 1,000 µm.*

to shrinkage using the previously introduced 1 %. The scavenging channel of the scavenging channel layer is shown in pink, while the microtunnel layer geometry is white. Due to the shrinkage, the wall thickness of the scavenging channel towards the cell compartment was significantly reduced, complicating the alignment, leaving little room for error, and increasing the risk of leakage.

To obtain the shrinkage of the scavenging channel layer, five chips were prepared. These were selected based on their quality from two separate moldings that were cured in the oven overnight and demolded the next day. The time they remained in the mold after curing was completed was approximately 10 h. They were then stored in a Petri dish at room temperature for several days prior to measurement. Then, the inner side length of the pentagonal cell compartment was measured optically with a microscope. The true shrinkage was then determined using the Equation 3.1 and was found to be 1.19 %.

4.4.3 Scavenging channel layer - Version 2

As mentioned before, a second version mold featuring slightly larger structures was fabricated taking into account the calculated shrinkage. A mold with a total of ten chips with two chips of five different sizes was produced. The chips were labeled by the length in micrometers of their inner sidelength of the pentagon facing towards the other cell compartments. These sizes were 4050, 4060, 4070, 4080, and 4090, with 4070 being the optimum based on the previously measured shrinkage. The two smaller sizes, 4050 and 4060, and the two larger sizes, 4080 and 4090, were added to leave room for error and increase the success rate with a single mold. The larger sizes were expected to fit as well but with a slightly larger distance of the scavenging channel to the cell compartment. Additionally, the scavenging channel along the back and sides was moved further away from the cell compartment for increased tolerance and was in these areas also widened to further reduce the pressure drop over the scavenging channel.

The second version mold for the scavenging channel layer produced chips of excellent quality. There were no or very minor flaps of PDMS that previously resulted from a little gap between the SU-8 baselayer and the glued insert. This was achieved by small changes to the design of the insert. More specifically the position of the pins and their length. Two chips are depicted in Figure 4.18. However, one insert was poorly glued with a large gap and therefore still suffered from the flap issue. Through several molding cycles, it was also observed that the quality degraded and the size and amount of flaps increased slightly.

When Mold 2 was on the same level in the oven as Mold 1 with the 7 kg weight applied, a significant deviation in layer thickness throughout the mold was observed. This was caused by the oven grating bending under the weight. Due to this, it was crucial to avoid them being on the same level, as deviations in the height of the chip can affect the submerged oxygen-blocking structure that will be resting on top of the chip. If it is tilted, the submerged part will be too, possibly affecting the blocking properties and spread of oxygen scavenging.

Of these second version chips, the ones with a sidelength of 4070 µm, 4080 µm, and 4090 µm were found to align best with the microtunnel layer, where the larger two offered some more room for alignment errors, while 4070 fitted the best. In Figure 4.19 a 4070 chip and a 4080 chip are shown bonded to the microtunnel layer. Small misalignments due to the manual procedure can be seen.

During the alignment, a few challenges were faced that complicated the procedure. The biggest one was the reflectivity of the wafer underneath the microtunnel layer which made the use of additional direct lighting impossible and made it hard to clearly recognize the structures. The second challenge was the blurry edge of the SU-8 structure which made it impossible to align it clearly to the edge of the scavenging channel layer. Additionally, the lack of a precise rotational alignment screw meant that it had to be done by hand making it less accurate. However, the translational adjustment could be done using precision screws.

The assembled chips were leak tested by gradually ramping up the pressure to the inlet from 25 mBar to 100 mBar. Misaligned chips with significant deviations started to leak

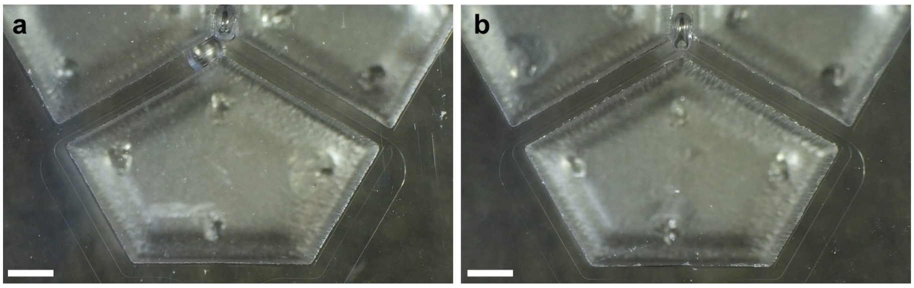

__Figure 4.18. a:__ Chip without any PDMS flaps. __b:__ Chip with very minor flaps. Scalebar of 1,000 µm.

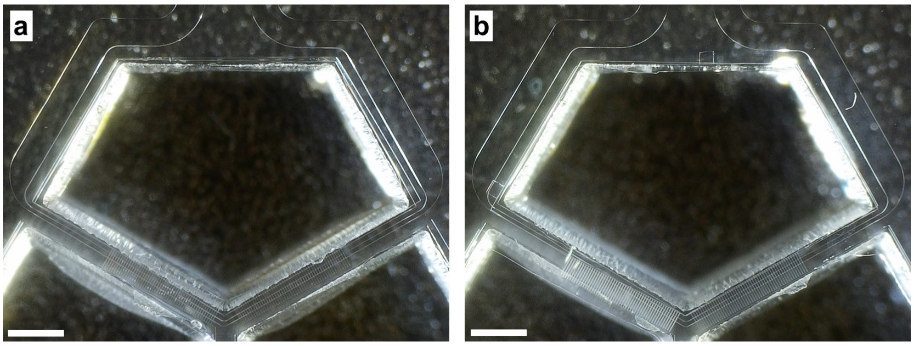

__Figure 4.19.__ Aligned chips of the reworked second version. __a:__ Chip with a sidelength of 4090 µm and a very good alignment quality. __b:__ Chip with a sidelength of 4080 µm. Slightly misaligned at the left side of the scavenging channel. Scalebar of 1,000 µm.

between 50 mBar to 70 mBar. If no bubbles were observed at 100 mBar the chip was considered as good. In one instance a chip was tested up to a pressure of 1,000 mBar without leakage. However, at such high pressures, bubbles form gradually within minutes by the air permeating through the PDMS. Therefore, as low as possible pressures applied to the scavenging channel were crucial during the measurements to avoid gradual bubble formation.

4.5 Oxygen control measurement results

During the ratiometric oxygen measurements, three different chips were measured. A chip bonded to an oxygen measurement plate within the measurement mount and the cover next to it is shown in Figure 4.20. Three chips were measured, referred to in the following section as Chip 1, Chip 2, and Chip 3. They were all based on the second version of the scavenging channel layer. The first one was of size 4060, the second one of size 4080, and the third one was of size 4070.

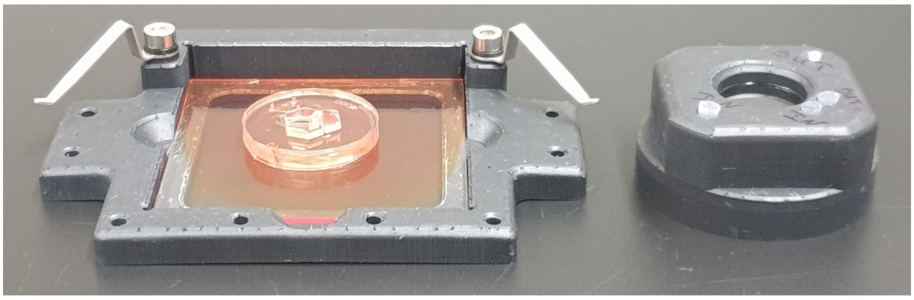

Figure 4.20. *Test Chip 2 permanently bonded to a ratiometric oxygen measurement plate within the measurement mount and the cover next to it.*

4.5.1 Chip 1

For this chip, each calibration gas was applied for 75 min, followed by a 120 min measurement. Images of the calibration time points for each oxygen concentration are shown in Figure 4.21.

During this measurement including the calibration, several bubbles gradually formed near the scavenging channel underneath the submerged oxygen-blocking structure. Additionally, delamination of the chip from the measurement layer was observed in the lower left corner of the field of view near the inlet and outlet. This was assumed to be caused by the connected metal tubings causing internal stress. Both effects can be seen in Figure 4.21.

The two used ROIs and the resulting calibration curve of the inlet ROI are shown in Figure 4.22. The calibration data was obtained using the inlet ROI which was then applied to the second ROI covering the entire chip. Since the data was only calibrated using the intensity ratios for 0 %, 5 %, and 10 % oxygen gas, the final calibration point where 19 % gas was applied deviated significantly. This indicated that oxygen content values above 10 % are not very trustworthy as they were not calibrated.

In Figure 4.23 there are oxygen maps for four time points throughout the measurement shown. The measurement started at a concentration of 19 % O_2 which was applied as the last calibration concentration to the channel. The two spots in the center which are visible in every picture as a higher concentration were an optical effect from the pillars of the submerged oxygen-blocking structure. Their position is clearly visible in Figure 4.21f and matches these two spots.

Unfortunately, this chip's measurement plate was destroyed when the measurement setup was disassembled. When the tubings to the chip were removed through the cover, the chip with the thin PDMS film and the polystyrene measurement layer were lifted off.

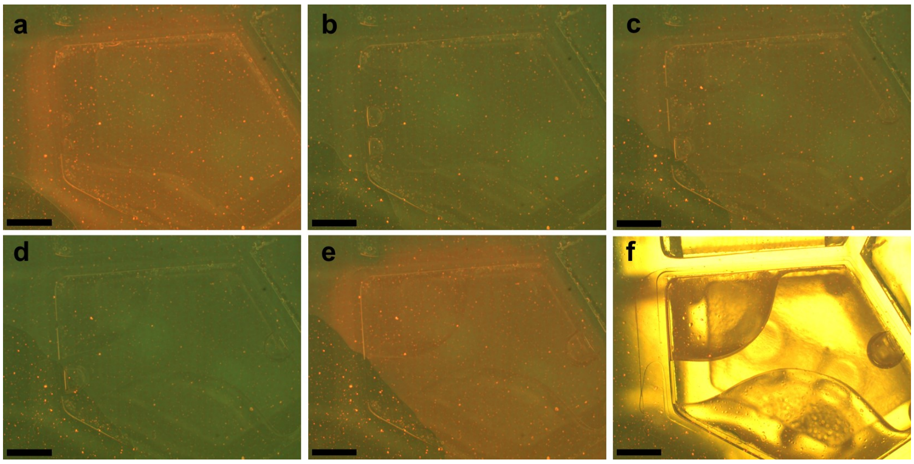

Figure 4.21. ***a-d:*** *Images of calibration time points after 75 min of each gas application for 0 %, 10 %, 5 %, and 19 % oxygen concentrations, respectively.* ***e:*** *Image during the measurement while scavenger is applied. The delamination in the lower left corner is clearly visible in comparison to (a).* ***f:*** *Brightfield image after the measurement showing significant bubble formation near the scavenging channel. Scalebar of 1,000 µm.*

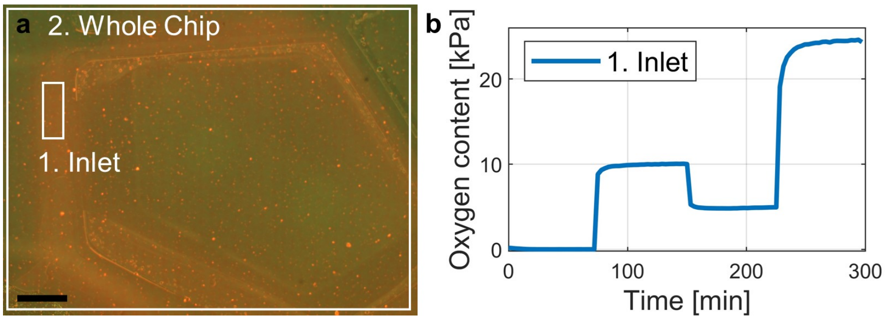

Figure 4.22. ***a:*** *The two ROIs that were defined for Chip 1. Scalebar of 1,000 µm.* ***b:*** *Oxygen content curve for the inlet ROI during the calibration sequence. Each applied concentration is clearly visible.*

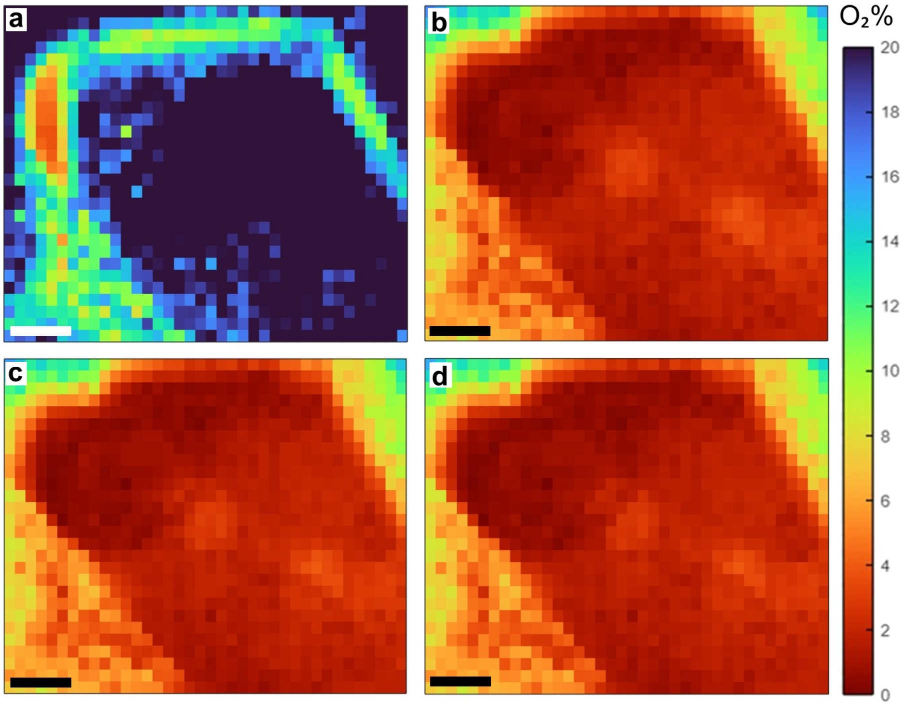

Figure 4.23. ***a-d:*** *Oxygen maps of the entire Chip 1 at 0 min, 40 min, 80 min, and 120 min, respectively. Scalebar of 1,000 µm.*

4.5.2 Chip 2

Based on the learnings from the measurement of Chip 1, this chip of type 4080 and the submerged oxygen-blocking structure were plasma treated prior to the measurement to make them more hydrophilic in an attempt to reduce bubble buildup within the cell compartment. To avoid gassing out during the experiment, the DI water was prewarmed in an incubator at 37 ℃. To enhance the gas flow through the cover, grease was applied around the bottom edge in contact with the measurement plate to better seal it. The measurement duration was again 120 min but was run prior to the calibration due to the bubble buildup and delamination that was faced during the measurement of Chip 1. The idea was to obtain clean measurement data before possible bubble buildup or other effects disturbing the measurement. Subsequently, the calibration cycle was run for 20 h overnight (5 h per calibration gas) using the automated valve system while applying the gases to the chip and cover. Images at the end of each applied calibration concentration are displayed in Figure 4.24a-d.

All the water from the scavenged and one neighboring cell compartment fully evaporated towards the end of the calibration cycle. The water level gradually decreased during the calibration. However, during the final 19 % O_2 calibration, the water under the submerged oxygen-blocking structure was seen receding as shown in Figure 4.24e. The interface of the remaining droplet wandering through the cell compartment affected the measurement data. Additionally, the sensor plate was then exposed directly to air which should not have mattered during the calibration as the same concentrations were applied throughout the entire chip and cover. However, optical changes at the interface might have still disturbed the data. A follow-up measurement would have failed in this case as the scavenging effect was no longer given due to oxygen's vastly different diffusion coefficients in air and water.

The selected ROIs and the resulting calibration curve from the inlet ROI are shown in Figure 4.25. Here, the data was also calibrated using only the 0 %, 5 %, and 10 % oxygen gases. Again the final calibration point of the 19 % gas can be seen deviating greatly indicating that any values above 10 % are not trustworthy. The deviation during the final calibration point is likely caused by the receding air-water interface shown in Figure 4.24.

Oxygen maps of the data for the entire recorded chip area are shown in Figure 4.26a-b.

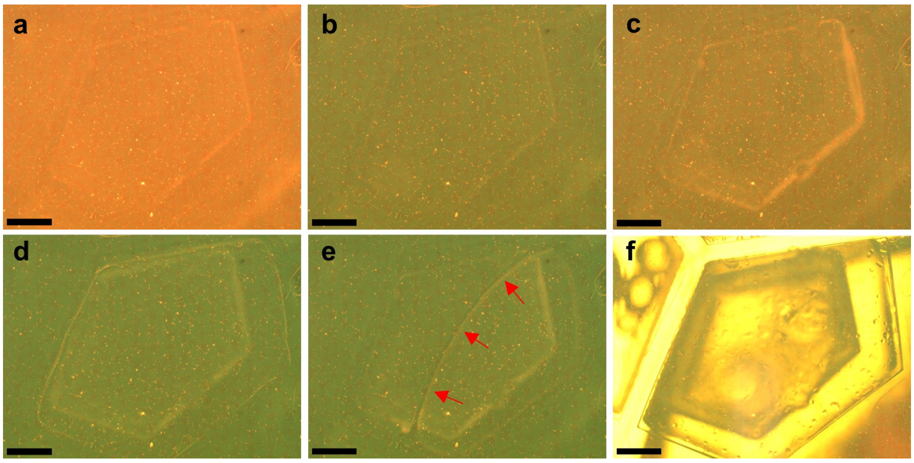

__Figure 4.24.__ Calibration images of Chip 2. __a-d:__ Images of calibration time points after 300 min of gas application for 0 %, 10 %, 5 %, and 19 % oxygen concentrations, respectively. __e:__ Image at 19 h into the measurement and calibration showing the water receding, highlighted by the arrows. __f:__ Brightfield image after the measurement showing the position of the submerged oxygen-blocking structure and the empty cell compartment with a few remaining droplets. Scalebar of 1,000 µm.

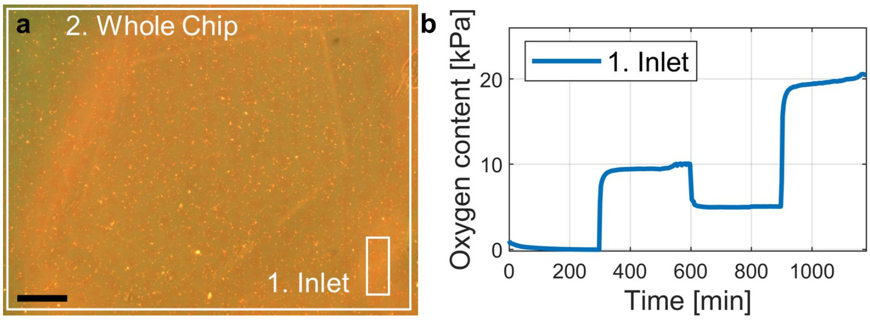

__Figure 4.25.__ __a:__ The two ROIs that were defined for Chip 2. Scalebar of 1,000 µm. __b:__ Oxygen level curve for the inlet ROI defined for the calibration sequence. Each applied concentration is clearly visible and the steady state is reached for all of them except the 19 % calibration point at the end.

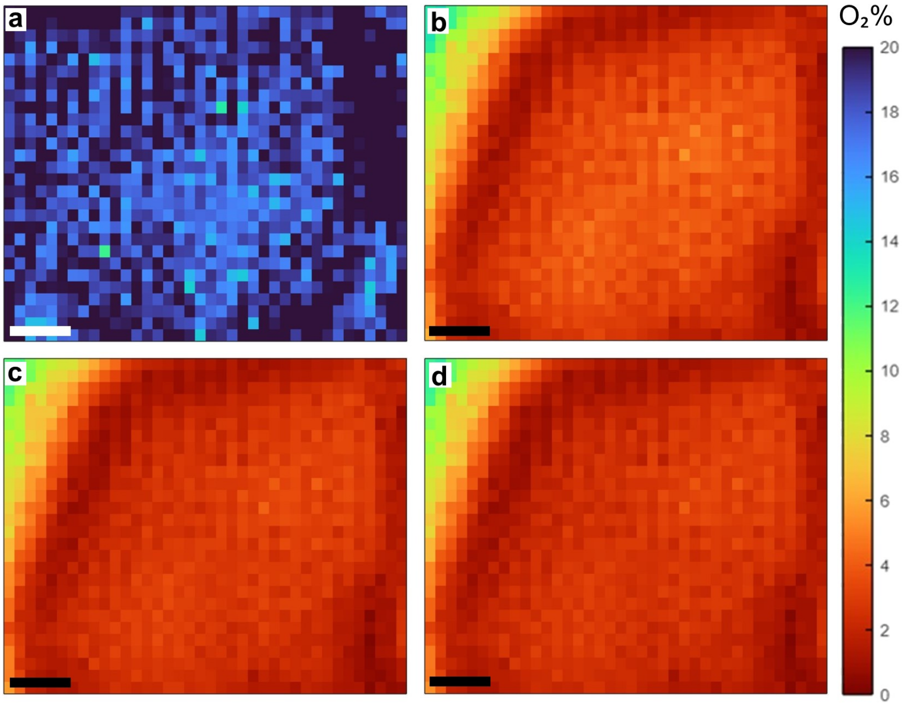

Figure 4.26. a-d: *Oxygen maps of the entire Chip 2 at 0 min, 39 min, 81 min, and 120 min, respectively. The gradient within the cell compartment is clearly visible in (b). Scalebar of 1,000 µm.*

In Figure 4.26a, the entire chip is still at 19 % oxygen which was the last calibration point. In b, a clear gradient is visible and the center reached 4-5 % oxygen concentration. In c, an average concentration of 3 % was reached, while in d after 120 min, a concentration of 2.5 % was achieved.

4.5.3 Chip 3

The third measured chip of type 4070 was set up in the same way as Chip 2. The measurement cycle was run again before the calibration cycle. The calibration was run for each oxygen concentration for 3 h compared to the 5 h that were used for Chip 2, as 3.5 h was found to be sufficient. The 19 % oxygen gas was replaced with 1 % oxygen gas as a tighter calibration in the lower concentration range was of more importance. Again, the automatic valve system was used during this calibration.

The selected ROIs and the resulting calibration curve from the inlet ROI of this chip are shown in Figure 4.28. An anomaly occurred during the 0 % oxygen gas application with a steep jump to around 19 % oxygen for roughly 50 min. This might have been caused by the remaining gas within the tubing but was surprising to occur for such a long time as the used flow rate of 5 ml/min should have cleared the estimated deadvolume much faster.

Oxygen maps for the entirety of this chip area are shown in Figure 4.29a-d. The measurement started at 19 % O_2 which was applied last to the scavenger channel and cover.

In b, a clear gradient is visible and the center reached 3-4 % oxygen concentration. In b-d, the optical error of the submerged oxygen-blocking structures pillars is visible as the yellow spots.

An image of the true zero measurement that used a liquid oxygen scavenger based on sodium sulfite (Na_2SO_3) is shown in Figure 4.30b next to the final timepoint of the conventional measurement. No gases were supplied here to the scavenging channel or the cover. A clear difference in color between the two can be seen, underlining that the conventional measurement did not reach a concentration close to 0 % oxygen. However, this data was not used in the calibration itself as for this measurement the chip needed to be disassembled, ultimately moving it in the end, making it impossible to calibrate with the gathered data as positions were shifted.

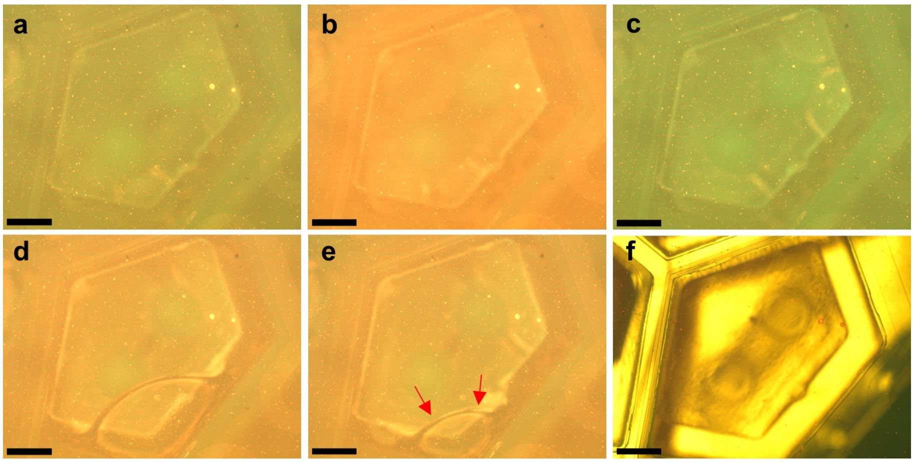

Figure 4.27. *Calibration images of Chip 3.* ***a-d:*** *Images of calibration time points after 180 min of gas application for 0 %, 10 %, 5 %, and 1 % oxygen concentrations, respectively.* ***e:*** *Image at 11 h into the measurement and calibration showing the water receding and an air pocket forming.* ***f:*** *Brightfield image after the measurement showing the position of the submerged oxygen-blocking structure. Scalebar of 1,000 µm.*

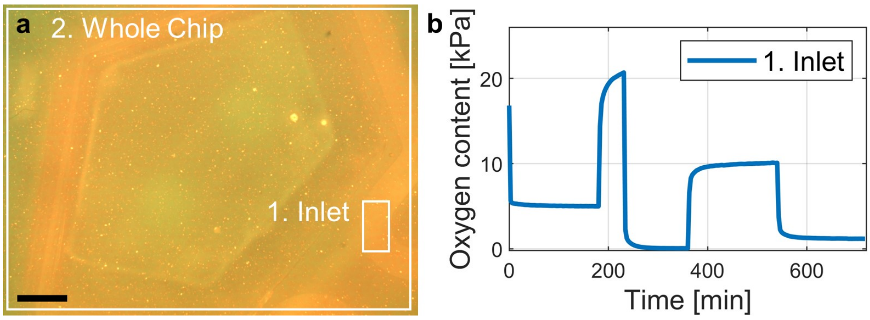

Figure 4.28. ***a:*** *The two ROIs that were defined for Chip 3. Scalebar of 1,000 µm.* ***b:*** *Oxygen level curve for the inlet ROI defined for the calibration sequence. Each applied concentration is clearly visible. At the beginning of the 0 % oxygen gas application, an anomaly is visible where the concentration shoots up to around 19 % for roughly 50 min.*

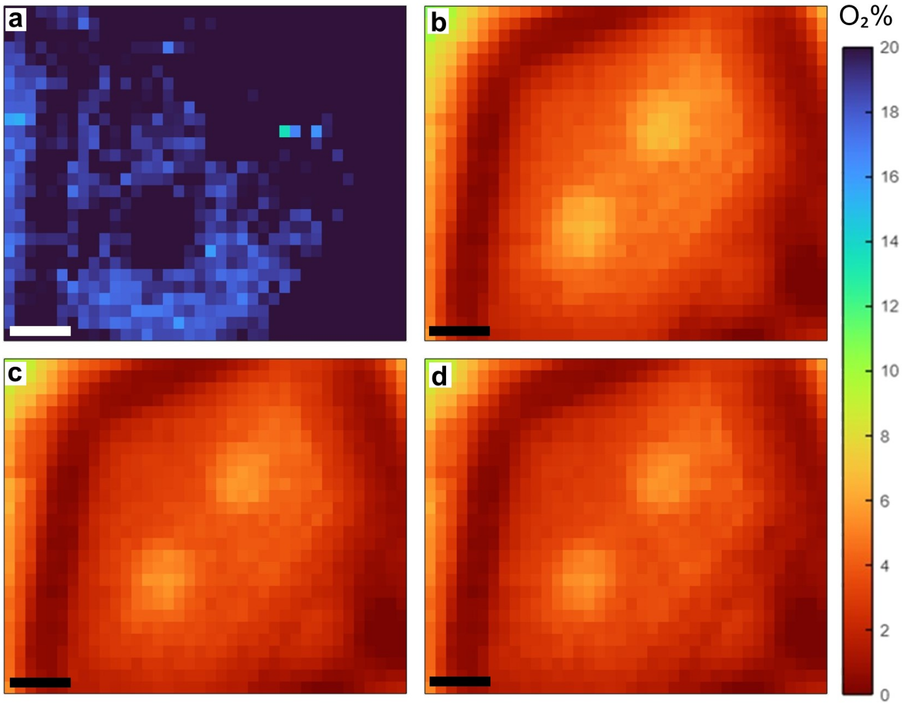

Figure 4.29. ***a-d:*** *Oxygen maps of the entire Chip 3 at 0 min, 40 min, 80 min, and 120 min, respectively.* ***b:*** *The gradient within the cell compartment, as well as the measurement error due to the pillars connected to the submerged oxygen-blocking structure, are clearly visible here. Scalebar of 1,000 µm.*

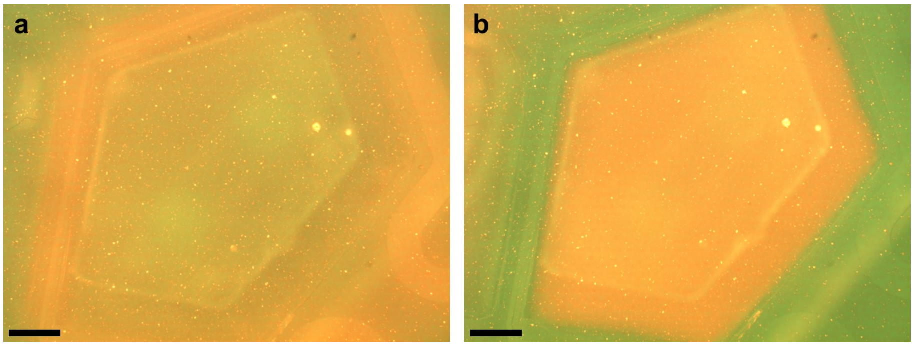

Figure 4.30. *Scalebar of 1,000 µm.* ***a:*** *Image taken at the end of the 120 min measurement.* ***b:*** *Image taken after 1 h of sodium sulfite scavenger application. The cell compartment is much more reddish than in (a).*

4.5.4 Comparison to 2D simulation results

To allow for a better comparison of the measurements to the simulations, the simulations were rerun for conditions at room temperature with the parameters stated in Table 3.9. This was necessary as the equilibrium concentrations and diffusion coefficients are temperature-dependent.

For all three chips, the concentration at the end of the measurement along a line in the center of the cell compartment was extracted to obtain an oxygen profile. In addition, to get the time constant, the concentration data over time at a spot 1.3 mm from the center was extracted as well. Both of these positions are highlighted in Figure 3.16. The comparison of the oxygen profile is displayed in Figure 4.31, while the oxygen change over time is shown in Figure 4.32. In Table 4.4 the calculated time constants for all three chips and the simulation at room temperature conditions are shown.

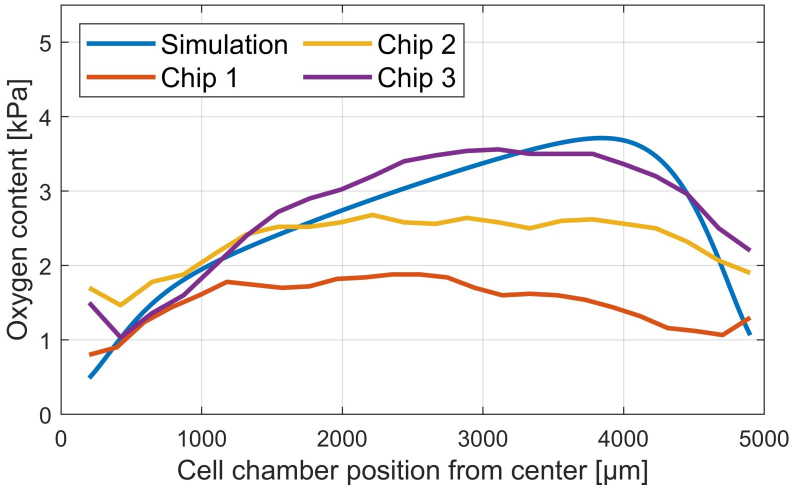

Figure 4.31. *Comparison of the smoothed oxygen concentration profile at the bottom of the cell compartment between the measurements of Chip 1-3 and the room temperature simulation.*

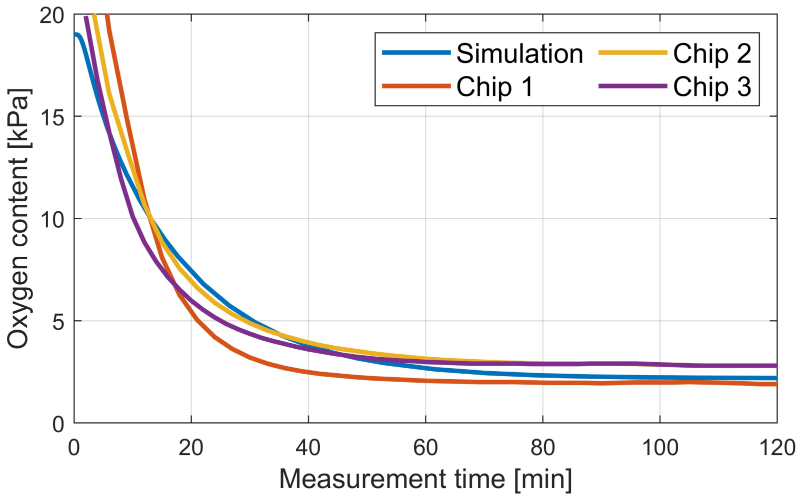

Figure 4.32. *Graphs of the oxygen content over time in the location of the measurement spot for all three measured chips and the room temperature simulation.*

Table 4.4. *Comparison of the obtained time constants from the room temperature simulation and the three measured chips.*

Simulation	**Chip 1**	**Chip 2**	**Chip 3**
1276 s	941 s	1099 s	934 s

The oxygen profile of Chip 3 and the room temperature simulation were in excellent alignment. The position of the submerged oxygen-blocking structure in the simulation was adjusted to the one in Chip 3. However, based on that the profile of Chip 1 and Chip 2 were not too far off either. The cells that are measured with this chip are usually located in the center near the microtunnels and MEA electrodes. In this range, the oxygen concentration was significantly lower compared to the more distant outer side which was beneficial for this design. In the case of the time constants, the profiles for all but the first chip were in approximate agreement. For the calculated time constants, more substantial deviations were observed, but the results were still within the same order of magnitude. These deviations might have been caused by small lateral changes in the position of the submerged oxygen-blocking structure and its distance to the oxygen-sensing plate.

There were also a few more minor differences that were not addressed in the simulations. Firstly, there was the plasma treatment used to increase a surface's hydrophilicity. Markov et al. have shown that such a treatment can reduce the diffusion coefficient for oxygen in PDMS [109]. However, this would have only affected the time constant and not the steady state conditions. Furthermore, there was the presence of CO_2 in all gases containing oxygen as presented in Table 3.7. The simulations assumed only an oxygen content, but the CO_2 present during the measurements could have impacted the O_2 diffusion. Lastly, in the simulations, the submerged oxygen-blocking structure was assumed to be a perfect oxygen blocker such as glass. The exact diffusion properties of O_2 through the 3D-printed submerged oxygen-blocking structure however were not known. It could have been that the material acted as a barrier with very low diffusion speed or might have even stored oxygen and slowly released it. Additionally, some of the many possible error sources related to the ratiometric oxygen measurements are discussed in the following chapter.

4.5.5 Error sources for oxygen measurements

There were several possible sources of error that could have affected the ratiometric oxygen measurement results. First, an accurate calibration was essential. Here, the more calibration points were used the better, but three to four was a very good compromise between the time taken to calibrate and the number of calibration points. Another error may have come from the time each calibration gas was applied. If there was not enough time to reach a steady state, the calibration would have been performed for an unknown oxygen concentration. However, this was not likely here as the area under the scavenging channel was used and the changes here occurred very fast. The way the measurement data was analyzed using the software can also greatly alter the results. The size and position as well as the features within the ROIs might have changed the outcome. Here it was assumed that the signal from the plates was homogeneous. Therefore, the obtained data from under the scavenging channel was applied to the entire chip. However, changes due to the presence of liquid, bubbles, PDMS features, the submerged oxygen-blocking structure, or other optical effects might have influenced the signal. These optical disturbances could have been reduced by spinning a thin layer of black PDMS between the chip and the measurement plate but might have also introduced other measurement errors. Nonetheless, this was not attempted during these measurements.

Furthermore, a few possible sources of error may have come from the measurement setup itself. A slow, gradual delamination of the chip bonded to the sample plate was observed for Chip 1. These changes in the arrangement likely have disturbed the light path, resulting in changes in the recorded intensity. Then, changes over time in the amount of DI water in the cell compartments due to evaporation could have reduced the diffusion distance and changed the dynamics of the system. Additionally, if too much of it evaporated as was the case at the end of the measurements for Chip 2 and 3, the measurement plate was suddenly exposed directly to the air which had a greatly larger diffusion coefficient for oxygen.

The observed bubble formation for Chip 1 could have been caused by the slight overpressure within the scavenging channel as the applied gas slowly permeates through the PDMS. In addition, bubbles might have formed by outgassing from the liquid due to temperature changes as the setup was heated up by the microscope. As a third alternative, the bubbles might have been introduced already while applying the submerged oxygen-blocking structure. Especially in the case of Chip 1 which did not undergo any hydrophilization.

The measurement plates themselves could have been a source of error too. If the dye particles were unevenly distributed or there were too many dye particles clumped together, the quality and intensity of the recorded signal might have been affected. Furthermore, these oxygen measurement plates are sensitive to temperature and humidity changes as was demonstrated by Wang and Wolfbeiss [110], affecting their signal response.

Using the automated valve system for the application of oxygen concentration gases could have caused variations in the final gas mixtures arriving at the chip if the solenoid valves were not properly sealed and leaked some of the gas. In this case, a slightly different and unknown concentration would have been used for calibrating the measurement data, causing an error. Additionally, the large design of the valves themselves and the valve block connecting them caused a rather large reservoir within. Paired with the relatively low gas flow rates of 5 ml/min, the dynamics of the setup were slowed down and the concentrations could have been slightly altered due to a mixing of the new gas and the previous gas that remained within the system. However, if only this was the case, it would have only affected the dynamics of the system, not the steady state.

4.6 Recommendations for future chip design and measurement procedure optimization

Based on the previously introduced results and experience, some recommendations for the optimization of the chip as well as the measurement procedure were collected. These are presented in this section.

The parameters that could be most easily altered in this design were the size of the submerged oxygen-blocking structure and its distance to the cells. The latter was subject to variation as the height of the chips varied from batch to batch and was hard to control. However, if this distance could be reliably reduced from the 640 µm measured in Chip 3 to below 400 µm, the oxygen levels at the center of the chip can be reduced by 0.5 % according to simulation results at room temperature. A further decrease to 300 µm cell distance and slightly below the top of the scavenging channels brings only a negligible improvement as shown in Figure 4.33a.

Bigger gains could be achieved by enlarging the structure towards the distant side from the microtunnels. If the structure was kept at a distance of 400 µm and elongated by only 200 µm, the simulations suggested that the maximum oxygen concentration would drop

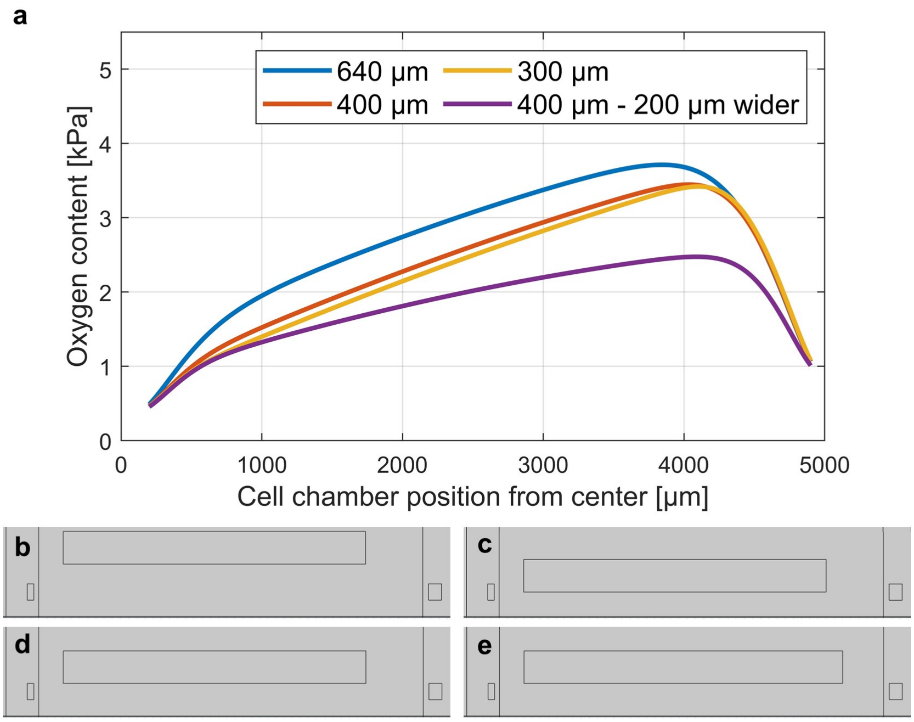

Figure 4.33. a: *Simulated oxygen profiles at room temperature conditions for different sizes and distances of the submerged oxygen-blocking structure.* ***b-e:*** *Schematics of the position and size of the submerged oxygen-blocking structure as modeled in the simulation where (b), (c), and (d) show the same size structure at cell distances of 640 µm, 300 µm, and 400 µm, respectively while (e) shows the 200 µm wider structure at a distance of 400 µm.*

by around 1.3 % to a new maximum level of 2.5 %, while the concentration towards the center stayed below 2 % up until the middle of the cell compartment as shown in Figure 4.33a. For visualization of the differences, schematics of these arrangements as they were modeled in COMSOL are shown in Figure 4.33b-e.

For the measurements, the best way to calibrate was to use only the calibration data from the ROI under the scavenging channel. The advantage of this was a much faster change in oxygen concentration compared to the rest of the chip. In addition, the oxygen levels reached in this area were much closer to the calibration gases, resulting in a more accurate calibration compared to the center of the chip, which took a very long time to reach these concentrations. However, there were drawbacks to this method of calibration, as the sensing plates themselves were not homogeneous, so their signal response could have varied, and the interfaces between the sensing plate and air, PDMS, and liquid were different causing different optical distortions. Nevertheless, this error was considered acceptable because it allowed for shorter measurement times, especially for the calibration phase. However, the resulting error must be understood and taken into account. For future measurements, a calibration time of 30 min per oxygen concentration is recommended with a gas application to the cover and scavenging channel. The measurement can be performed before or after the calibration, which makes no difference except for the water that evaporates from the cell compartment over time.

In terms of the number and specific oxygen concentrations used, concentrations in the lower range close to the levels of interest are recommended. Since the measurements were done in a range of hypoxia for neurons with oxygen levels of about 3 %, calibration gases with concentrations of 0 %, 1 %, and 5 % were considered most important. In addition, a calibration point of 10 % or 19 % oxygen can be added at the cost of a longer calibration time. It is important to note that the values above the highest calibration concentration used cannot be considered accurate as the measurement response is not linear and therefore the data is not properly calibrated.

4.6.1 Consideration of cellular oxygen consumption

For future measurements and as a design consideration for improved setups, the cellular oxygen consumption needs to be considered as well.

For the cellular oxygen consumption, a value of 7.7e-16 mol/(cell*s) was used based on [111]. The number of cells was approximated to be 1e4 and the volume of the cell compartment was estimated as 47.75 µl, based on the CAD model. The oxygen concentration at equilibrium was calculated to be 9.46e-9 mol of oxygen at incubator conditions.

Based on these conditions, it was estimated that the cells consume the entire oxygen within 20.5 min assuming that no new oxygen is diffusing into the medium. In the chosen concept with the submerged oxygen-blocking structure, the directly available volume for the cells is significantly smaller, leading to the assumption that the cells will use the available oxygen within minutes. Running long experiments with applied scavengers might lead to anoxic conditions and cell apoptosis. Therefore the consideration of cellular oxygen consumption together with the active oxygen scavenging is recommended. In addition, it may be beneficial to perform ratiometric oxygen measurements with live cells and add cellular oxygen consumption to the simulation models.

5. CONCLUSION AND FUTURE ASPECTS

The goal of this thesis was to develop an approach to extend an existing cell culture device with targeted oxygen level control to achieve localized hypoxia for cell studies. This goal was achieved by building a working prototype and proving its oxygen-controlling abilities using two-dimensional ratiometric oxygen measurements. Data about the oxygen profile and levels in proximity to the cells was gathered and compared to simulations. This project involved many disciplines such as system design and simulations, clean room microfabrication of molds, chip molding, and assembly, measurement setup design, measurement execution, and data analysis.

Three concepts were designed and pre-evaluated using a weighted evaluation, and the two most promising were compared using simulations. The selected design featured scavenging channels around each cell compartment routed through two layers of PDMS. This allowed for separate oxygen control of each cell compartment and the scavenging channels could be closer to the cells, reducing the resulting oxygen gradient. Besides the aforementioned manufacturing challenges, the design also had some downsides. While the submerged oxygen-blocking structure hindered the diffusion of oxygen to the cells from the rest of the medium, it also impeded the diffusion of nutrients toward the cells. Due to the long time to reach hypoxic conditions and a very small amount of nutrients available below the structure, the cells might starve before hypoxia is reached. In parallel with the simulations, manufacturability tests were conducted to produce thin PDMS membranes with openings to test the viability of three selected techniques. An optimal process was found using a polycarbonate plate and sufficient pressure to displace the PDMS. In addition, rotating the plate was found to aid in the displacement of excess PDMS and reduce the number of flaps and unopened structures. With further optimization and experience, this process can be used for more complex and specialized assemblies. However, several simplifications were made to the selected design to improve the initial manufacturability of the selected prototype. The final selected chip was still two-layered but had only one scavenging channel routed around a single cell compartment within one layer. In addition, a passive oxygen-blocking structure was added that was submerged in the cell compartment to block oxygen diffusion from above in an attempt to reduce the oxygen gradient and achieve lower oxygen concentrations in the center of the cell compartment. This prototype was considered to be a pathfinder to test the new chip fabrication processes of multilayer chips with membranes containing openings and microstructures, and based on the results of this work, further development will be possible.

Molding both layers from PDMS was successful. The resulting quality of the microtunnel layers was stable. The cell compartments were mostly open, and if not, they could be easily opened by hand using tweezers. The amount of thin PDMS flaps was acceptable and occurred mostly in the corners. The improved second version of the scavenging channel layers was of good quality but suffered from bubble formation around the 3D-printed inserts. This is a common problem with this type of chip, according to Lassi Sukki of the Micro- and Nanosystems Research Group at Tampere University, who designed the original chip. Therefore, more chips were molded to sort out the ones with few bubbles. When aligning the first version of the scavenging channel layers, a problem with uneven shrinkage was detected. Initially, a shrinkage of 1 % was considered for both layers. However, the microtunnel layer remained in the mold which prevented it from shrinking. To make them align, a revised and slightly upscaled version of the scavenging channel layer was fabricated. Additionally, the scavenging channel around the back and sides was moved further away to achieve a greater misalignment tolerance. When building similar systems, it is important to leave the microtunnel layer in its original size and only scale up the scavenging channel layer. The alignment of the chips proved difficult due to reflections from the wafer under the microtunnel layer. The edges of the microtunnel layer were blurred and could not be clearly seen, preventing a clean alignment. In addition, the rotational alignment had to be done by hand, while the translational alignment could be done using precision screws. If these two difficulties could be corrected in future work, chips with smaller features and even better alignment quality could be assembled. All of the chips that showed visually good alignment quality and that were leak tested withstood at least 100 mBar, indicating that the bonding process works well and that these scavenging channel geometries are suitable in terms of their aspect ratio. Initially, there was concern that the narrow scavenging channel walls facing the cell compartment would not bond properly, and would bend or stick to other parts of the chip. However, these concerns were not realized and the scavenging channel walls proved to bond very well without deforming.

Before using the chips for measurements, it was found important to treat them to be hydrophilic to reduce bubble formation during assembly. For other chips in cell culture, this was usually done with a polyvinylpyrrolidone (PVP) treatment, as it is more stable in the long term compared to an oxygen plasma treatment alone. Here, however, two of the three chips measured only received a hydrophilic oxygen plasma treatment immediately prior to the measurement, which greatly improved their preparation for the measurements. During the long-term measurements, evaporation of the test medium was a problem, even though the measurements were performed at room temperature and the cell compartments were covered. At temperatures of 37 ℃, as used in cell culture, evaporation will be a major problem and the cell compartments will need to be expanded, as is currently the case in the regular MEMO chip setup. When comparing the measurements with the rerun simulations for room temperature conditions, it was found that they agree very well, as far as they are comparable, since the simulations were a 2D abstraction of a 3D system. Also, there were many influences that might have affected the measurements which were discussed in detail in Section 4.5.5. All in all, the current simulation models were considered to be accurate and can be used for the simulation of the system and for the development of further improved prototypes.

An additional estimation of the oxygen consumption of the cells was performed and is described in Section 4.6.1. Based on this, it was found that the cells consume all the oxygen in the cell compartment within 20.5 min, assuming that no new oxygen diffuses into the cell compartment. This is especially important for the much smaller part of the cell compartment below the submerged oxygen-blocking structure where the cells are located. Here the oxygen would be depleted within minutes. If the experiments were run for 75 min with the scavenger, the cells might reach anoxic oxygen conditions and die. It will be important to consider the effects of the cells when designing the cell experiments. In addition, it may be beneficial to perform ratiometric oxygen measurements with live cells and add cellular oxygen consumption to the simulation models.

When not considering the cells' own oxygen consumption this build and measured approach has a rather large time constant. Additionally, the cells have a limited amount of nutrients available due to the submerged oxygen-blocking structure, which obstructs nutrient diffusion. With such long time constants, there may be a problem with the cells starving before hypoxic levels can be reached. This could cause cell responses that are not specifically due to hypoxic conditions to distort the measurement results. However, this would need to be studied in detail before drawing any final conclusions.

While this chip in this particular configuration may not yet be viable for cell culture testing due to the issues mentioned above, it surely will be with further improvements. Also, if some of the difficulties encountered during the assembly can be overcome, a more sophisticated system will be possible. This specific prototype served as an excellent test bed for the new fabrication techniques and for the verification of the simulation models and can be optimized to be used with cells.

REFERENCES

[1] T. Vos, A. D. Flaxman, S. Abdalla, *et al.*, “Disability-adjusted life years (DALYs) for 291 diseases and injuries in 21 regions, 1990–2010: A systematic analysis for the Global Burden of Disease Study 2010,” eng, *The Lancet (British edition)*, vol. 380, no. 9859, pp. 2197–2223, 2012, Place: England Publisher: Elsevier Ltd, ISSN: 0140-6736. DOI: 10.1016/S0140-6736(12)61689-4.

[2] O. Devinsky, A. Vezzani, T. J. O’Brien, *et al.*, “Epilepsy,” en, *Nature Reviews Disease Primers*, vol. 4, no. 1, pp. 1–24, May 2018, Number: 1 Publisher: Nature Publishing Group, ISSN: 2056-676X. DOI: 10.1038/nrdp.2018.24. [Online]. Available: https://www.nature.com/articles/nrdp201824 (visited on 05/03/2023).

[3] A. I. Grainger, M. C. King, D. A. Nagel, H. R. Parri, M. D. Coleman, and E. J. Hill, “In vitro Models for Seizure-Liability Testing Using Induced Pluripotent Stem Cells,” eng, *Frontiers in neuroscience*, vol. 12, pp. 590–590, 2018, Place: Switzerland Publisher: Frontiers Research Foundation, ISSN: 1662-4548. DOI: 10.3389/fnins.2018.00590.

[4] K. Fabre, B. Berridge, W. R. Proctor, *et al.*, “Introduction to a manuscript series on the characterization and use of microphysiological systems (MPS) in pharmaceutical safety and ADME applications,” eng, *Lab on a chip*, vol. 20, no. 6, pp. 1049–1057, 2020, Place: England Publisher: Royal Society of Chemistry, ISSN: 1473-0197. DOI: 10.1039/c9lc01168d.

[5] A. Pelkonen, R. Mzezewa, L. Sukki, *et al.*, “A modular brain-on-a-chip for modelling epileptic seizures with functionally connected human neuronal networks,” en, *Biosensors and Bioelectronics*, vol. 168, p. 112 553, Nov. 2020, ISSN: 0956-5663. DOI: 10.1016/j.bios.2020.112553. [Online]. Available: https://www.sciencedirect.com/science/article/pii/S0956566320305455 (visited on 01/12/2023).

[6] Y. Xu and Q. Fan, “Relationship between chronic hypoxia and seizure susceptibility,” *CNS Neuroscience & Therapeutics*, vol. 28, no. 11, pp. 1689–1705, Aug. 2022, ISSN: 1755-5930. DOI: 10.1111/cns.13942. [Online]. Available: https://www.ncbi.nlm.nih.gov/pmc/articles/PMC9532927/ (visited on 05/03/2023).

[7] M. D. Brennan, M. L. Rexius-Hall, L. J. Elgass, and D. T. Eddington, “Oxygen control with microfluidics,” en, *Lab on a Chip*, vol. 14, no. 22, pp. 4305–4318, Oct. 2014, Publisher: The Royal Society of Chemistry, ISSN: 1473-0189. DOI: 10.1039/C4LC00853G. [Online]. Available: https://pubs.rsc.org/en/content/articlelanding/2014/lc/c4lc00853g (visited on 01/13/2023).

[8] S. M. Grist, J. C. Schmok, M.-C. A. Liu, L. Chrostowski, and K. C. Cheung, "Designing a Microfluidic Device with Integrated Ratiometric Oxygen Sensors for the Long-Term Control and Monitoring of Chronic and Cyclic Hypoxia," eng, *Sensors (Basel, Switzerland)*, vol. 15, no. 8, pp. 20 030–20 052, 2015, Place: Switzerland Publisher: MDPI, ISSN: 1424-8220. DOI: 10.3390/s150820030.

[9] K. Tornberg, H. Välimäki, S. Valaskivi, *et al.*, "Compartmentalized organ-on-a-chip structure for spatiotemporal control of oxygen microenvironments," eng, *Biomedical microdevices*, vol. 24, no. 4, pp. 34–34, 2022, Place: New York Publisher: Springer US, ISSN: 1387-2176. DOI: 10.1007/s10544-022-00634-y.

[10] J. J. F. Sleeboom, J. M. J. den Toonder, and C. M. Sahlgren, "MDA-MB-231 breast cancer cells and their CSC population migrate towards low oxygen in a microfluidic gradient device," eng, *International journal of molecular sciences*, vol. 19, no. 10, pp. 3047–, 2018, Place: Switzerland Publisher: MDPI, ISSN: 1422-0067. DOI: 10.3390/ijms19103047.

[11] S. Wiebe, W. T. Blume, J. P. Girvin, and M. Eliasziw, "A Randomized, Controlled Trial of Surgery for Temporal-Lobe Epilepsy," eng, *The New England journal of medicine*, vol. 345, no. 5, pp. 311–318, 2001, Publisher: Massachusetts Medical Society, ISSN: 0028-4793. DOI: 10.1056/NEJM200108023450501.

[12] W. Niu and J. M. Parent, "Modeling genetic epilepsies in a dish," en, *Developmental Dynamics*, vol. 249, no. 1, pp. 56–75, 2020, _eprint: https://onlinelibrary.wiley.com/doi/pdf/10.1002/dvdy.79, ISSN: 1097-0177. DOI: 10.1002/dvdy.79. [Online]. Available: https://onlinelibrary.wiley.com/doi/abs/10.1002/dvdy.79 (visited on 05/04/2023).

[13] S. Nallamshetty, S. Y. Chan, and J. Loscalzo, "Hypoxia: A master regulator of microRNA biogenesis and activity," eng, *Free radical biology & medicine*, vol. 64, pp. 20–30, 2013, Place: United States Publisher: Elsevier Inc, ISSN: 0891-5849. DOI: 10.1016/j.freeradbiomed.2013.05.022.

[14] T. Zhao, C.-p. Zhang, Z.-h. Liu, *et al.*, "Hypoxia-driven proliferation of embryonic neural stem/progenitor cells - role of hypoxia-inducible transcription factor-1," eng, *The FEBS journal*, vol. 275, no. 8, pp. 1824–1834, 2008, Place: Oxford, UK Publisher: Blackwell Publishing Ltd, ISSN: 1742-464X. DOI: 10.1111/j.1742-4658.2008.06340.x.

[15] Y. B. Kang, J. Eo, B. Bulutoglu, M. L. Yarmush, and O. B. Usta, "Progressive hypoxia-on-a-chip: An in vitro oxygen gradient model for capturing the effects of hypoxia on primary hepatocytes in health and disease," eng, *Biotechnology and bioengineering*, vol. 117, no. 3, pp. 763–775, 2020, Place: United States Publisher: Wiley Subscription Services, Inc, ISSN: 0006-3592. DOI: 10.1002/bit.27225.

[16] T. Kietzmann, "Metabolic zonation of the liver: The oxygen gradient revisited," eng, *Redox biology*, vol. 11, pp. 622–630, 2017, Place: Netherlands Publisher: Elsevier B.V, ISSN: 2213-2317. DOI: 10.1016/j.redox.2017.01.012.

[17] V. Palacio-Castaneda, N. Velthuijs, S. L. Gac, and W. P. R. Verdurmen, “Oxygen control: The often overlooked but essential piece to create better in vitro systems,” eng, *Lab on a chip*, vol. 22, no. 6, pp. 1068–1092, 2022, Place: England Publisher: Royal Society of Chemistry, ISSN: 1473-0197. DOI: 10.1039/d1lc00603g.

[18] A. Carreau, B. E. Hafny-Rahbi, A. Matejuk, C. Grillon, and C. Kieda, “Why is the partial oxygen pressure of human tissues a crucial parameter? Small molecules and hypoxia,” eng, *Journal of cellular and molecular medicine*, vol. 15, no. 6, pp. 1239–1253, 2011, Place: Oxford, UK Publisher: Blackwell Publishing Ltd, ISSN: 1582-1838. DOI: 10.1111/j.1582-4934.2011.01258.x.

[19] G. Chen and A. F. Palmer, “Hemoglobin-based oxygen carrier and convection enhanced oxygen transport in a hollow fiber bioreactor,” eng, *Biotechnology and bioengineering*, vol. 102, no. 6, pp. 1603–1612, 2009, Place: Hoboken Publisher: Wiley Subscription Services, Inc., A Wiley Company, ISSN: 0006-3592. DOI: 10.1002/bit.22200.

[20] J.-O. Dunn, M. G. Mythen, and M. P. Grocott, “Physiology of oxygen transport,” eng, *BJA education*, vol. 16, no. 10, pp. 341–348, 2016, Publisher: Elsevier Ltd, ISSN: 2058-5349. DOI: 10.1093/bjaed/mkw012.

[21] Y.-C. Tung, *Organs-on-chips*, eng. MDPI - Multidisciplinary Digital Publishing Institute, 2020, ISBN: 978-3-03928-918-9.

[22] D. Karthikeyan, V. Kavitha, and R. Sathishkumar, “Mathematical Modeling on Blood flow through a stenosed artery with Heat Transfer under the Impact of Slip condition,” eng, *Journal of physics. Conference series*, vol. 1850, no. 1, pp. 12 127–, 2021, Place: Bristol Publisher: IOP Publishing, ISSN: 1742-6588. DOI: 10.1088/1742-6596/1850/1/012127.

[23] A. Paul, *Thermodynamics, Diffusion and the Kirkendall Effect in Solids*, eng, 1st ed. 2014. Cham: Springer International Publishing, 2014, ISBN: 978-3-319-07461-0. DOI: 10.1007/978-3-319-07461-0.

[24] K. P. Ivanov, “Function of alveoli as a result of evolutionary development of respiratory system in mammals,” eng, *Journal of evolutionary biochemistry and physiology*, vol. 49, no. 1, pp. 78–83, 2013, Place: Dordrecht Publisher: SP MAIK Nauka/Interperiodica, ISSN: 0022-0930. DOI: 10.1134/S002209301301009X.

[25] W. Xing, M. Yin, Q. Lv, Y. Hu, C. Liu, and J. Zhang, “1 - Oxygen Solubility, Diffusion Coefficient, and Solution Viscosity,” en, in *Rotating Electrode Methods and Oxygen Reduction Electrocatalysts*, W. Xing, G. Yin, and J. Zhang, Eds., Amsterdam: Elsevier, Jan. 2014, pp. 1–31, ISBN: 978-0-444-63278-4. DOI: 10.1016/B978-0-444-63278-4.00001-X. [Online]. Available: https://www.sciencedirect.com/science/article/pii/B978044463278400001X (visited on 04/23/2023).

[26] T. L. Place, F. E. Domann, and A. J. Case, “Limitations of oxygen delivery to cells in culture: An underappreciated problem in basic and translational research,” en, *Free Radical Biology and Medicine*, vol. 113, pp. 311–322, Dec. 2017, ISSN: 0891-

5849. DOI: 10.1016/j.freeradbiomed.2017.10.003. [Online]. Available: https://www.sciencedirect.com/science/article/pii/S0891584917307864 (visited on 02/22/2023).

[27] J. Welty, G. L. Rorrer, and D. G. Foster, *Fundamentals of Momentum, Heat, and Mass Transfer*, English, 7th ed. Wiley, Feb. 2019, ISBN: 978-1-119-49541-3. (visited on 01/30/2023).

[28] S. Kanehashi, T. Sato, S. Sato, and K. Nagai, "Microstructure and Gas Diffusivity of Poly(dimethylsiloxane) Dense Membrane Using Molecular Dynamics (MD) Simulation," eng, *Transactions of the Materials Research Society of Japan*, vol. 37, no. 3, pp. 439–442, 2012, ISSN: 1382-3469. DOI: 10.14723/tmrsj.37.439.

[29] B. A. Wittenberg and J. B. Wittenberg, "Transport of oxygen in muscle," eng, *Annual review of physiology*, vol. 51, no. 1, pp. 857–878, 1989, Place: United States, ISSN: 0066-4278. DOI: 10.1146/annurev.ph.51.030189.004233.

[30] M.-T. Arango, P. Quintero-Ronderos, J. Castiblanco, and G. Montoya-Ortíz, "Cell culture and cell analysis," en, in *Autoimmunity: From Bench to Bedside [Internet]*, El Rosario University Press, Jul. 2013. [Online]. Available: https://www.ncbi.nlm.nih.gov/books/NBK459464/ (visited on 05/05/2023).

[31] J. Seok, H. S. Warren, A. G. Cuenca, *et al.*, "Genomic responses in mouse models poorly mimic human inflammatory diseases," eng, *Proceedings of the National Academy of Sciences - PNAS*, vol. 110, no. 9, pp. 3507–3512, 2013, Place: United States Publisher: National Academy of Sciences, ISSN: 0027-8424. DOI: 10.1073/pnas.1222878110.

[32] R. Franco and A. Cedazo-Minguez, "Successful therapies for Alzheimer's disease: Why so many in animal models and none in humans?" eng, *Frontiers in pharmacology*, vol. 5, pp. 146–146, 2014, Place: Switzerland Publisher: Frontiers Media, ISSN: 1663-9812. DOI: 10.3389/fphar.2014.00146.

[33] D. E. Ingber, "Human organs-on-chips for disease modelling, drug development and personalized medicine," eng, *Nature reviews. Genetics*, vol. 23, no. 8, pp. 467–491, 2022, Place: England Publisher: Nature Publishing Group, ISSN: 1471-0056. DOI: 10.1038/s41576-022-00466-9.

[34] Z. Zhu and D. Huangfu, "Human pluripotent stem cells: An emerging model in developmental biology," en, *Development (Cambridge, England)*, vol. 140, no. 4, p. 705, Feb. 2013, Publisher: Company of Biologists. DOI: 10.1242/dev.086165. [Online]. Available: https://www.ncbi.nlm.nih.gov/pmc/articles/PMC3557771/ (visited on 07/11/2023).

[35] K. Takahashi, K. Tanabe, M. Ohnuki, *et al.*, "Induction of Pluripotent Stem Cells from Adult Human Fibroblasts by Defined Factors," eng, *Cell*, vol. 131, no. 5, pp. 861–872, 2007, Place: United States Publisher: Elsevier Inc, ISSN: 0092-8674. DOI: 10.1016/j.cell.2007.11.019.

[36] S. W. Baran, P. C. Brown, A. R. Baudy, *et al.*, “Perspectives on the evaluation and adoption of complex in vitro models in drug development: Workshop with the FDA and the pharmaceutical industry (IQ MPS Affiliate),” eng, *ALTEX, alternatives to animal experimentation*, vol. 39, no. 2, pp. 297–, 2022, Place: Germany Publisher: Springer Spektrum, ISSN: 1868-596X. DOI: 10.14573/altex.2112203.

[37] M. Kapałczyńska, T. Kolenda, W. Przybyła, *et al.*, “2D and 3D cell cultures - a comparison of different types of cancer cell cultures,” eng, *Archives of medical science*, vol. 14, no. 4, pp. 910–919, 2018, Place: Poland Publisher: Termedia Publishing House, ISSN: 1734-1922. DOI: 10.5114/aoms.2016.63743.

[38] A. Cacciamali, R. Villa, and S. Dotti, “3D Cell Cultures: Evolution of an Ancient Tool for New Applications,” *Frontiers in Physiology*, vol. 13, p. 836 480, Jul. 2022, ISSN: 1664-042X. DOI: 10.3389/fphys.2022.836480. [Online]. Available: https://www.ncbi.nlm.nih.gov/pmc/articles/PMC9353320/ (visited on 06/28/2023).

[39] M. Sun, A. Liu, X. Yang, *et al.*, “3D Cell Culture—Can It Be As Popular as 2D Cell Culture?” eng, *Advanced NanoBiomed Research (Online)*, vol. 1, no. 5, 2 000 066–n/a, 2021, Publisher: Wiley-VCH, ISSN: 2699-9307. DOI: 10.1002/anbr.202000066.

[40] N.-E. Ryu, S.-H. Lee, and H. Park, “Spheroid Culture System Methods and Applications for Mesenchymal Stem Cells,” *Cells*, vol. 8, no. 12, p. 1620, Dec. 2019, ISSN: 2073-4409. DOI: 10.3390/cells8121620. [Online]. Available: https://www.ncbi.nlm.nih.gov/pmc/articles/PMC6953111/ (visited on 05/07/2023).

[41] K. Białkowska, P. Komorowski, M. Bryszewska, and K. Miłowska, “Spheroids as a Type of Three-Dimensional Cell Cultures—Examples of Methods of Preparation and the Most Important Application,” *International Journal of Molecular Sciences*, vol. 21, no. 17, p. 6225, Aug. 2020, ISSN: 1422-0067. DOI: 10.3390/ijms21176225. [Online]. Available: https://www.ncbi.nlm.nih.gov/pmc/articles/PMC7503223/ (visited on 05/07/2023).

[42] N. de Souza, “Organoids,” eng, *Nature methods*, vol. 15, no. 1, pp. 23–23, 2018, Place: New York Publisher: Nature Publishing Group, ISSN: 1548-7091. DOI: 10.1038/nmeth.4576.

[43] S. Price, S. Bhosle, E. Gonçalves, *et al.*, “A suspension technique for efficient large-scale cancer organoid culturing and perturbation screens,” en, *Scientific Reports*, vol. 12, no. 1, p. 5571, Apr. 2022, Number: 1 Publisher: Nature Publishing Group, ISSN: 2045-2322. DOI: 10.1038/s41598-022-09508-y. [Online]. Available: https://www.nature.com/articles/s41598-022-09508-y (visited on 05/05/2023).

[44] T.-K. Huang and K. A. McDonald, “Bioreactor engineering for recombinant protein production in plant cell suspension cultures,” eng, *Biochemical engineering journal*, vol. 45, no. 3, pp. 168–184, 2009, Place: Amsterdam Publisher: Elsevier B.V, ISSN: 1369-703X. DOI: 10.1016/j.bej.2009.02.008.

[45] M.-H. Wu, S.-B. Huang, and G.-B. Lee, “Microfluidic cell culture systems for drug research,” eng, *Lab on a chip*, vol. 10, no. 8, pp. 939–, 2010, Place: England, ISSN: 1473-0197. DOI: 10.1039/b921695b.

[46] L. Goers, P. Freemont, and K. M. Polizzi, “Co-culture systems and technologies: Taking synthetic biology to the next level,” eng, *Journal of the Royal Society interface*, vol. 11, no. 96, pp. 20 140 065–, 2014, Place: England Publisher: The Royal Society, ISSN: 1742-5689. DOI: 10.1098/rsif.2014.0065.

[47] M. Häkli, S. Jäntti, T. Joki, *et al.*, “Human Neurons Form Axon-Mediated Functional Connections with Human Cardiomyocytes in Compartmentalized Microfluidic Chip,” eng, *International journal of molecular sciences*, vol. 23, no. 6, pp. 3148–, 2022, Place: Switzerland Publisher: MDPI AG, ISSN: 1422-0067. DOI: 10.3390/ijms23063148.

[48] W. R. Chae and N. Y. Lee, “Monolayer/spheroid co-culture of cells on a PDMS well plate mediated by selective polydopamine coating,” eng, *Journal of materials chemistry. B, Materials for biology and medicine*, vol. 8, no. 44, pp. 118–1116, 2020, Place: England Publisher: Royal Society of Chemistry, ISSN: 2050-750X. DOI: 10.1039/d0tb01589j.

[49] A. Al-Ani, D. Toms, D. Kondro, J. Thundathil, Y. Yu, and M. Ungrin, “Oxygenation in cell culture: Critical parameters for reproducibility are routinely not reported,” *PLoS ONE*, vol. 13, no. 10, e0204269, Oct. 2018, ISSN: 1932-6203. DOI: 10.1371/journal.pone.0204269. [Online]. Available: https://www.ncbi.nlm.nih.gov/pmc/articles/PMC6191109/ (visited on 05/09/2023).

[50] R. S. Shirazi, M. Vyssotski, K. Lagutin, *et al.*, “Neuroprotective activity of new 3-N-acylethanolamines in a focal ischemia stroke model,” eng, *Lipids*, vol. 57, no. 1, pp. 17–31, 2022, Place: Hoboken, USA Publisher: John Wiley & Sons, Inc, ISSN: 0024-4201. DOI: 10.1002/lipd.12326.

[51] P. Erne, A. W. Schoenenberger, D. Burckhardt, *et al.*, “Effects of Percutaneous Coronary Interventions in Silent Ischemia After Myocardial Infarction: The SWISSI II Randomized Controlled Trial,” eng, *JAMA : the journal of the American Medical Association*, vol. 297, no. 18, pp. 1985–1991, 2007, Place: Chicago, IL Publisher: American Medical Association, ISSN: 0098-7484. DOI: 10.1001/jama.297.18.1985.

[52] E. Boscaini, M. L. Alexander, P. Prazeller, and T. D. Märk, “Investigation of fundamental physical properties of a polydimethylsiloxane (PDMS) membrane using a proton transfer reaction mass spectrometer (PTRMS),” eng, *International journal of mass spectrometry*, vol. 239, no. 2, pp. 179–186, 2004, Publisher: Elsevier B.V, ISSN: 1387-3806. DOI: 10.1016/j.ijms.2004.08.011.

[53] B. Harink, S. Le Gac, D. Barata, C. van Blitterswijk, and P. Habibovic, “Microtiter plate-sized standalone chip holder for microenvironmental physiological control in gas-impermeable microfluidic devices,” eng, *Lab on a chip*, vol. 14, no. 11, pp. 1816–1820, 2014, Place: England, ISSN: 1473-0197. DOI: 10.1039/c4lc00190g.

[54] J. M. Ayuso, M. Virumbrales-Muñoz, A. Lacueva, *et al.*, “Development and characterization of a microfluidic model of the tumour microenvironment,” eng, *Scientific reports*, vol. 6, no. 1, pp. 36 086–36 086, 2016, Place: England Publisher: Nature Publishing Group, ISSN: 2045-2322. DOI: 10.1038/srep36086.

[55] G. Mehta, J. Lee, W. Cha, Y.-C. Tung, J. J. Linderman, and S. Takayama, “Hard Top Soft Bottom Microfluidic Devices for Cell Culture and Chemical Analysis,” eng, *Analytical chemistry (Washington)*, vol. 81, no. 10, pp. 3714–3722, 2009, Place: Washington, DC Publisher: American Chemical Society, ISSN: 0003-2700. DOI: 10.1021/ac802178u.

[56] *Baker Ruskinn | Concept | Scimed*, en-US, May 2021. [Online]. Available: https://scimed.com.sg/product/baker-ruskinn-concept/ (visited on 05/09/2023).

[57] I. Kiiski, P. Järvinen, E. Ollikainen, V. Jokinen, and T. Sikanen, “The material-enabled oxygen control in thiol-ene microfluidic channels and its feasibility for subcellular drug metabolism assays under hypoxia in vitro,” eng, *Lab on a chip*, vol. 21, no. 9, pp. 1820–1831, 2021, Place: England Publisher: Royal Society of Chemistry, ISSN: 1473-0197. DOI: 10.1039/d0lc01292k.

[58] D. C. Duffy, J. C. McDonald, O. J. A. Schueller, and G. M. Whitesides, “Rapid Prototyping of Microfluidic Systems in Poly(dimethylsiloxane),” eng, *Analytical chemistry (Washington)*, vol. 70, no. 23, pp. 4974–4984, 1998, Place: Washington, DC Publisher: American Chemical Society, ISSN: 0003-2700. DOI: 10.1021/ac980656z.

[59] B. Ruben, M. Elisa, L. Leandro, *et al.*, “Oxygen plasma treatments of polydimethylsiloxane surfaces: Effect of the atomic oxygen on capillary flow in the microchannels,” eng, *Micro & nano letters*, vol. 12, no. 10, pp. 754–757, 2017, Place: Stevenage Publisher: The Institution of Engineering and Technology, ISSN: 1750-0443. DOI: 10.1049/mnl.2017.0230.

[60] D. Bodas and C. Khan-Malek, “Hydrophilization and hydrophobic recovery of PDMS by oxygen plasma and chemical treatment—An SEM investigation,” eng, *Sensors and actuators. B, Chemical*, vol. 123, no. 1, pp. 368–373, 2007, Publisher: Elsevier B.V, ISSN: 0925-4005. DOI: 10.1016/j.snb.2006.08.037.

[61] S. Hemmilä, J. V. Cauich-Rodríguez, J. Kreutzer, and P. Kallio, “Rapid, simple, and cost-effective treatments to achieve long-term hydrophilic PDMS surfaces,” en, *Applied Surface Science*, vol. 258, no. 24, pp. 9864–9875, Oct. 2012, ISSN: 0169-4332. DOI: 10.1016/j.apsusc.2012.06.044. [Online]. Available: https://www.sciencedirect.com/science/article/pii/S016943321201094X (visited on 05/13/2023).

[62] J. Kuncova-Kallio and P. Kallio, “PDMS and it’s suitability for analytical microfluidic devices,” eng, 2006.

[63] J. C. McDonald, D. C. Duffy, J. R. Anderson, *et al.*, “Fabrication of microfluidic systems in poly(dimethylsiloxane),” eng, *Electrophoresis*, vol. 21, no. 1, pp. 27–40, 2000, Place: Hoboken Publisher: Wiley Subscription Services, Inc., A Wiley

Company, ISSN: 0173-0835. DOI: 10.1002/(SICI)1522-2683(20000101)21:1<27::AID-ELPS27>3.0.CO;2-C.

[64] A. Lamberti, S. L. Marasso, and M. Cocuzza, "PDMS membranes with tunable gas permeability for microfluidic applications," en, *RSC Advances*, vol. 4, no. 106, pp. 61 415–61 419, 2014, Publisher: Royal Society of Chemistry. DOI: 10.1039/C4RA12934B. [Online]. Available: https://pubs.rsc.org/en/content/articlelanding/2014/ra/c4ra12934b (visited on 05/13/2023).

[65] A. Victor, J. E. Ribeiro, and F. F. Araújo, "Study of PDMS characterization and its applications in biomedicine: A review," eng, *Journal of Mechanical Engineering and Biomechanics*, vol. 4, no. 1, pp. 1–9, 2019, Accepted: 2019-09-03T10:36:22Z Publisher: Rational Publication, ISSN: 2456-219X. DOI: 10.24243/JMEB/4.1.163. [Online]. Available: https://bibliotecadigital.ipb.pt/handle/10198/19528 (visited on 05/13/2023).

[66] T. C. Merkel, V. I. Bondar, K. Nagai, B. D. Freeman, and I. Pinnau, "Gas sorption, diffusion, and permeation in poly(dimethylsiloxane)," eng, *Journal of polymer science. Part B, Polymer physics*, vol. 38, no. 3, pp. 415–434, 2000, Place: New York Publisher: John Wiley & Sons, Inc, ISSN: 0887-6266. DOI: 10.1002/(SICI)1099-0488(20000201)38:3<415::AID-POLB8>3.0.CO;2-Z.

[67] F. C. Sales, R. M. Ariati, V. T. Noronha, and J. E. Ribeiro, "Mechanical Characterization of PDMS with Different Mixing Ratios," eng, *Procedia Structural Integrity*, vol. 37, pp. 383–388, 2022, Publisher: Elsevier B.V, ISSN: 2452-3216. DOI: 10.1016/j.prostr.2022.01.099.

[68] J. H. Sung and M. L. Shuler, "Microtechnology for Mimicking In Vivo Tissue Environment," eng, *Annals of biomedical engineering*, vol. 40, no. 6, pp. 1289–1300, 2012, Place: Boston Publisher: Springer US, ISSN: 0090-6964. DOI: 10.1007/s10439-011-0491-2.

[69] B. van Meer, H. de Vries, K. Firth, *et al.*, "Small molecule absorption by PDMS in the context of drug response bioassays," *Biochemical and Biophysical Research Communications*, vol. 482, no. 2, pp. 323–328, Jan. 2017, ISSN: 0006-291X. DOI: 10.1016/j.bbrc.2016.11.062. [Online]. Available: https://www.ncbi.nlm.nih.gov/pmc/articles/PMC5240851/ (visited on 05/13/2023).

[70] S.-S. D. Carter, A.-R. Atif, S. Kadekar, *et al.*, "PDMS leaching and its implications for on-chip studies focusing on bone regeneration applications," en, *Organs-on-a-Chip*, vol. 2, p. 100 004, Dec. 2020, ISSN: 2666-1020. DOI: 10.1016/j.ooc.2020.100004. [Online]. Available: https://www.sciencedirect.com/science/article/pii/S2666102020300045 (visited on 05/13/2023).

[71] J. N. Lee, C. Park, and G. M. Whitesides, "Solvent Compatibility of Poly(dimethylsiloxane)-Based Microfluidic Devices," eng, *Analytical chemistry (Washington)*, vol. 75, no. 23, pp. 6544–6554, 2003, Place: Washington, DC Publisher: American Chemical Society, ISSN: 0003-2700. DOI: 10.1021/ac0346712.

[72] J. Huft, D. J. Da Costa, D. Walker, and C. L. Hansen, “Three-dimensional large-scale microfluidic integration by laser ablation of interlayer connections,” eng, *Lab on a chip*, vol. 10, no. 18, pp. 2358–2365, 2010, Place: England, ISSN: 1473-0197. DOI: 10.1039/c004051g.

[73] T. Silva Santisteban, R. Zengerle, and M. Meier, “Through-holes, cavities and perforations in polydimethylsiloxane (PDMS) chips,” eng, *RSC advances*, vol. 4, no. 89, pp. 48 012–48 016, 2014, ISSN: 2046-2069. DOI: 10.1039/C4RA09586C.

[74] N. Qu, X. Chen, H. Li, and D. Zhu, “Fabrication of PDMS micro through-holes for electrochemical micromachining,” eng, *International journal of advanced manufacturing technology*, vol. 72, no. 1-4, pp. 487–494, 2014, Place: London Publisher: Springer London, ISSN: 0268-3768. DOI: 10.1007/s00170-014-5702-1.

[75] D. T. Chiu, N. L. Jeon, S. Huang, *et al.*, “Patterned Deposition of Cells and Proteins onto Surfaces by Using Three-Dimensional Microfluidic Systems,” eng, *Proceedings of the National Academy of Sciences - PNAS*, vol. 97, no. 6, pp. 2408–2413, 2000, Place: United States Publisher: National Academy of Sciences of the United States of America, ISSN: 0027-8424. DOI: 10.1073/pnas.040562297.

[76] C. F. Carlborg, T. Haraldsson, M. Cornaglia, G. Stemme, and W. van der Wijngaart, “A High-Yield Process for 3-D Large-Scale Integrated Microfluidic Networks in PDMS,” *Journal of Microelectromechanical Systems*, vol. 19, no. 5, pp. 1050–1057, Oct. 2010, Conference Name: Journal of Microelectromechanical Systems, ISSN: 1941-0158. DOI: 10.1109/JMEMS.2010.2067203.

[77] F. van Rossem, J. G. Bomer, H. L. de Boer, *et al.*, “Sensing oxygen at the millisecond time-scale using an ultra-microelectrode array (UMEA),” eng, *Sensors and actuators. B, Chemical*, vol. 238, pp. 1008–1016, 2017, Place: Lausanne Publisher: Elsevier B.V, ISSN: 0925-4005. DOI: 10.1016/j.snb.2016.06.156.

[78] C.-C. Wu, T. Yasukawa, H. Shiku, and T. Matsue, “Fabrication of miniature Clark oxygen sensor integrated with microstructure,” eng, *Sensors and actuators. B, Chemical*, vol. 110, no. 2, pp. 342–349, 2005, Publisher: Elsevier B.V, ISSN: 0925-4005. DOI: 10.1016/j.snb.2005.02.014.

[79] C.-C. Wu, T. Saito, T. Yasukawa, *et al.*, “Microfluidic chip integrated with amperometric detector array for in situ estimating oxygen consumption characteristics of single bovine embryos,” eng, *Sensors and actuators. B, Chemical*, vol. 125, no. 2, pp. 680–687, 2007, Publisher: Elsevier B.V, ISSN: 0925-4005. DOI: 10.1016/j.snb.2007.03.017.

[80] K. Hiramoto, M. Yasumi, H. Ushio, *et al.*, “Development of Oxygen Consumption Analysis with an on-Chip Electrochemical Device and Simulation,” eng, *Analytical chemistry (Washington)*, vol. 89, no. 19, pp. 10 303–10 310, 2017, Place: United States Publisher: American Chemical Society, ISSN: 0003-2700. DOI: 10.1021/acs.analchem.7b02074.

[81] B. Ungerböck, V. Charwat, P. Ertl, and T. Mayr, “Microfluidic oxygen imaging using integrated optical sensor layers and a color camera,” eng, *Lab on a chip*, vol. 13, no. 8, pp. 1593–161, 2013, Place: England, ISSN: 1473-0197. DOI: 10.1039/c3lc41315b.

[82] G. Mehta, K. Mehta, D. Sud, *et al.*, “Quantitative measurement and control of oxygen levels in microfluidic poly(dimethylsiloxane) bioreactors during cell culture,” eng, *Biomedical microdevices*, vol. 9, no. 2, pp. 123–134, 2007, Place: United States Publisher: Springer, ISSN: 1387-2176. DOI: 10.1007/s10544-006-9005-7.

[83] B. Ungerböck, A. Pohar, T. Mayr, and I. Plazl, “Online oxygen measurements inside a microreactor with modeling of transport phenomena,” eng, *Microfluidics and nanofluidics*, vol. 14, no. 3-4, pp. 565–574, 2013, Place: Berlin/Heidelberg Publisher: Springer-Verlag, ISSN: 1613-4982. DOI: 10.1007/s10404-012-1074-8.

[84] V. Nock, R. J. Blaikie, and T. David, “Patterning, integration and characterisation of polymer optical oxygen sensors for microfluidic devices,” eng, *Lab on a chip*, vol. 8, no. 8, pp. 1300–1307, 2008, Place: England, ISSN: 1473-0197. DOI: 10.1039/b801879k.

[85] Z. Lin, T. Cherng-Wen, P. Roy, and D. Trau, “In-situ measurement of cellular microenvironments in a microfluidic device,” eng, *Lab on a chip*, vol. 9, no. 2, pp. 257–262, 2009, Place: England, ISSN: 1473-0197. DOI: 10.1039/b806907g.

[86] J. I. Peterson, R. V. Fitzgerald, and D. K. Buckhold, “Fiber-optic probe for in vivo measurement of oxygen partial pressure,” eng, *Analytical chemistry (Washington)*, vol. 56, no. 1, pp. 62–67, 1984, Place: Washington, DC Publisher: American Chemical Society, ISSN: 0003-2700. DOI: 10.1021/ac00265a017.

[87] J. P. Fischer and K. Koop-Jakobsen, “The multi fiber optode (MuFO): A novel system for simultaneous analysis of multiple fiber optic oxygen sensors,” eng, *Sensors and actuators. B, Chemical*, vol. 168, pp. 354–359, 2012, Publisher: Elsevier B.V, ISSN: 0925-4005. DOI: 10.1016/j.snb.2012.04.034.

[88] A. Odawara, H. Katoh, N. Matsuda, and I. Suzuki, “Physiological maturation and drug responses of human induced pluripotent stem cell-derived cortical neuronal networks in long-term culture,” eng, *Scientific reports*, vol. 6, no. 1, pp. 26 181–26 181, 2016, Place: England Publisher: Nature Publishing Group, ISSN: 2045-2322. DOI: 10.1038/srep26181.

[89] Z. Sheidaei, P. Akbarzadeh, and N. Kashaninejad, “Advances in numerical approaches for microfluidic cell analysis platforms,” eng, *Journal of science. Advanced materials and devices*, vol. 5, no. 3, pp. 295–307, 2020, Publisher: Elsevier B.V, ISSN: 2468-2179. DOI: 10.1016/j.jsamd.2020.07.008.

[90] S. Chen and G. D. Doolen, “LATTICE BOLTZMANN METHOD FOR FLUID FLOWS,” eng, *Annual review of fluid mechanics*, vol. 30, no. 1, pp. 329–364, 1998, Place: Palo Alto, CA 94303-0139, 4139 El Camino Way, P.O. Box 10139, USA Publisher: Annual Reviews, ISSN: 0066-4189. DOI: 10.1146/annurev.fluid.30.1.329.

[91] G. R. Liu, *Smoothed particle hydrodynamics a meshfree particle method*, eng. Singapore ; World Scientific, 2003, ISBN: 978-1-281-87680-5.

[92] A. R. Lam, D. B. Teplow, H. E. Stanley, and B. Urbanc, “Effects of the Arctic (E22–>G) mutation on amyloid beta-protein folding: Discrete molecular dynamics study,” eng, *Journal of the American Chemical Society*, vol. 130, no. 51, pp. 17 413–17 422, 2008, Place: United States, ISSN: 0002-7863. DOI: 10.1021/ja804984h.

[93] D. Marx, *Ab initio molecular dynamics: basic theory and advanced methods*, eng. Cambridge: University Press, 2009, ISBN: 978-1-107-20216-0.

[94] G. R. Liu, *The finite element method: a practical course*, eng, Second edition. Amsterdam: Elsevier, 2014, ISBN: 978-0-08-099441-3.

[95] Frei, *How Large of a Model Can You Solve with COMSOL®?* en, Jun. 2022. [Online]. Available: https://www.comsol.com/blogs/much-memory-needed-solve-large-comsol-models/ (visited on 04/27/2023).

[96] J.-P. Weiss, *Automatic Time Step and Order Selection in Time-Dependent Problems*, 2019. [Online]. Available: https://www.comsol.com/blogs/automatic-time-step-and-order-selection-in-time-dependent-problems/ (visited on 04/27/2023).

[97] COMSOL, *Using Symmetry to Reduce Model Size*, 2023. [Online]. Available: https://www.comsol.com/support/learning-center/article/Using-Symmetry-to-Reduce-Model-Size-35921 (visited on 04/27/2023).

[98] W. Frei, *Using Adaptive Meshing for Local Solution Improvement*, en, Dec. 2013. [Online]. Available: https://www.comsol.com/blogs/using-adaptive-meshing-local-solution-improvement/ (visited on 04/30/2023).

[99] P. Buchwald, “FEM-based oxygen consumption and cell viability models for avascular pancreatic islets,” eng, *Theoretical biology and medical modelling*, vol. 6, no. 1, pp. 5–5, 2009, Place: England Publisher: BioMed Central Ltd, ISSN: 1742-4682. DOI: 10.1186/1742-4682-6-5.

[100] I. Lee, J. H. Woo, M. Lee, T.-J. Jeon, and S. M. Kim, “Hypoxic Physiological Environments in a Gas-Regulated Microfluidic Device,” eng, *Micromachines (Basel)*, vol. 10, no. 1, pp. 16–, 2018, Place: Switzerland Publisher: MDPI AG, ISSN: 2072-666X. DOI: 10.3390/mi10010016.

[101] M. Zahorodny-Burke, B. Nearingburg, and A. L. Elias, “Finite element analysis of oxygen transport in microfluidic cell culture devices with varying channel architectures, perfusion rates, and materials,” eng, *Chemical engineering science*, vol. 66, no. 23, pp. 6244–6253, 2011, Place: Kidlington Publisher: Elsevier Ltd, ISSN: 0009-2509. DOI: 10.1016/j.ces.2011.09.007.

[102] A.-J. Mäki, M. Peltokangas, J. Kreutzer, S. Auvinen, and P. Kallio, “Modeling carbon dioxide transport in PDMS-based microfluidic cell culture devices,” eng, *Chemical engineering science*, vol. 137, pp. 515–524, 2015, Publisher: Elsevier Ltd, ISSN: 0009-2509. DOI: 10.1016/j.ces.2015.06.065.

[103] M. Skolimowski, M. W. Nielsen, J. Emnéus, *et al.*, "Microfluidic dissolved oxygen gradient generator biochip as a useful tool in bacterial biofilm studies," eng, *Lab on a chip*, vol. 1, no. 16, pp. 2162–2169, 2010, Place: England, ISSN: 1473-0197. DOI: 10.1039/c003558k.

[104] R. Sander, "Compilation of Henry's law constants (version 4.0) for water as solvent," *Atmos. Chem. Phys.,*, vol. 15, pp. 4399–4981, 2015. DOI: doi:10.5194/acp-15-4399-2015.

[105] D. Hillel, *Environmental soil physics*, eng. San Diego, CA: Academic Press, 1998, ISBN: 978-1-281-02498-5.

[106] C. R. Wilke and P. Chang, "Correlation of diffusion coefficients in dilute solutions," eng, *AIChE journal*, vol. 1, no. 2, pp. 264–270, 1955, Place: New York Publisher: American Institute of Chemical Engineers, ISSN: 0001-1541. DOI: 10.1002/aic.690010222.

[107] *SU-8 3000 Permanent Negative Epoxy Photoresist | Kayaku Advanced Materials*, en-US. [Online]. Available: https://kayakuam.com/products/su-8-3000/ (visited on 05/21/2023).

[108] *SU-8 2000 Permanent Negative Epoxy Photoresist | Kayaku*, en-US. [Online]. Available: https://kayakuam.com/products/su-8-2000/ (visited on 05/21/2023).

[109] D. A. Markov, E. M. Lillie, S. P. Garbett, and L. J. McCawley, "Variation in diffusion of gases through PDMS due to plasma surface treatment and storage conditions," *Biomedical microdevices*, vol. 16, no. 1, pp. 91–96, Feb. 2014, ISSN: 1387-2176. DOI: 10.1007/s10544-013-9808-2. [Online]. Available: https://www.ncbi.nlm.nih.gov/pmc/articles/PMC3945670/ (visited on 05/13/2023).

[110] L. Wang, W. Liu, Y. Wang, *et al.*, "Construction of oxygen and chemical concentration gradients in a single microfluidic device for studying tumor cell-drug interactions in a dynamic hypoxia microenvironment," eng, *Lab on a chip*, vol. 13, no. 4, pp. 695–705, 2013, Place: England, ISSN: 1473-0197. DOI: 10.1039/c2lc40661f.

[111] R. J. McMurtrey, "Analytic Models of Oxygen and Nutrient Diffusion, Metabolism Dynamics, and Architecture Optimization in Three-Dimensional Tissue Constructs with Applications and Insights in Cerebral Organoids," eng, *Tissue engineering. Part C, Methods*, vol. 22, no. 3, pp. 221–249, 2016, Place: United States Publisher: Mary Ann Liebert, Inc, ISSN: 1937-3384. DOI: 10.1089/ten.tec.2015.0375.

APPENDIX A: GLASSWARE FOR SILANE TREATMENT

Here, the glassware used while silane coating the microscope slides is shown. The first image shows the vessel for the methanol AEAPS mixture on the right, the slide holder with ten slides in the middle, and the lid to prevent methanol evaporation on the left. The slide holder is open at the bottom. This is beneficial for the handling of the slides because they can be easily lifted out of the mixture and transferred to the oven without the need to handle the methanol.

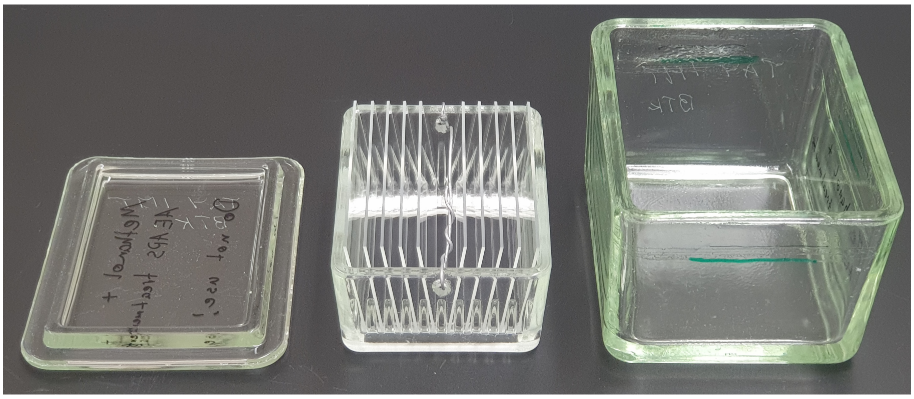

APPENDIX B: PHOTOLITHOGRAPHY MASKS

The four photolithography masks used during mold manufacturing. In order from top to bottom: The mask for Layer 1 of Mold 1 with the microchannels. The mask for Layer 2 of Mold 1 with the structures that keep the cell compartments open. The mask for Layer 1 of Mold 2 contains the scavenger channel and the base where the 3D-printed inserts are glued on. The updated second version mask for Layer 1 of Mold 2 features five different scales and wider scavenger channels.

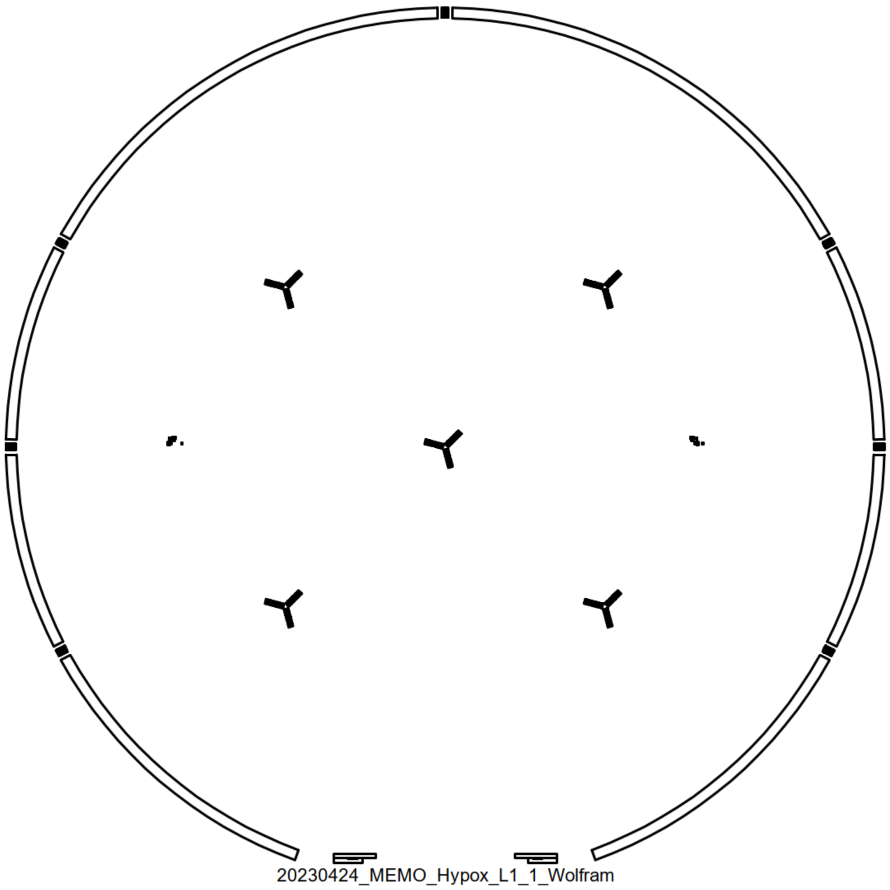

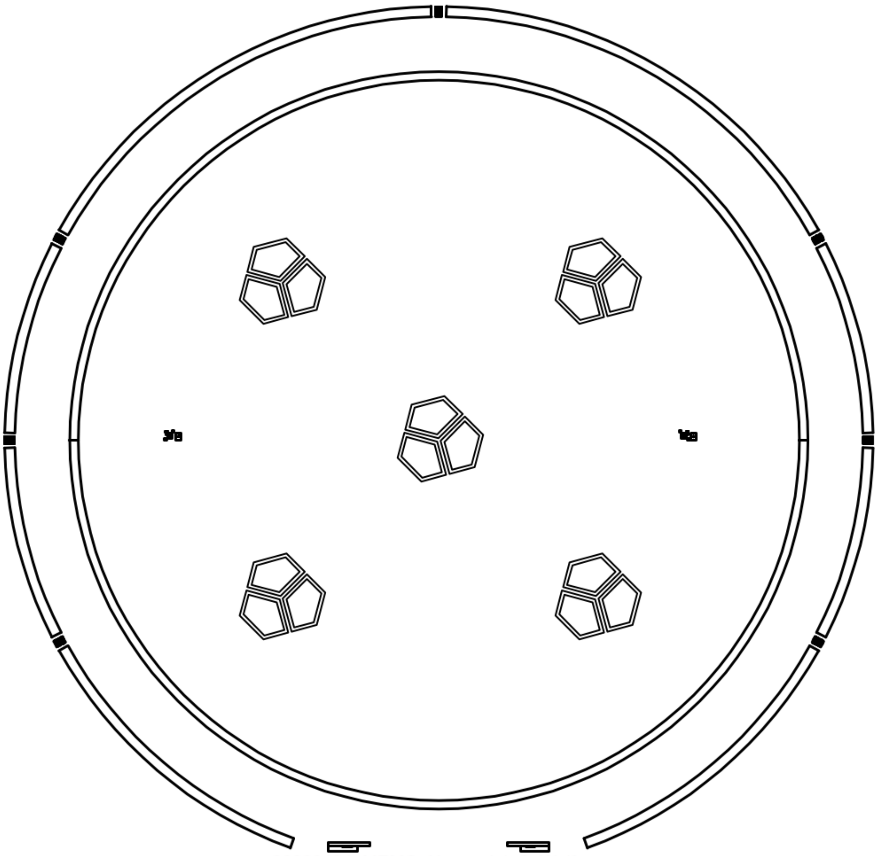

20230424_MEMO_Hypox_L1_2_Wolfram

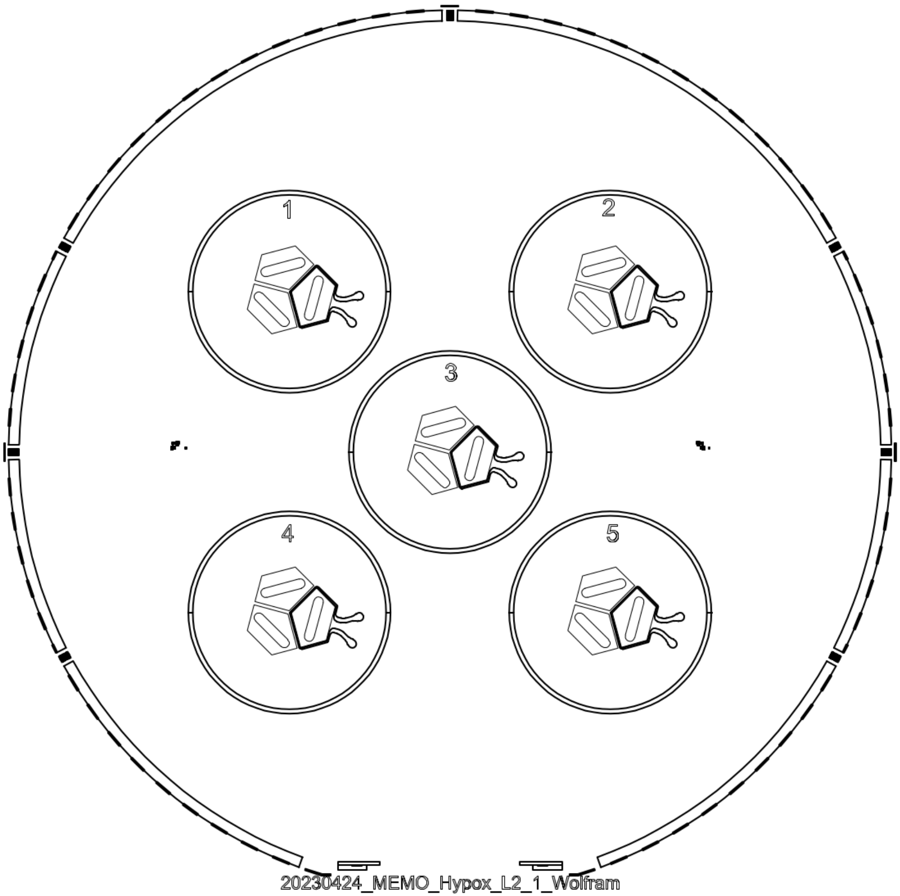

20230424_MEMO_Hypox_L2_1_Wolfram

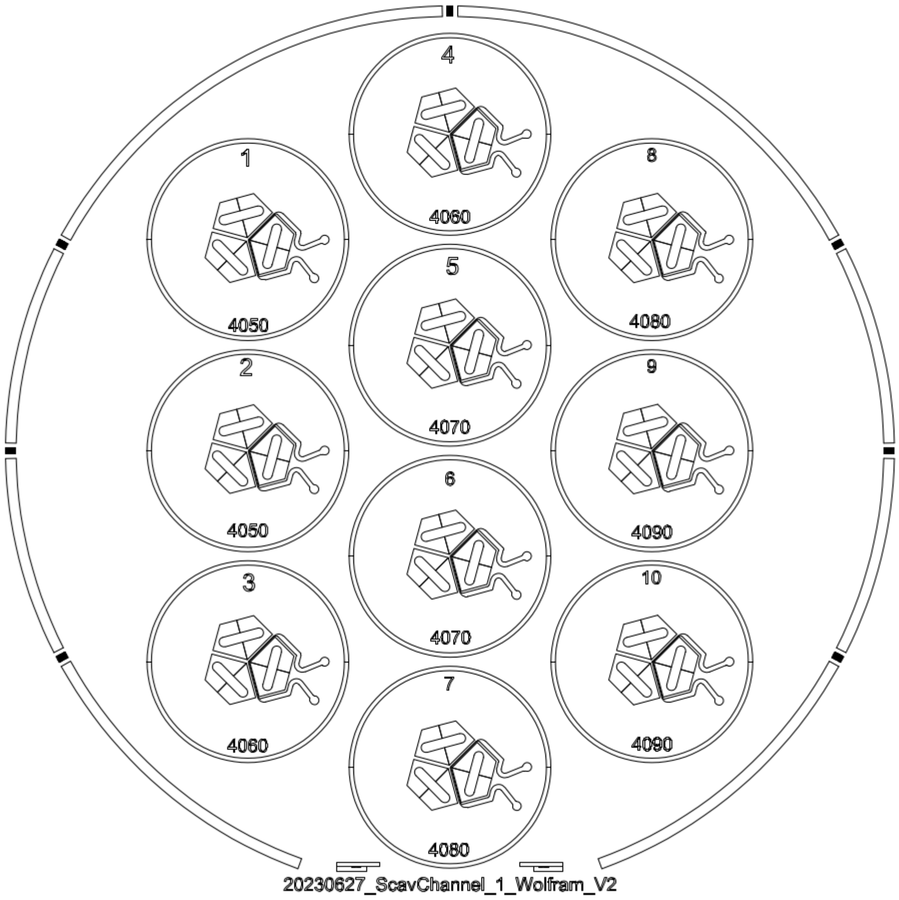
4
4060
1
4050
8
4080
5
4070
2
4050
9
4090
6
4070
3
4060
10
4090
7
4080
20230627_ScavChannel_1_Wolfram_V2

APPENDIX C: MATLAB CODE TO FIND TIME CONSTANTS

This MATLAB code was used to analyze oxygen concentration data over time in a specified location. It fits an exponential curve to the data and scans for the time point where the oxygen level falls below a preset threshold (37 %). This time point is identified as the system's time constant.

```
% Settings
initialOxygen = 19; %[%]
threshold = 0.37;
timeStep = 1; %[s]

% Prepare Data
t_time = ProbeData(:,1);
d_oxygen = ProbeData(:,2);
tau1 = 0;

% Fit data and find time constant
f = fit(t_time, d_oxygen,'exp2');
plot(f,t_time,d_oxygen)
for x = min(t_time):timeStep:max(t_time)
   if(f(x) <= initialOxygen * threshold)
       tau1 = x;
       break;
   end
end
output = ['Time Constant = ',num2str(tau1),'s'];
disp(output);
```